DISSERTATION

SIMULATED IMPACTS OF ANTHROPOGENIC LAND-COVER CHANGE ON THE MESOSCALE CLIMATE OF THE FLORIDA PENINSULA

Submitted by

Curtis Hal Marshall

Department of Atmospheric Science

In partial fulfillment of the requirements

For the Degree of Doctor of Philosophy

Colorado State University

Fort Collins, Colorado

Fall 2004

COLORADO STATE UNIVERSITY

May 28, 2004

WE HEREBY RECOMMEND THAT THE DISSERTATION PREPARED UNDER OUR SUPERVISION BY CURTIS H. MARSHALL ENTITLED SIMULATED IMPACTS OF ANTHROPOGENIC LAND-COVER CHANGE ON THE MESOSCALE CLIMATE OF THE FLORIDA PENINSULA BE ACCEPTED AS FULFILLING IN PART REQUIREMENTS FOR THE DEGREE OF DOCTOR OF PHILOSOPHY.

Committee on Graduate Work

William R. Cotton
Dr. William R. Cotton

A. Scott Denning
Dr. A. Scott Denning

Michael B. Coughenour
Dr. Michael B. Coughenour

Louis T. Steyaert
Dr. Louis T. Steyaert

Roger A. Pielke Sr.
Dr. Roger A. Pielke, Sr., **Adviser**

Jeffrey L. Collett, Jr.
Dr. Jeffrey L. Collett, Jr., **Acting Department Head**

ABSTRACT OF DISSERTATION

SIMULATED IMPACTS OF ANTHROPOGENIC LAND-COVER CHANGE ON THE MESOSCALE CLIMATE OF THE FLORIDA PENINSULA

Datasets representing both natural and current land cover on the Florida peninsula were implemented in the Regional Atmospheric Modeling System to simulate the impacts of anthropogenic land-cover change on the mesoscale climate of the region. Implementation of current land cover in simulations of three recent July-August periods resulted in generally increased daily maximum temperature, especially along an interior north-to-south axis corresponding to natural wetlands within the Kissimmee River basin and south of Lake Okeechobee that were drained during the 20th Century. In the natural land-cover case, this axis was associated with a local minimum in sensible heat flux, which served to generate a horizontally divergent mesoscale wind that reinforced the convergence along the adjacent sea-breeze fronts. This feature was diminished or altogether absent in the simulations with current land cover, because those wetlands were largely drained during the 20th Century. As a result, the simulated convergence along the adjacent sea-breeze fronts was weakened, and the divergence along the interior axis was diminished. This mechanism resulted in decreased rainfall along the sea-breeze fronts and increases along the interior axis. When expressed as an average over the model domain, the convective rainfall was decreased 10-12% from the natural case total. These

results provide evidence of a physical-dynamical mechanism that links the mesoscale spatial distributions of the changes in land cover, surface fluxes, the sea-breeze circulations, and convective rainfall with a regional-scale decrease in warm season rainfall. These results were consistent when subjected to a variety of model sensitivity tests. The differences in grid-average rainfall and daily maximum temperature are also consistent with long-term trends derived from an analysis of observational data.

The two land-cover datasets were also applied to simulate three recent (and climatologically rare) damaging freeze events in south Florida. In most areas of the model domain where wetlands were drained and converted to agriculture during the 20th Century, minimum temperatures were colder when current land cover was implemented. Further examination of one event reveals that if wetlands were specified, the resulting increased heat capacity of the surface and a persistent water vapor flux acted to diminish the cooling rate of the lower atmosphere, thereby altogether preventing the development of freezing conditions at a location where crop losses totaled US $300M. With current land cover (agriculture), subfreezing temperatures developed and persisted for five hours.

The results presented in this work suggest that anthropogenic land-cover changes have significantly impacted several aspects of the mesoscale climate of the Florida Peninsula. The results of this study also support previous studies in concluding that perturbations introduced to the climate system through anthropogenic land-cover change are physically and socioeconomically significant.

Curtis Hal Marshall
Department of Atmospheric Science
Colorado State University
Fort Collins, CO 80523
Fall 2004

ACKNOWLEDGEMENTS

I thank Roger Pielke, Sr., my adviser, for providing solid scientific mentorship and guidance, and for encouraging me to chart an independent course. I also appreciate his willingness to accommodate the circumstances of life that can occasionally place a hurdle on the path to a Ph.D. I am grateful to the other members of my committee -- Bill Cotton, Scott Denning, Lou Steyaert, and Mike Coughenour -- for their scientific wisdom and support. I learned a lot from Bill Cotton and Scott Denning in the classroom and elsewhere. Lou Steyaert was integrally involved in all aspects of this study. I appreciate Mike Coughenour's willingness to serve as the external member of my committee.

The students and research staff of the Pielke research group provided crucial help throughout this research, and Dallas Staley always ensured that the machinery ran smoothly. And of course, I thank all of my friends and loved ones, far too numerous to list here, for their support and encouragement throughout my education.

Funding for this research was provided by USGS Grant 1434-CR-97-AG-00025, Task 7, and the USGS Geographic Research Applications Prospectus Activity. Additional support was provided by NASA Grant No. NAG5-11370.

TABLE OF CONTENTS

LIST OF FIGURES

Figure 4.26. Time series of the (a) net radiative flux difference (W m^{-2}) in the first model layer (defined as Rn at the land surface minus Rn at model level 1, near 20 above ground level) and (b) the cooling rate (deg h^{-1}) due solely to the flux divergence in the same layer. Symbol convention same in Figure 4.23.

Figure 4.27. Same as in Figure 4.26, except the quantities pertain to sensible heat flux in the first model layer.

Chapter 1

INTRODUCTION

1.1 Anthropogenic Land-Cover Change on the Florida Peninsula

Mankind has dramatically transformed the land cover on the Florida peninsula. This transformation began during the 16th Century, when Juan Ponce de León arrived on the Atlantic coast near present-day St. Augustine. During the decades that followed, European colonists and slave laborers cleared pine forests and wetlands to build forts and villages, and to make way for crops. However, the great majority of the land-cover change within south and central Florida occurred during the 20th Century, when urbanization over coastal areas and agricultural production over the interior accelerated in earnest. During the Great Depression, President Roosevelt's New Deal brought large-scale public works projects to the region. Coastal resort towns grew into major population centers. Interior land was "reclaimed" to promote the growth of the state's agricultural industries, especially citrus and fresh vegetable farming. Natural hydrologic systems, including rivers, lakes, and wetlands, were harnessed to provide fresh water for irrigation and domestic use, and to prevent the frequent flooding that plagued the region.

Prior to human intervention, much of the rain that fell on the peninsula drained inward, towards the wide, perpetually inundated flood plain of the Kissimmee River, which in turn drained southward into Lake Okeechobee (Figure 1.1 illustrates the

locations of key geographical features on the Florida peninsula). Natural flow over the south rim of the lake spilled into the wide expanse of the Everglades. The vast area of standing water within the Everglades seeped slowly south and west into Florida Bay. However, overland flow comprised a relatively small percentage of the terrestrial hydrologic budget of the peninsula, because much of the rainfall was expended through evaporation and transpiration before reaching Florida Bay (Kushlan 1990). After the major water diversion projects of the early and middle 20th Century, much of the Kissimmee River flood plain had been drained, and the south shore of Lake Okeechobee had been dammed. Today, overland flow within the Everglades is highly managed through an intricate network of levees and canals. The landscapes of south and central Florida and the Everglades have been changed forever, as eloquently described by Marjory Stoneman Douglas in *The Everglades: River of Grass* (1947):

> "There are no other Everglades in the world. They have always been one of the unique regions of the earth, remote, never wholly known. Nothing anywhere else is like them: their vast glittering openness, wider than the enormous visible round of the horizon, the racing free saltness and sweetness of their massive winds, under the dazzling blue heights of space. They are unique in simplicity, the diversity, the related harmony of the forms of life they enclose.
>
> "The miracle of the light pours over the green and brown expanse of sawgrass and of water – shining and slow moving below, the grass and water that is the meaning and central fact of the Everglades of Florida.
>
> "It is a river of grass.
>
> "Where do you begin? Because when you think of it, history, the recorded time of the earth and man, is in itself something like a river. To try to present it whole is to find oneself lost in the sense of continuing change. The source can be only the beginning in time and space and the end is the future and the unknown.

"So it is with the Everglades, which have the quality of long existence in their own nature.

"They were changeless. They were changed."

A comparison of pre-1900 and 1993 land-cover maps (Figure 1.2) clearly demonstrates how human activities have changed the landscape over the entire peninsula during the 20th Century. Within the Everglades, the extent of freshwater marshes has been reduced by agricultural development, and significant areas of slough and bog have been displaced by sawgrass marsh. The freshwater marshes and other types of wetlands within the Kissimmee River basin and the watershed of the St. John's River have been drained and converted to agriculture and pasture. Across the remainder of the peninsula, agriculture and urban complexes have replaced large areas of natural pine forestland.

The purpose of this work is to present a study that was designed to evaluate the impacts of the land-cover changes described above on the mesoscale climate of the Florida peninsula. A mesoscale meteorological model was configured with two separate land-cover datasets that represent the land-cover change on the peninsula during the 20th Century. The results from simulations with these two model configurations were evaluated to assess the impacts of land-cover change on several aspects of warm season weather, including the diurnal cycle of shelter-level temperatures, near-surface wind features (especially the sea breezes), and the distribution of convective rainfall. The evaluation of impacts on cool season weather is focused on simulations of recent agriculturally damaging freeze events in south Florida. From both a meteorological and socioeconomic perspective, occasional damaging freezes are among the most significant aspects of cool season weather in south Florida.

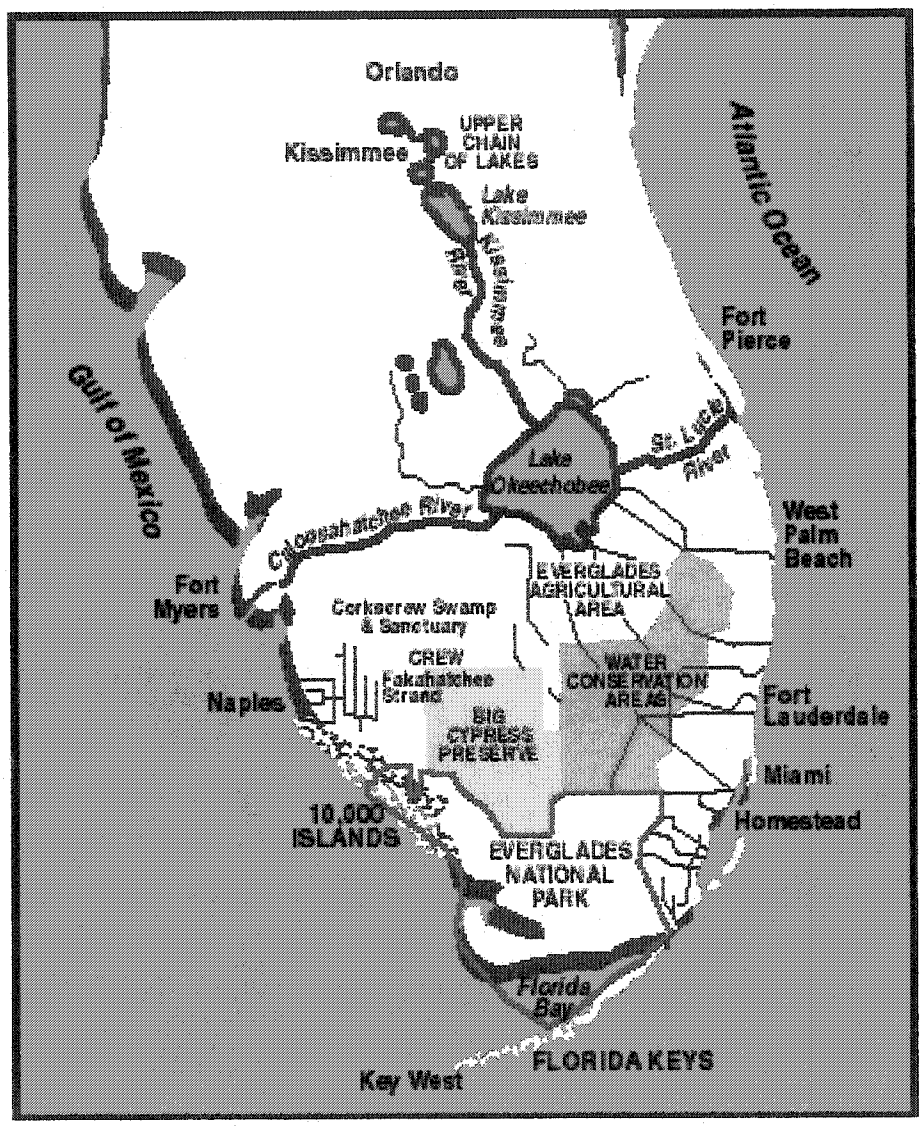

Figure 1.1. Map of the Florida peninsula illustrating the locations of important geographical features.

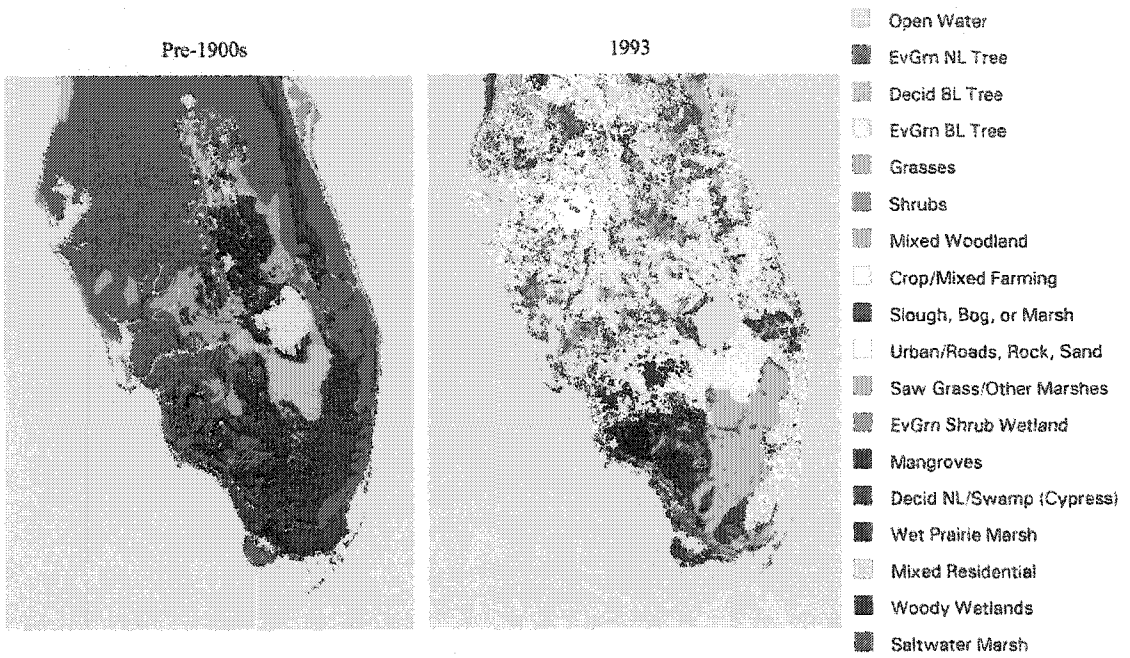

Figure 1.2. Maps that represent the pre-1900 (left) and 1993 (right) land cover on the Florida peninsula (see Chapter 2 for a description of these data).

1.2 Warm Season Impacts

Many studies have addressed the impacts of land-cover change on warm season weather features over spatial scales similar to the size of the Florida peninsula. Several of these studies have emphasized the relationships among land-cover heterogeneities, surface-forced circulations, and the spatial distribution of cumulus convective rainfall (e.g., Anthes 1984; Wetzel 1990; Segal and Arritt 1992; Dalu and Pielke 1993; Pielke et al. 1999; Pielke 2001; Weaver and Avissar 2001). Over the Florida peninsula, the dominant mode of convection during the warm season is associated with the sea-breeze fronts (Byers and Rodebush 1948; Pielke 1974; Blanchard and Lopez 1985; Michaels et al. 1987; Simpson 1994). Anthropogenic alterations in the nature of the land cover of the

peninsula could have impacts on the physical characteristics of these circulations, because they are driven primarily by contrasting thermal properties between the land and adjacent ocean (Pielke and Cotton 1977; Gannon and Warner 1990; Baker et al. 2001). This mechanism could have important implications for the distribution of sea-breeze convective rainfall. Furthermore, changes in land cover over the peninsula could impact other (inland) mesoscale circulation features (and related convective rainfall), and the diurnal cycle of surface thermodynamics (e.g., shelter-level temperature).

Pielke et al. (1999) provided a brief study that addressed the possible impacts of 20th Century land-cover change on the peninsula's summertime near-surface temperature and convective rainfall. They presented three numerical simulations of the period July-August 1973. The model configuration differed among the simulations only by the specification of land cover. Land-cover databases that were constructed to represent 1900, 1973, and 1993 conditions were implemented separately in the three simulations. An increase in the average July-August near-surface temperature occurred when the 1900 land cover was replaced with the 1973 or 1993 dataset. The simulations that used later land cover also yielded a decrease in grid-average, two-month total rainfall. Time series of observational data from selected stations were provided that indicated increased temperature and decreased rainfall during the 20th Century. It was suggested that the observed changes could be explained partially by the model results. However, the conclusions were limited because of the limited scope of the model simulations. The different land-cover datasets were applied to simulations of only one July-August period, and the impacts of land-cover change were not examined within the framework of sensitivity factors that strongly influence the numerical simulation of warm season

convective rainfall and near-surface sensible weather. Moreover, relationships among anthropogenic land-cover change, surface energy fluxes, surface-forced circulations, and convective rainfall were not linked within the context of a mesoscale, physical-dynamical framework.

In this current work, the preliminary study is revisited and significantly expanded upon. New land-cover datasets that are highly detailed and considerably more realistic than those utilized in the previous study were constructed for this work. Additional warm season periods were simulated, and the results were evaluated within the context of important model factors that could strongly impact the outcome. It will be shown that, despite subjection to a multitude of factors that could eclipse the role of land cover, the replacement of pre-1900 land cover with present-day data affects the simulated warm season rainfall and near-surface sensible weather in a consistent and robust manner. Moreover, a physical-dynamical mechanism is identified that directly links anthropogenic land-cover change and changes in the distribution of cumulus convective rainfall with changes in the characteristics of the sea-breeze circulations. The model results are corroborated by comparison with a significantly expanded observational dataset.

1.3 Cool Season Impacts: Agriculturally Damaging Freezes

Agriculture has always been the mainstay of Florida's economy. Florida-based production of citrus, winter fresh vegetables, and sugarcane comprise a large share of the United States market for these products. During 2002, Florida ranked first in the nation for cash receipts of citrus crops, and either first or second for several fresh fruit and vegetable crops, including tomatoes, strawberries, snap beans, squash, sweet corn, bell

peppers, watermelons, radishes, and avocados (FDACS 2002). By some estimates, more than half of the fresh vegetables consumed by Americans during the core winter months are harvested in south Florida (Hansen et al. 1999).

Although more prone to damaging freezes, northern and central areas of the peninsula have been preferred in the past because the well-drained, sandy soils provide a less disease prone environment than the wetlands and saturated organic soils of south Florida. Moderate freezes that can destroy tender vegetable crops and may damage or kill citrus foliage and blossoms occur with some regularity in northern and central areas of the peninsula. These freezes are not typically severe enough to kill or result in permanent wood damage to citrus trees (Weischet and Caviedes 1987). Occasionally, however, winter freezes have wrought severe destruction on agriculture in northern and central Florida. Around the turn of the 20th Century, a series of killing freezes prompted a dramatic southward shift in production toward central areas of the peninsula. Prior to that time, orange groves were planted as far north as Jacksonville and Tallahassee.

Citrus production flourished after the southward shift in production to central Florida, but occasional catastrophic losses have been unavoidable, despite improvements in frost and freeze protection technologies. During the 1980s, a series of severe freezes destroyed many groves of the central peninsula. Attaway (1997) documents the killing freezes that have resulted in southward migration of the citrus industry during the past 150 years. He suggests that after the "catastrophic period from 1981-1989," perceptions changed permanently amongst Florida's citrus community regarding the risk of freeze in central areas of the state. Many producers elected to avoid the risk of more damaging freezes by relocating, thereby beginning a second dramatic southward shift of the primary

areas of citrus production on the peninsula (Whittaker 1985; Miller 1991). Prior to and during this timeframe, significant areas of wetlands in south Florida were drained to provide agricultural land, particularly for winter vegetable and sugarcane production. In many cases, citrus producers relocated to these drained wetlands areas. Figure 1.3 illustrates the number of citrus trees by county, as well as the key areas of vegetable production in Florida during 2000. Comparison with Figure 1.2 shows that many of these areas are within or near locations that were once natural wetlands.

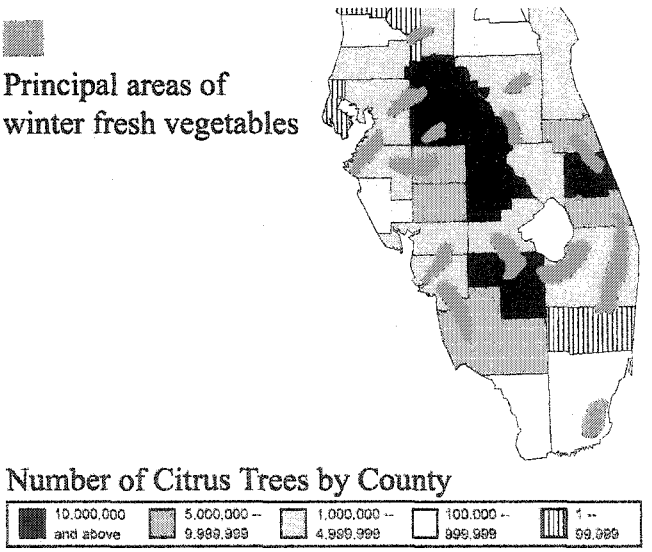

Figure 1.3. The number of citrus trees by county, and key areas of winter vegetable cultivation during 2000 (figure adapted from the Florida Agriculture Facts Directory; FDACS 2002).

Previous investigators have documented the correlation of freezes with the phases of the Pacific North American pattern (PNA; Horel and Wallace 1981), the El Niño Southern Oscillation (ENSO; Ropelewski and Halpert 1986) and the North Atlantic Oscillation (NAO; Rogers 1984). These studies show that freezes are more likely in south Florida when the PNA (NAO) is in a positive (negative) phase (Downton and Miller 1993). A recent analysis by the Florida Climate Center indicates that killing freezes are more likely during winters in which the phase of ENSO is neutral (http://www.coaps.fsu.edu/~grant/flclimate/spotlight). Another interesting and as yet relatively unexplored question involves whether *it is possible that the conversion of natural wetlands to accommodate the expanding agricultural production in south Florida could itself have an impact on the incidence or severity of freeze events in that region.* In this work, model simulations of three recent freeze events are evaluated to address this question. It will be shown that the specification of land cover was critical to both the development and severity of killing freezes at key agricultural production centers in south Florida.

Chapter 2

BACKGROUND AND METHODOLOGY

2.1 The Regional Atmospheric Modeling System: Design and Configuration.

Version 4.3 of the Regional Atmospheric Modeling System (RAMS; Pielke et al. 1992; Cotton et al. 2003) was used for the numerical simulations presented in this work. All simulations were performed on the horizontal grid domain shown in Figure 2.1. The outer grid, which consists of 42 X 48 points spaced at a 40 km interval, covers the southeastern corner of the United States and extends southward to the latitude of the Yucután Peninsula. An inner grid of 42 X 50 points spaced at 10 km was nested to cover central and south Florida and adjacent coastal waters. The vertical domain of both the inner and outer grids extends over thirty vertical levels. For the warm season simulations, the lowest level was set to near 100 m above ground level. For the simulations of the freeze events, the lowest level was located near 20 m above ground level. In both cases, the vertical grid spacing was geometrically increased with height to a maximum of 1 km at the model top (near 20 km).

A 1 min. time step was employed on the outer grid, with 30 s on the inner grid. Forward-backward first-order time differencing was used with a split-explicit scheme for filtering fast modes (Tremback et al. 1987). Initial conditions were provided by the National Centers for Environmental Prediction (NCEP)/National Center for Atmospheric

Research (NCAR) Global Reanalysis dataset (Kalnay et al. 1996). The Reanalysis data, available at 6-hour intervals, were interpolated in time and spatially nudged over the five outer-most RAMS domain grid points to provide lateral boundary conditions at each time step during the model integration (Davies 1976). Over ocean areas of the model domain, the sea-surface temperature (SST) was specified using the one-degree, monthly climatological dataset available from NCEP (Reynolds and Smith 1994).

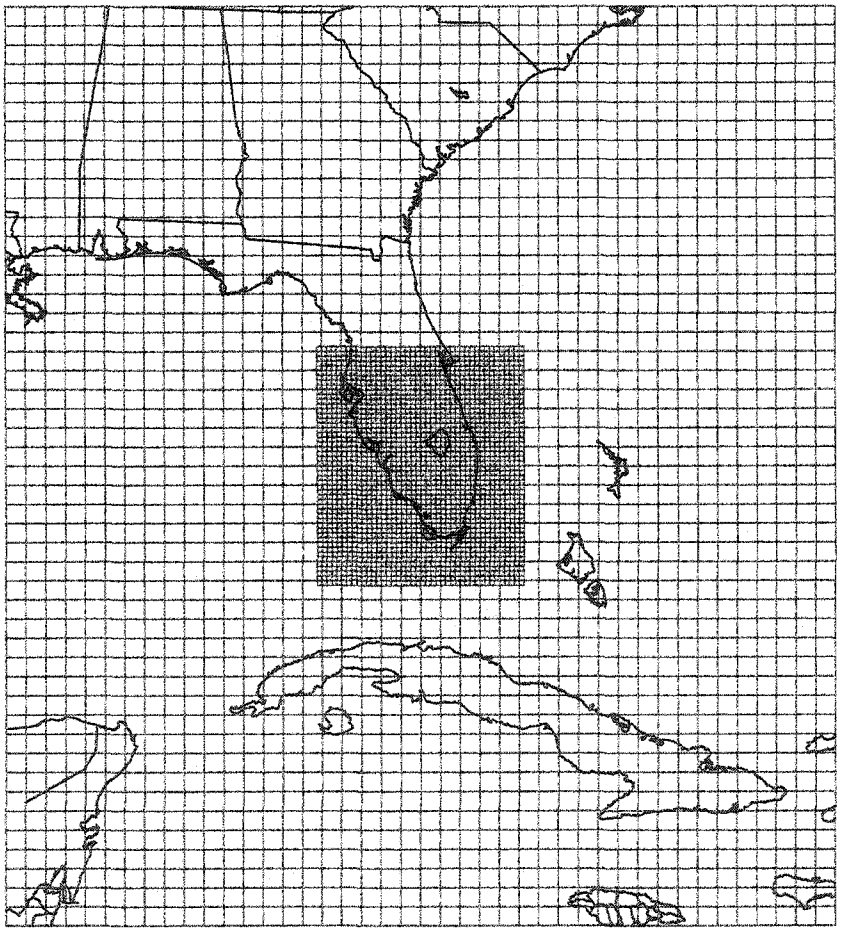

Figure 2.1. RAMS horizontal grid configuration used for all numerical simulations.

Precipitating deep convection was parameterized with the Kain-Fritsch scheme (Kain and Fritsch 1993), with adjustments to the adjustments to the terrain-dependent convective trigger function as described by Castro et al (2002). In the warm season simulations, the vertical flux of short-and longwave radiation was parameterized with the radiative transfer scheme of Mahrer-Pielke (Mahrer and Pielke 1977). The Chen-Cotton Scheme (Chen and Cotton 1983) was used for the freeze simulations. The subgrid-scale turbulent fluxes were represented with prognostic turbulent kinetic energy (Mellor and Yamada 1974). The surface exchange coefficients in all simulations were defined following Louis (1979).

The surface energy budget in RAMS was parameterized with the Leaf-Ecosysetem-Atmosphere-Feedback-2 (LEAF-2; Walko et al 2000) land-surface model, which partitions the net radiation at the land-surface into sensible, latent (evaporation plus transpiration), and soil heat fluxes. The fluxes in LEAF-2 are parameterized with a resistance approach, similar to Ohm's Law for electrical current. The various physical controls on the flux are represented as resistors in series. For example, the effects of stomatal control, soil water availability, and aerodynamic resistance are represented mathematically as resistances in series that constrain the transpiration rate. The resistances themselves are empirical functions that incorporate numerous factors, including soil and land-cover class-dependent parameters.

The soil model that accompanies LEAF-2 was configured to consist of eleven vertical layers spanning a depth of 2 m. This model contains prognostic equations for both soil moisture and soil temperature to account for the vertical flux of heat and water within the soil column. The soil moisture is of first-order importance in determining the

evaporation and transpiration. The vertical profile of soil temperature evolves in response to the soil heat flux to partly determine the surface radiative ("skin") temperature, which provides the basis for the lower boundary condition for diagnosing the surface sensible heat flux and the longwave radiation emitted by the land-surface.

In all the simulations, the soil temperature in the top layer was initialized at a value equal to the initial condition for air temperature at the first atmospheric level above ground. This temperature was adjusted linearly with depth to a bottom layer value that was constrained to the climatological annual mean value of shelter-level temperature at the grid point location in question. For the warm season simulations, the top layer soil moisture was initialized as 40% of the saturation value. This value was increased linearly to a maximum value of 60% saturation at depths below 50 cm. The soil moisture initialization was applied in a horizontally homogenous fashion, in keeping with the method employed by Pielke et al. (1999) in the preliminary study. For the simulations of the freeze events, the dataset provided by the University of Washington Variable Infiltration Capacity (VIC) model archive (see Maurer et al. 2002 for a description of both the VIC model and the production of this archive dataset) was used to initialize soil moisture. The saturation value (i.e., soil porosity) and all other soil hydraulic and thermodynamic properties were based on the global 3 km soil type database that has been compiled by the Food and Agriculture Organization of the United Nations (FAO 1997). These properties were also used to convert the data provided from the VIC archive from total column water to volumetric water content, which is the prognostic variable in LEAF-2. For this work, one important modification was made to the FAO soils database.

Organic soil was specified for wetlands areas of the peninsula, along with the associated soil hydraulic parameter values for that soil type

Forty separate land-cover classes were implemented in LEAF-2 for this work. These classes were provided by 1 km datasets that were designed to represent the pre-1900 and 1993 conditions illustrated by Fig. 1.2. The subgrid "tile" method was used to assign four classes to each RAMS model grid cell. In short, the percentage of the area occupied by each class within a RAMS grid cell was determined. The four predominant classes were assigned a tile. A fifth tile was always reserved for the presence of permanent, open water (i.e., lakes), within the grid cell. (Note: permanent, open water is classified differently from wetlands, which are described in more detail in the next section.) During the integration of the model, the surface fluxes were calculated separately for each tile. The flux provided to the atmospheric boundary layer was a weighted average of the individual tile values within the RAMS grid cell. The weights were based on the percentage of area covered by the tile class within the RAMS grid cell. With the use of the tile approach, the fluxes of energy and water are influenced by the subgrid-scale heterogeneity of land-cover. The land-cover datasets used to provide the tile classes are now described in more detail.

2.2 Land-Cover Datasets

The U.S. Geological Survey (USGS) developed the datasets that were used to produce the maps of pre-1900 and 1993 land cover that are provided in Figure 1.2. The datasets cover the southeastern United States at 1 km grid spacing. As mentioned above, the datasets were used to assign four separate tile classes for each RAMS model grid cell.

To accommodate the use of these datasets in RAMS, the number of LEAF-2 vegetation classes was expanded to include sloughs, bogs, sawgrass marshes, wet prairie marshes, saltwater marshes, deciduous needleleaf swampland (i.e., cypress swampland), evergreen broadleaf swampland (predominantly mangroves), various mixed woody wetland complexes consisting of mixed trees and shrubs, and modified residential and urban classes. Addition of these classes to the standard LEAF-2 classes provided a total of 40 classes for this work.

In LEAF-2, each land-cover class is associated with values for several physical parameters. These parameters include Leaf Area Index (LAI), fractional vegetation coverage (σ_f), shortwave albedo (α), longwave emissivity (ε), roughness length (z_o), and rooting depth. The USGS determined parameter values for these classes by tailoring standard LEAF-2 parameter values for wetlands with knowledge gained from field observations of research scientists in the Everglades and key sources in the literature (Steyaert 2004, personal communication). In general, the tailored values are LEAF-2 parameters that have been modified to account for the effects of water inundation. For example, the albedo value for sawgrass marsh is based on the LEAF-2 value for tall grass, with a slight reduction to account for surface water. In some cases, the mixed-wetlands parameters were based on weighted averages of LEAF-2 parameters. For example, the parameter values for tropical hardwood were defined as the average of the LEAF-2 parameter values for deciduous broadleaf trees and evergreen broadleaf trees. It is emphasized that all parameter values were determined *a priori*. No tuning of parameter values was undertaken *ex post facto* to the numerical simulations in order to influence the results presented in this work.

The explicit representation of wetlands is among the most important aspects of the model configuration used for this study. To explicitly represent surface water in wetlands, vegetation classes identified as a swamp or marsh type, which cover much of the Everglades and the Kissimmee River valley, were inundated with 10 cm of standing water, if the wetlands class was determined to be within the hydroperiod during the time of year covered by the simulation. The hydroperiod is defined as that time of year during which the surface is inundated with standing water. On the Florida peninsula, some wetlands locations become devoid of standing water during the "dry season," which coincides roughly with continental winter. Other wetlands complexes remain inundated all year. For this work, The USGS determined the hydroperiods (Steyaert 2004, personal communication). Hydroperiods for freshwater marshes were based primarily on the work of Kushlan (1990). Hydroperiods for other wetlands were based on information provided to USGS by researchers at the University of Florida. The 10 cm depth was chosen to facilitate an effective value for a RAMS grid cell, recognizing the substantial degree of subgrid-scale variability in the actual depth of water in wetlands over such an area. For all wetlands classes, soil moisture was initialized at complete saturation at all levels, regardless of whether the class was within its hydroperiod during the time covered by the simulations. This is consistent with observations that even during the dry season, the organic soils in wetlands areas remain saturated. The initial temperature of the surface water was set equal to the initial air temperature at the first model layer, and allowed to evolve in accordance with the modeled surface energy budget.

The USGS utilized a Geographic Information System (GIS) to combine a variety of data sources to define a consistent set of land-cover classes for LEAF-2 (Steyaert

2004, personal communication). These classes are the basis of Figure 1.2. Early vegetation maps, historical analyses, paleo-studies, and literature sources were the primary inputs for the pre-1900 land cover. The reconstructed pre-1900 vegetation for the Everglades (south of the Kissimmee River watershed) was based on a GIS analysis of the Davis (1943) South Florida Natural Vegetation Map, with modifications to the sawgrass plains areas just south of Lake Okeechobee provided by McVoy (1996), McVoy et al. (2002), and Willard et al. (2001). McVoy (1996) analyzed historical documents and early photographs to reconstruct the distribution of sawgrass and slough/bogs/marshes in the Everglades prior to conversion to agriculture and the diversion of surface water flow by the construction of surface hydrology controls [an historical review of water resource engineering activities is provided by Light and Dineen (1994)]. Willard et al. (2001) confirmed the reconstruction provided by McVoy (1996) by analysis of pollen extracted from sedimentary core samples taken within the Everglades. These input datasets were combined within the framework of a careful and comprehensive analysis. Thus, it is believed that the pre-1900 dataset used for this work closely represents the land-cover conditions that existed within the Everglades prior to any significant anthropogenic modifications.

The Küchler (1964) potential natural vegetation dataset was used as the primary input data source for the pre-1900 land cover for most of the Florida peninsula outside the Everglades region, and for the rest of the RAMS model domain (the outer model grid shown in Figure 2.1). However, the southern mixed forest class was modified to a predominantly evergreen needle leaf forest, which represents the extensive areas of Longleaf Pine and Florida Slash Pine in fire-prone areas (Landers and Boyle 1999).

Also, the data were modified to account for the freshwater marsh areas of the southern St. Johns River basin (note the axis of marsh over the east central peninsula shown in Figure 1.2, just inland of Cape Kennedy, southward to the latitude of the north shore of Lake Okeechobee). For the Kissimmee River watershed, the pre-disturbance land cover constructed by Costanza (1975, 1979) was used as the primary input data source.

The 1993 land cover was derived primarily from the USGS 30 m National Land Cover Dataset (NLCD; Vogelmann et al. 1998, 2001) and the 30 m Florida Gap Analysis Project (GAP) land-cover dataset (Pearlstine et al. 2002). The NLCD, which covers the conterminous United States, is based on Landsat Thematic Mapper (TM) scenes obtained during the 1992-1993 timeframe. The GAP dataset was developed by the USGS (Biological Resources Discipline), the Florida State Cooperative Fish and Wildlife Research Unit, and the University of Florida, using Landsat Thematic Mapper (TM) scenes from the 1992-94 time frame. The RAMS land-cover on the outer grid domain was based solely on the NLCD data. The NLCD was combined with the GAP land-cover product to provide more detailed land-cover classes over the Florida peninsula. Urban, residential, mixed agriculture, and other classes representing intense land-use activities were selected from the NLCD, while wetlands, marshes, Longleaf Pine forests, and the other classes specific to the Florida peninsula were selected from the GAP data.

Chapter 3

WARM SEASON IMPACTS: SENSIBLE WEATHER AND THE SEA-BREEZE CIRCULATIONS

3.1 Background and Experimental Design

Pairs of simulations were completed for the July-August periods of 1973, 1989, and 1994. Within a given pair, the model configuration differed only because one member incorporated the pre-1900 (hereafter, "natural") data, whereas the other incorporated the 1993 (hereafter, "current") dataset. The July-August period was chosen for simulation in order to span a significant duration during the core of the rainy season in south Florida. The 1989 and 1994 periods were chosen for two reasons. First, both are relatively close to 1993. Presumably, land cover over the peninsula during these periods did not differ significantly from 1993 conditions. Second, the observed rainfall during those two summers ranged from drought (1989) to above normal (1994) (Schmidt et al. 2001). Thus, simulations of these two separate periods can be used to evaluate the impact of anthropogenic land-cover change within the context of a range of warm-season rainfall totals. The 1973 period was simulated to assess the impact of two significant changes that were implemented in the model configuration following the study by Pielke et al. (1999). The natural and current land-cover datasets implemented for this work are significantly more detailed and realistic than those used previously. In addition, the

Kain-Fritsch convective parameterization was implemented in lieu of the Kuo scheme (Kuo 1974).

Because of the public attention given to a perceived increase in the frequency and severity of drought in south Florida during the last century (e.g., Boyle and Mechem 1982), the 1989 simulations were chosen for additional analysis. Specifically, the diurnal cycle of shelter-level temperature and the near-surface mesoscale flow, particularly the sea breezes, were examined in detail. Furthermore, the 1989 results were subjected to a number of model sensitivity tests. This pair of simulations was repeated with alternative specifications for horizontal grid spacing, convective parameterization, radiative transfer, initial soil moisture, and regional SST. The sensitivity experiments and the requisite changes to the model configuration are described in detail in Section 3.6.

3.2 Rainfall

Figure 3.1 provides observed rainfall fields corresponding to the three simulation periods. For a variety of reasons, the value at any particular location within these fields should not be interpreted as ground truth. These fields are based on analyses of daily rainfall recorded by rain gauges at National Weather Service Cooperative Observation Network sites. The Climate Prediction Center (CPC) utilizes a Cressman scheme (Cressman 1959) to analyze the daily gauge totals on a 0.25°x0.25° grid domain covering the continental U.S. The fields shown here were constructed by summing the daily analysis values at locations within the RAMS domain over the two-month periods of interest. Thus, these fields reflect the analysis error and the sampling limitations of the point-specific gauge observations used to construct those analyses. The sampling error is

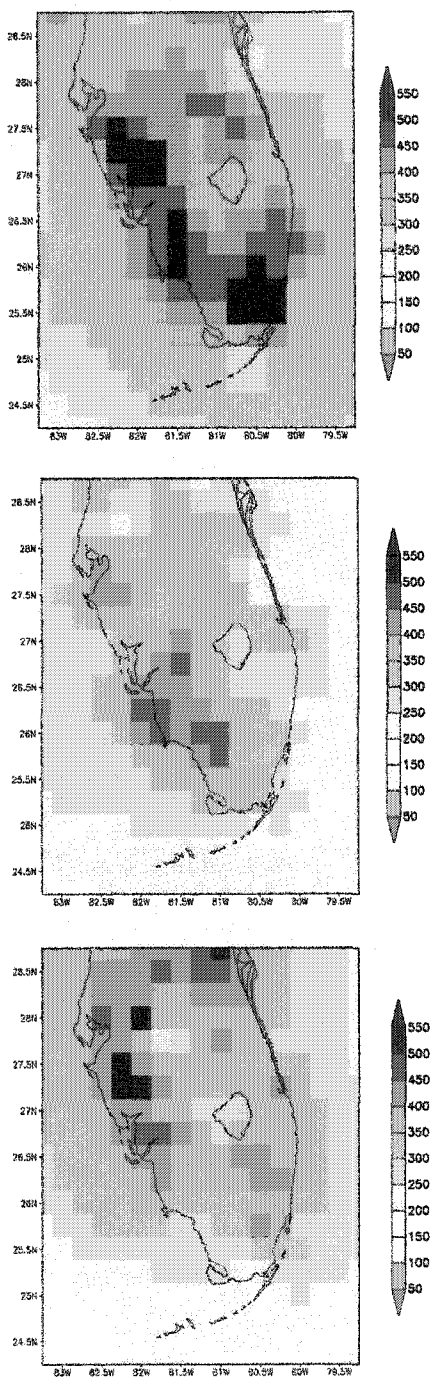

Figure 3.1. Accumulated precipitation (mm) from the CPC analysis of Cooperative Observation Network rain gauge data (analysis on a 0.25° grid) for (top) Jul-Aug 1973, (middle) Jul-Aug 1989, and (bottom) Jul-Aug 1994.

potentially significant because of the convective nature of warm season rainfall in Florida. Furthermore, the analyzed values over the ocean are extrapolated entirely from gauge data on the peninsula. Despite these limitations, the analyses are adequate for assessing the overall characteristics of the observed rainfall and for comparing with the model results. For example, the three analyses confirm that the 1973 and 1994 periods were generally wetter than the documented 1989 drought period. During the 1973 (top panel) and 1994 (bottom panel) periods, totals exceeded 400 mm over much of the peninsula, with a few locations exceeding 550 mm. Locations that received more than 400 mm during the 1989 period (middle panel) are confined to the immediate west coast. Elsewhere, the analyzed values are generally less than those for the other periods.

A comparison of the model results for 1973 (Figure 3.2) with those previously presented by Pielke et al. (1999) (not shown here) and the corresponding observed precipitation field reveals that the new model configuration provided significantly improved rainfall totals. The relative roles of the two major model configuration changes (land cover and convective parameterization) will be addressed further in Section 3.6. In the new simulations, rainfall exceeded 400 mm over a significant area. In the previous study, rainfall was significantly less than the observed at most locations. Local maximum rarely exceeded 300 mm. The smaller-scale spatial details from the new simulations do not exactly match the observed data. Also, the model field suggests that little rainfall fell over the oceans. Regardless, the simulated rainfall for this period agrees reasonably well with the observed field and it is significantly improved over the previous results. This general agreement holds true for the 1989 (Figure 3.3) and 1994 (Figure 3.4) periods. Furthermore, the simulated rainfall for the 1989 period is generally less

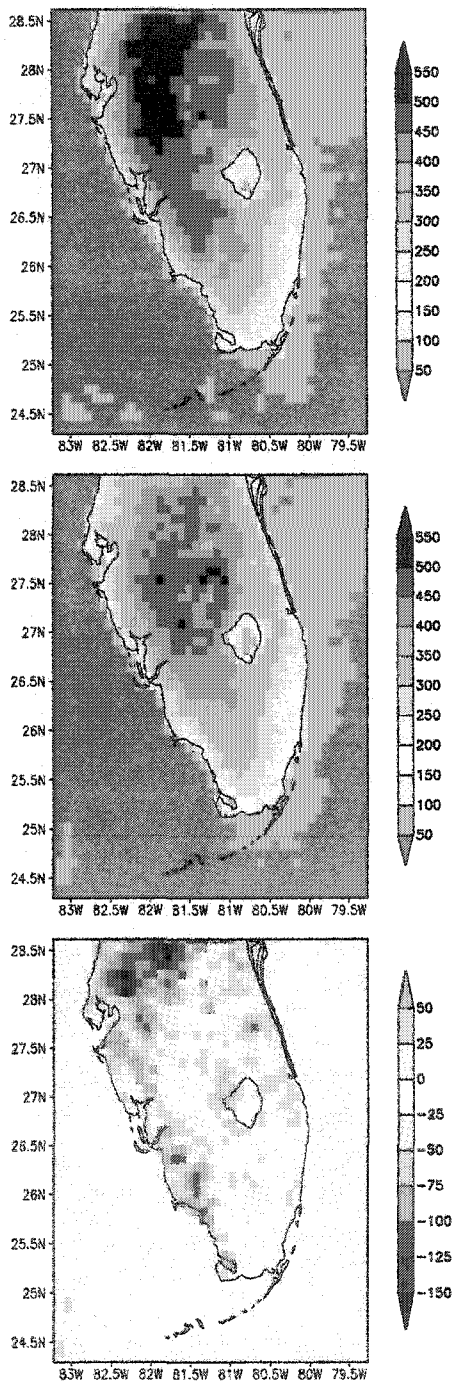

Figure 3.2. Accumulated convective rainfall (mm) from the model simulations of Jul-Aug 1973 with (top) natural land cover, (middle) current land cover, and (bottom) the difference field for the two (current minus natural case).

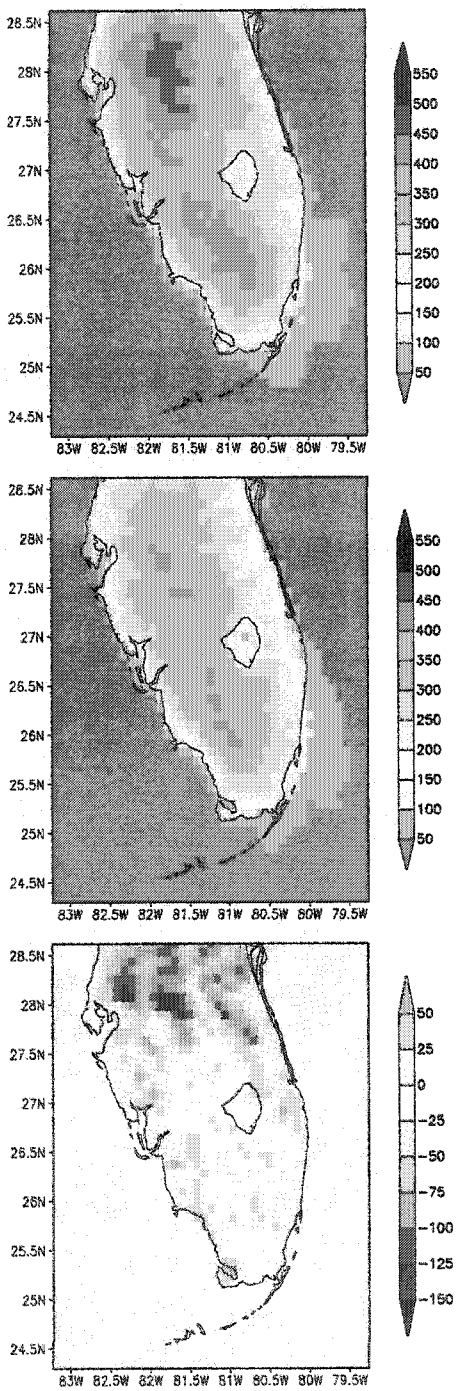

Figure 3.3. Same as in Figure 3.2, except for the simulations of Jul-Aug 1989.

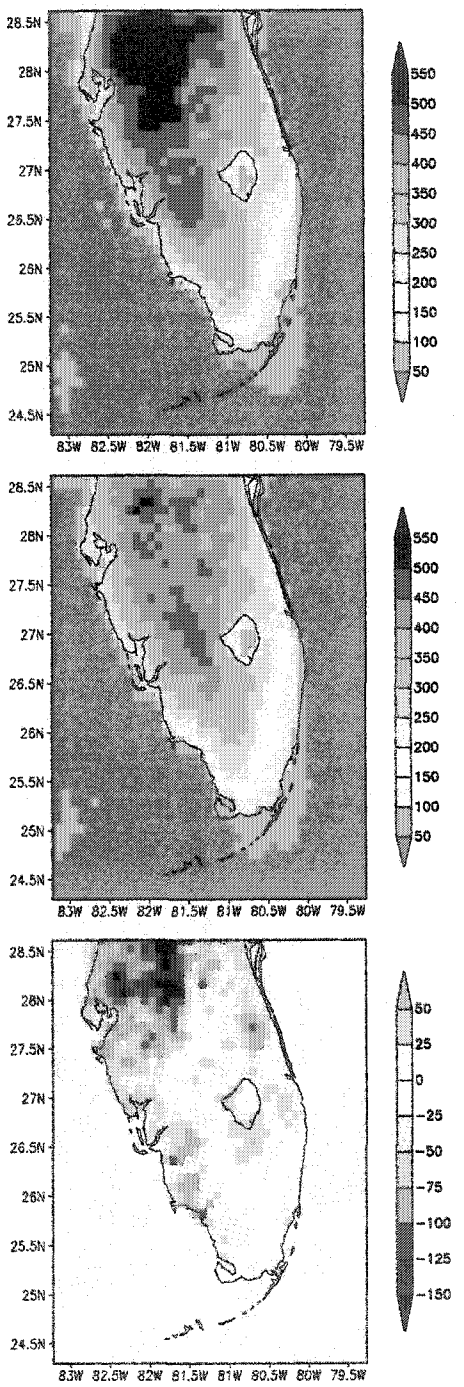

Figure 3.4. Same as in Figure 3.2, except for the simulations of Jul-Aug 1994.

than that for the 1973 and 1994 periods, in accordance with the variation among the observed rainfall fields.

In all three periods, rainfall was generally less in the current land-cover case. The rainfall difference fields (bottom panels of Figures 3.2-3.4; difference fields hereafter always defined as the current land-cover case minus the natural land-cover case) clearly illustrate decreased totals over much of the peninsula. Interestingly, the spatial average for each current land-cover case, as determined from data at land grid points only, is consistently 10%-12% less than the corresponding natural case grid average value. These differences are hydrologically significant. When expressed in terms of volume over the land area of the study domain, the rainfall difference fields are on the order of *millions* of acre-feet. The rainfall was decreased by an average of 2.6 M acre-feet during the July-August period when the current land cover was employed (Figure 3.5). This amount of water can be viewed in the proper perspective by considering that the average daily use of water in Miami-Dade county in south Florida is 1960 acre-feet (source: www.miamidade.gov).

Despite the consistent decrease in grid-average rainfall in each current land-cover case, rainfall was consistently larger along an interior axis that extends from the latitude of Tampa Bay to just south of Lake Okeechobee. This feature corresponds spatially to the axis of natural wetlands that once extended along Kissimmee River watershed, southward through Lake Okeechobee and into northern portions of the Everglades. Most of these wetlands were drained and converted to agriculture during the 20th Century (see Figure 1.2). Distinct north-to-south axes of decreased precipitation are juxtaposed between this central axis and both coasts. These axes of decrease extend along the

typical positions of the afternoon sea-breeze fronts (Michaels et al. 1987). The impacts of anthropogenic land-cover change on the physical characteristics of the sea-breeze circulations and the relationship to the distribution of convective rainfall are addressed in more detail in the following sections.

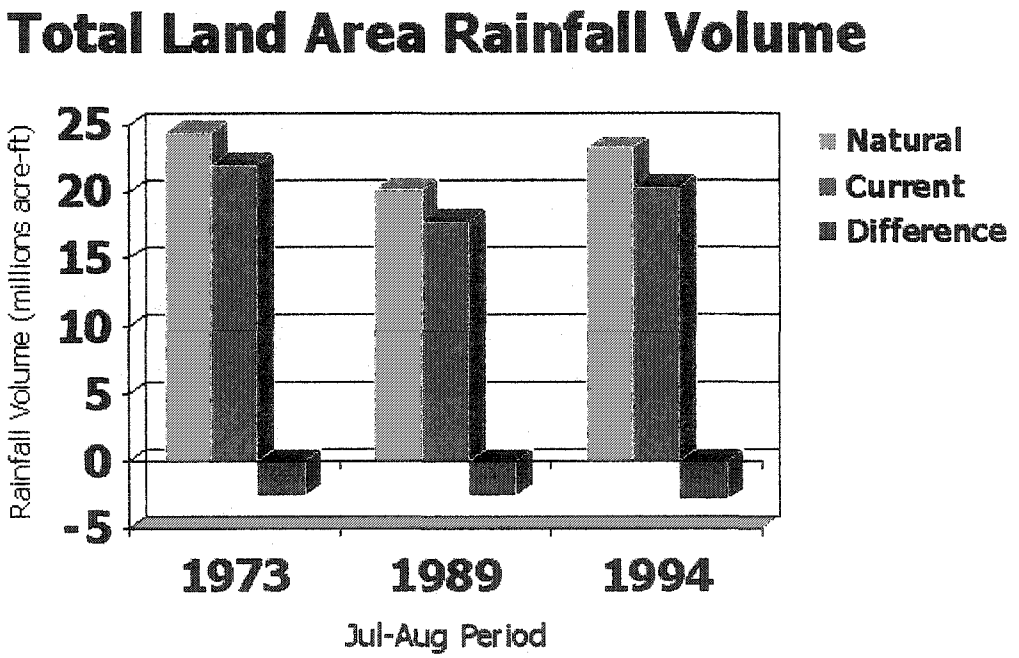

Figure 3.5. Rainfall expressed in traditional hydrologic volume units (acre-feet), for the rainfall fields shown in Figures 3.2-3.4. The totals are the sum of the volume of rainfall at all land grid points in the model domain.

3.3 Sensible and Latent Heat Fluxes

The patterns of average sensible and latent heat flux from the July-August 1973 simulations (Figures 3.6 and 3.7) are in general physical agreement with previous results provided by Pielke et al. (1999). Of particular interest is the distinct axis of increased sensible heat flux in the difference field (bottom panel of Figure 3.6) that extends along the Kissimmee River basin to south of Lake Okeechobee. This axis is co-located with the area drained wetlands and precipitation increases discussed above. Another distinct axis of increased sensible heat flux is located along the eastern coastal ridge. This increase is likely associated with urbanization. Figures 3.8-3.11 show the same general patterns in sensible and latent heat flux for the 1989 and 1994 periods. The grid average of the latent heat flux difference fields exhibits a consistent decrease of near 10% of the grid-average value for the natural land-cover case. The grid average sensible heat flux is nearly unchanged, despite the coherent patterns of increase over the central portion of the peninsula.

Attention is now turned towards more detailed investigation of the 1989 simulations.

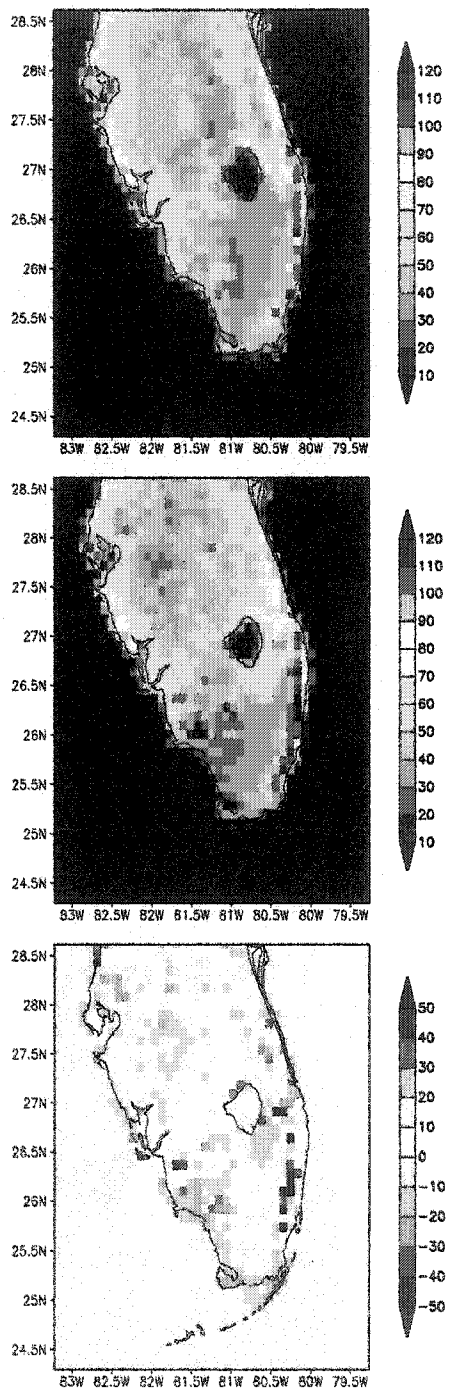

Figure 3.6. Two-month average of the surface sensible heat flux (W m^{-2}) from the model simulations of Jul-Aug 1973 for the (top) natural land cover, (middle) current land cover, and the difference for the two (current minus natural case).

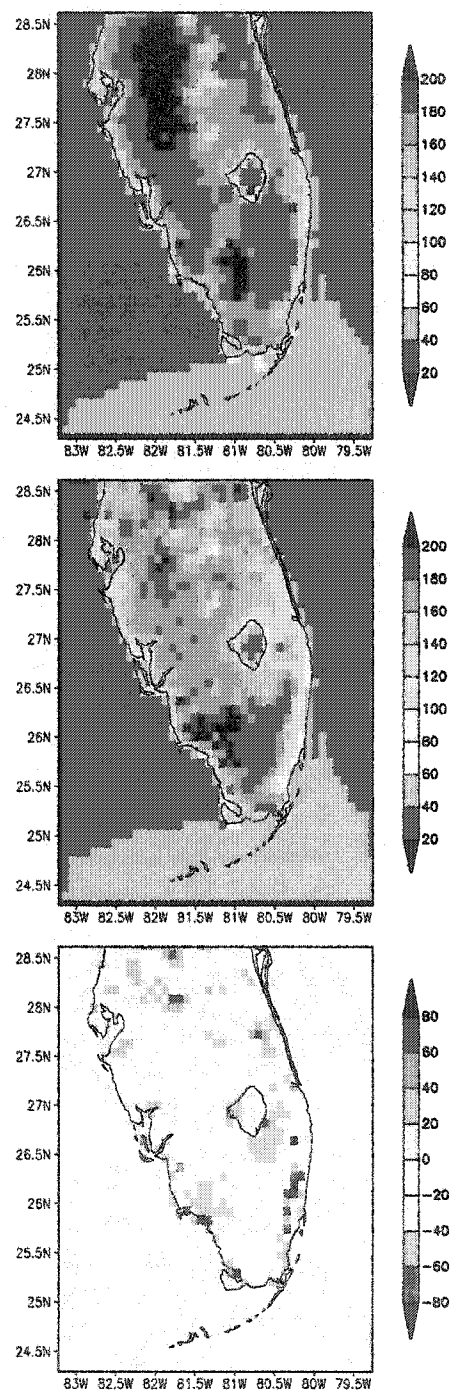

Figure 3.7. Same as in Figure 3.6, except for latent heat flux.

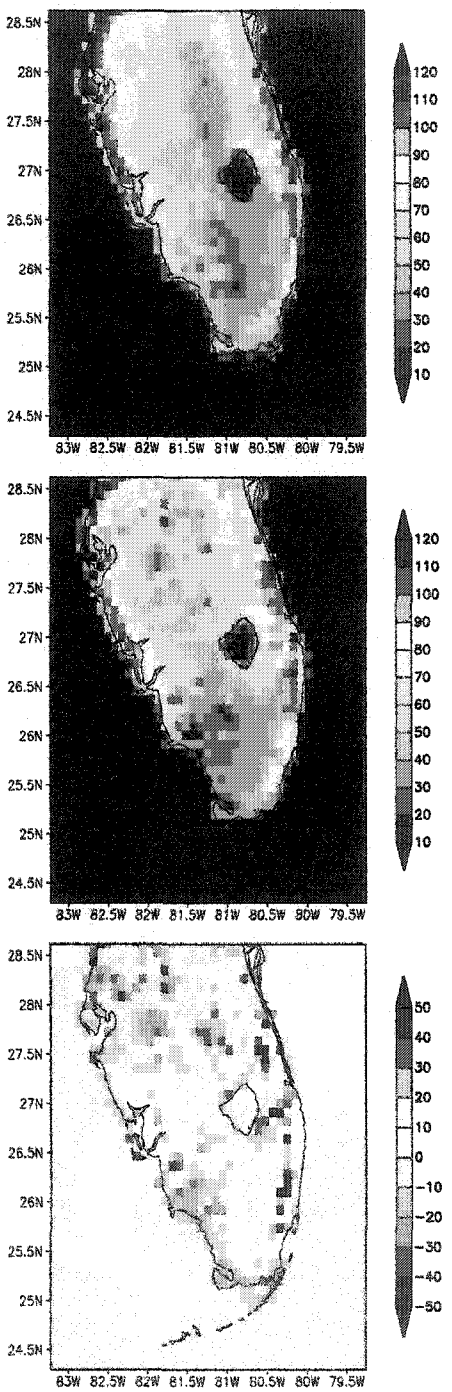

Figure 3.8. Same as in Figure 3.6, except for the simulations of Jul-Aug 1989.

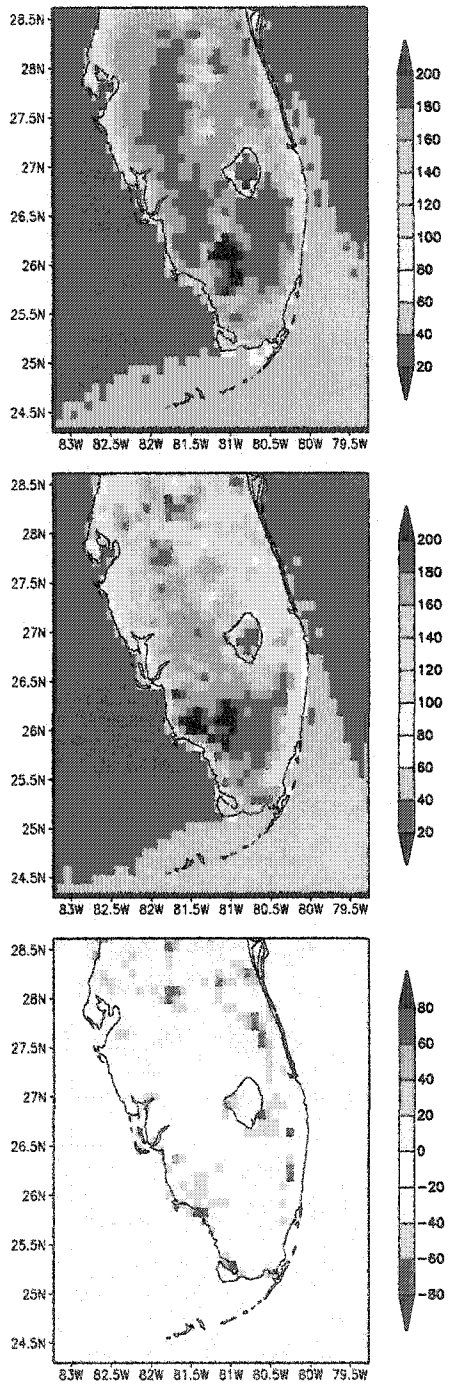

Figure 3.9. Same as in Figure 3.8, except for latent heat flux.

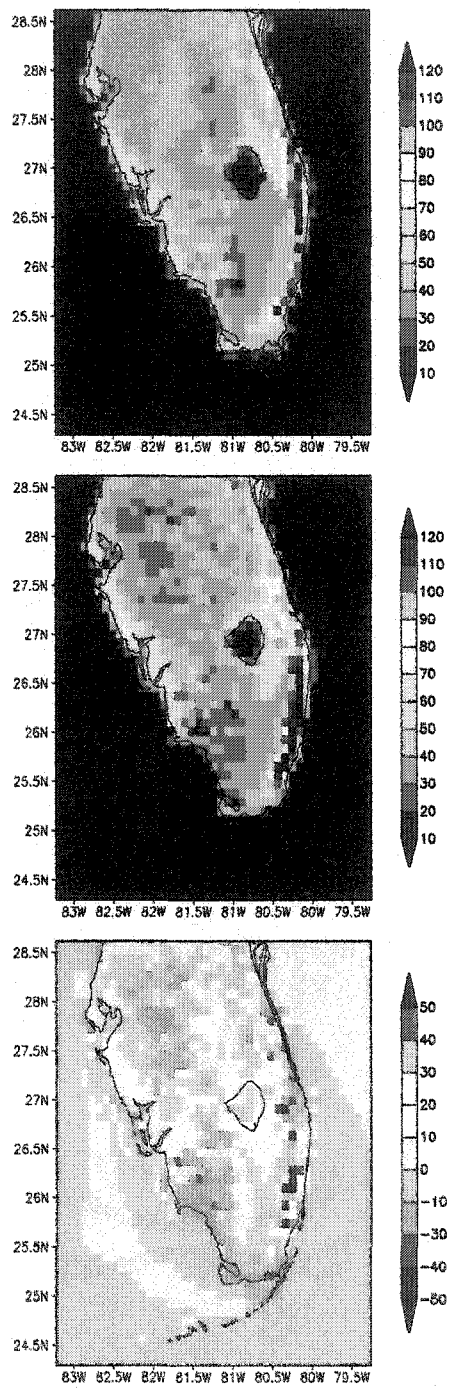

Figure 3.10. Same as in Figure 3.6, except for the simulations of Jul-Aug 1994.

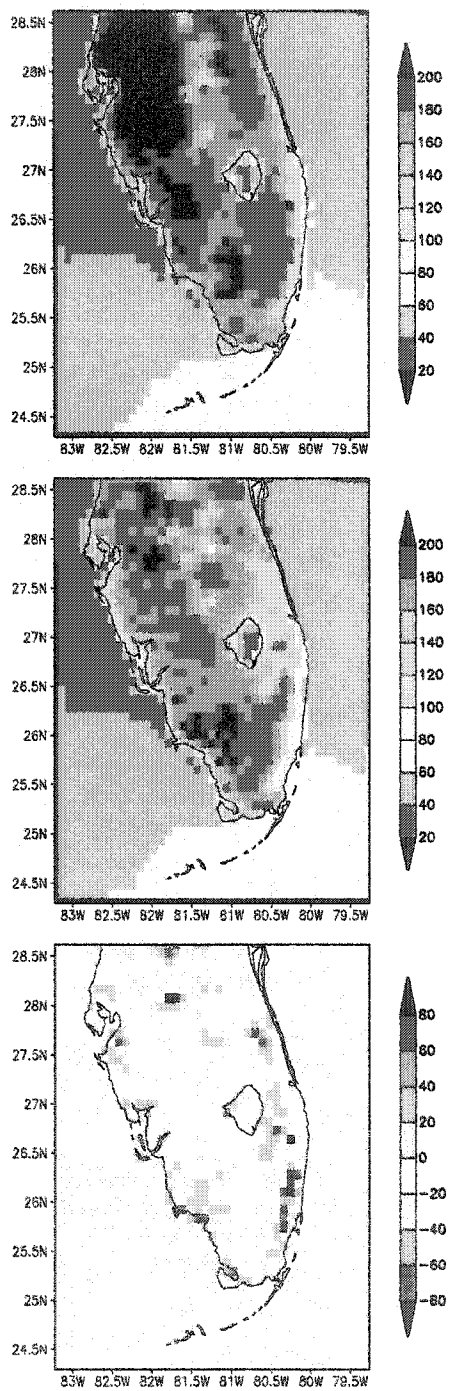

Figure 3.11. Same as in Figure 3.10, except for latent heat flux.

3.4 Shelter-Level Temperature

Figures 3.12 and 3.13 show the two-month average of the shelter-level daily maximum and minimum temperatures from the July-August 1989 simulations. While there is a great deal of spatial variability in these fields, the results show that daytime maximum generally increased when the current land cover was implemented. Significant decreases in daily minimum were realized along the interior axis of the peninsula. When averaged over all land grid points in the domain, the complete diurnal cycle of shelter-level temperature is amplified (Figure 3.14a), with an increase in the maximum of 0.31°C, and a decrease in the minimum of 0.26°C. This amplification is particularly apparent at locations where standing water has been drained, such as the grid point in the heart of the Kissimmee River basin (Figure 3.14b; grid point location marked by the "X" in Figures 3.12 and 3.13. At this particular point, the nighttime minimum is nearly four degrees cooler in the current land-cover scenario, and the daytime maximum is warmer and phase-shifted considerably earlier in time.

The phase-shifted, cooler maximum in the natural case is consistent with the fact that the standing water present at this location results in a higher effective thermal inertia of the land surface relative to the current case. For a typical diurnal cycle in the natural case, more net radiation is expended after sunrise to heat the standing water, thus delaying the commencement of sensible heating of the lower atmosphere. A comparison of the daytime (1200-0000 UTC) ground heat flux in the two cases (Figure 3.15), verifies this. At locations in the Kissimmee River valley, the ground heat flux is significantly larger in the natural land-cover case, because the standing water more efficiently absorbs and conducts the incident net radiation than the soil/vegetation surface in the current case.

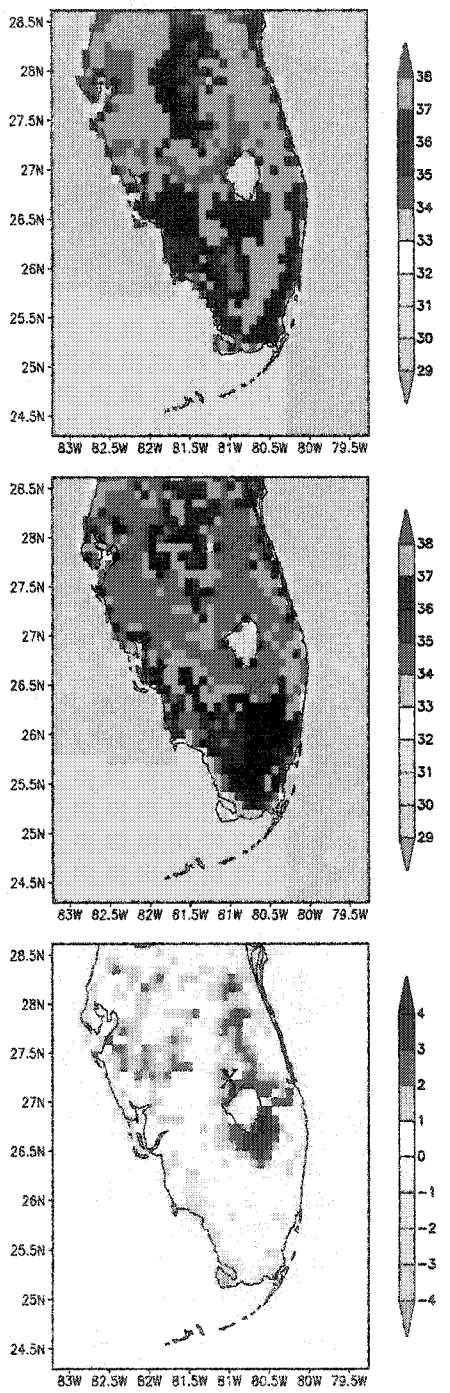

Figure 3.12. Two-month average of the daily maximum shelter-level temperature (°C) from the model simulations of Jul-Aug 1989 with (top) natural land cover, (middle) current land cover.

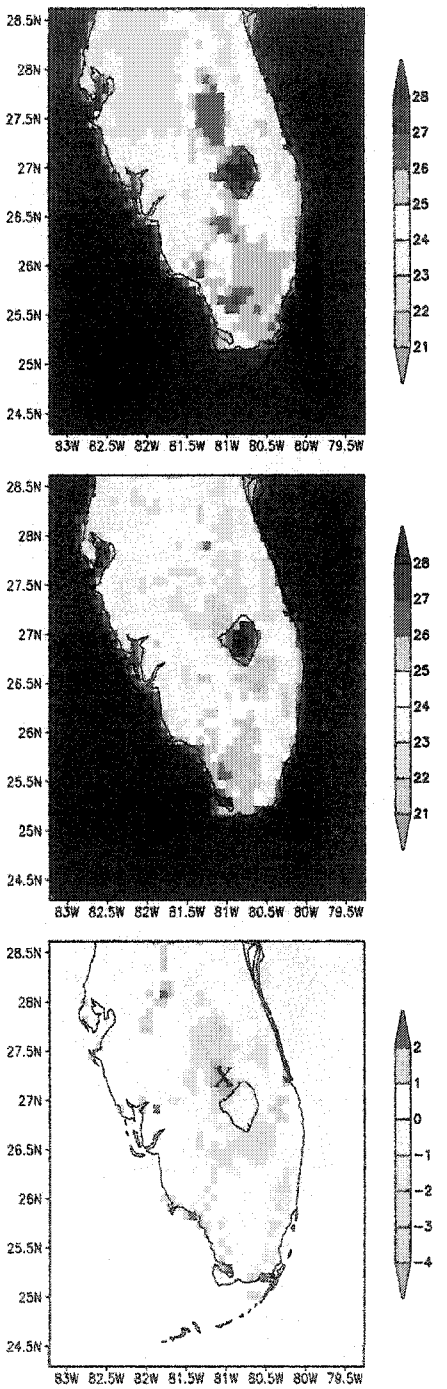

Figure 3.13. Same as in Figure 3.12, except for daily minimum temperature.

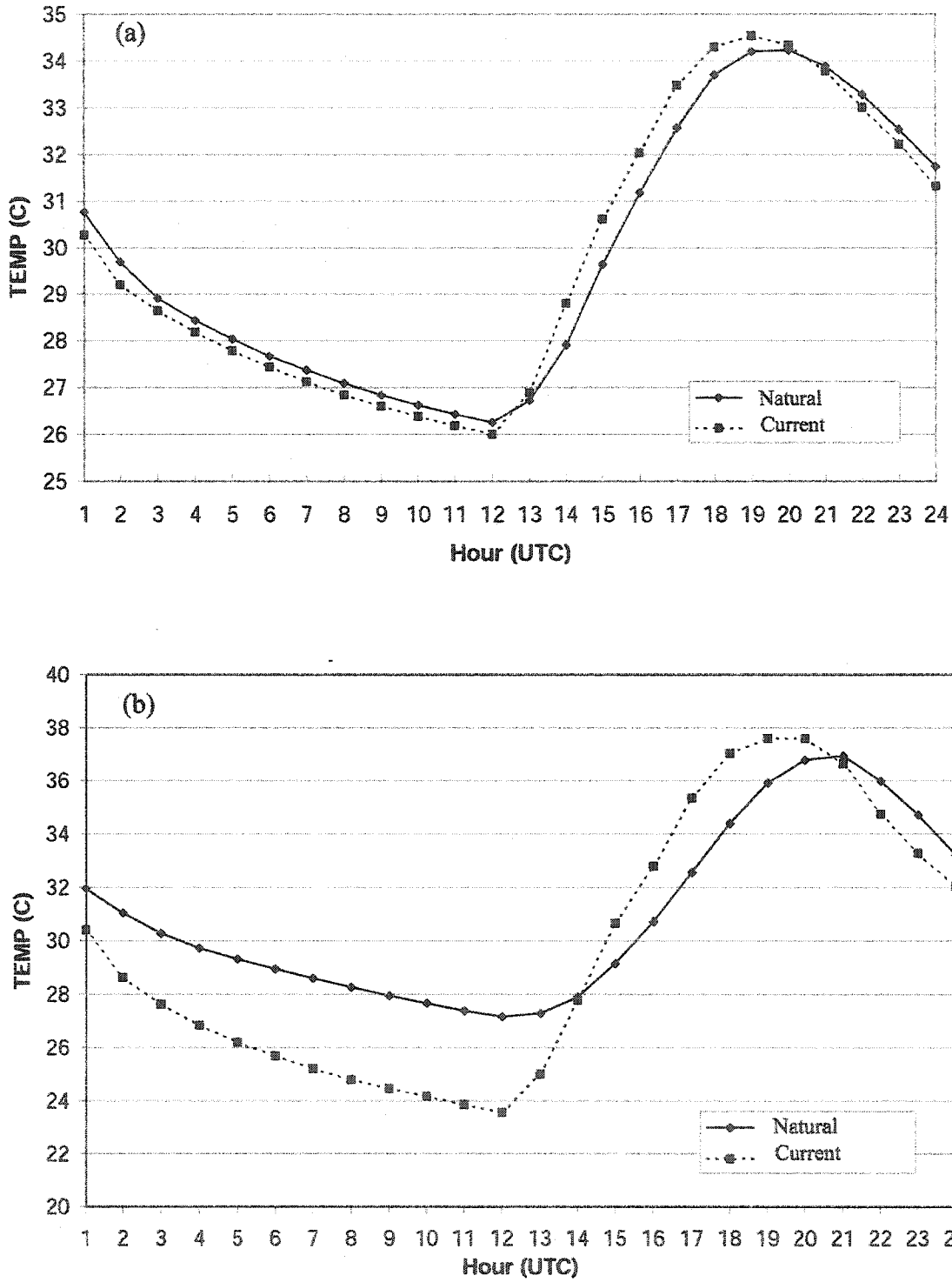

Figure 3.14. Two-month average of the diurnal cycle of shelter-level temperature (°C) from the model simulations for Jul-Aug 1989 (a) averaged over all land grid points in the model domain and (b) for the grid point marked by the "X" in Figures 3.12 and 3.13.

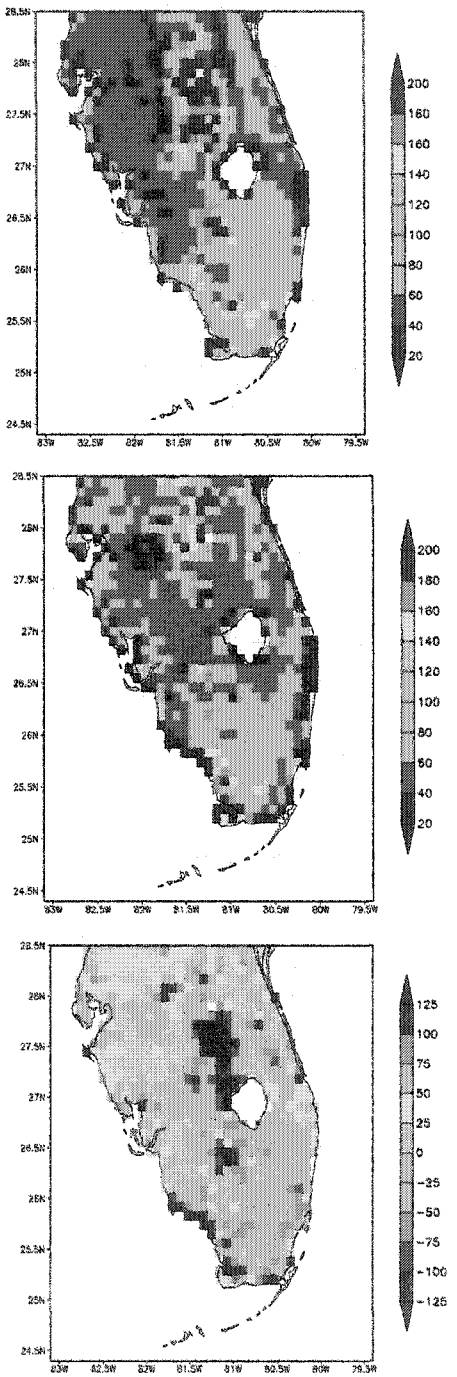

Figure 3.15. Two-month average of the daytime (1200-0000 UTC) ground heat flux from the model simulations of Jul-Aug 1989. Panel convention as above.

3.5 Near-Surface Mesoscale Flow and the Sea-Breeze Circulations

During mid-summer, light easterly flow is typically present over the central and southern Florida peninsula, in association with the western extension of the dominant high-pressure system over the subtropical Atlantic Ocean. The flow pattern is characterized by general synoptic quiescence. Under this regime, the sea breezes are often the most meteorologically significant features, and on many afternoons, convection occurs in association with them. During the typical diurnal cycle, breezes form on both the east and west coasts of the peninsula, and penetrate inland with the intensification of afternoon heating. The west coast front typically does not penetrate as far inland as the east coast one, due to interaction with the large-scale easterly flow. However, this interaction usually results in stronger convergence and greater precipitation along the west coast breeze. According to an analysis of radar data by Michaels et al. (1987) convection begins first over the western side of the peninsula, and that is typically where the greatest warm-season rainfall occurs. This maximum is apparent in the observations shown in Figure 3.1, as well as the model results shown in Figures 3.2-3.4. Pielke (1974) provides observational and modeling evidence that outlines these patterns and this sequence of events as the typical diurnal evolution of the sea breezes over the Florida peninsula. This scenario is also consistent with the typical patterns of sea-breeze convective activity described by Blanchard and Lopez (1985).

The fundamental mechanism behind the formation and maintenance of the sea breezes is the gradient of surface sensible heat flux between land and sea. Thus, it stands to reason that changes in the nature of the underlying land surface, which serve to alter the spatial patterns of sensible heat flux, could have a direct impact on the structure and

diurnal evolution of the sea breezes. Spatial heterogeneities in land cover could also force (inland) mesoscale flow features, which could also impact the evolution of convection over the interior peninsula and interact with the sea breezes. The ability of surface heterogeneities to force mesoscale circulations can be shown mathematically following Pielke (2001). First, consider the hydrostatic equation for shallow features:

$$\frac{\partial p'}{\partial z} = \frac{\theta'}{\alpha_o \theta_o} g \tag{3.1}$$

where $\alpha_o = 1/\rho_o$ and ρ_o is the base state mean density, p′ is the mesoscale perturbation pressure and θ′ is the mesoscale perturbation potential temperature. Taking the derivative of (3.1) with respect to the horizontal and permuting the order of operations on the left-hand side gives:

$$\frac{\partial}{\partial z}(\nabla_h p') = \frac{g}{\alpha_o \theta_o} \nabla_h \theta' \tag{3.2}$$

If (3.2) is integrated from the surface to the top (z_i) of the planetary boundary layer (PBL), and the PBL is assumed to be well mixed with respect to θ, then:

$$\nabla_h p'\Big|_{Zi} - \nabla_h p'\Big|_{z\ =\ surface} = \frac{g z_i}{\alpha_o \theta_o} \nabla_h \theta' \tag{3.3}$$

Differentiating (3.3) is with respect to time gives:

$$\frac{\partial}{\partial t}\nabla_h p'\Big|_{Zi} - \frac{\partial}{\partial t}\nabla_h \bar{p}\Big|_{z\,=\,surface} = \frac{g}{\theta_o}\left\{\theta'\nabla_h\frac{\partial z_i}{\partial t} + z_i\nabla_h\frac{\partial \theta'}{\partial t}\right\} \tag{3.4}$$

Now consider that the acceleration of the horizontal wind is a function of the horizontal pressure gradient:

$$\frac{\partial \vec{V}'}{\partial t} \sim \alpha_o \nabla_h p' \tag{3.5}$$

Deardorff (1974) suggested that the local tendency of boundary layer growth can be described by:

$$\frac{\partial z_i}{\partial t} \sim H^{2/3} z_i^{-4/3} \tag{3.6}$$

where H is the surface sensible heat flux. The local diabatic heating rate is also a function of the surface sensible heat flux:

$$\frac{\partial \theta}{\partial t} \sim \frac{\partial}{\partial z}\frac{H}{\rho C_p} \tag{3.7}$$

If Equations (3.5)-(3.7) are substituted into Equation (3.4), the relationship of spatial gradients of H to boundary-layer circulations is demonstrated. Furthermore gradients of H are a direct function of spatial heterogeneities of land-cover properties. Therefore, surface heterogeneities can force local circulations in the PBL.

Figure 3.16 shows the July-August average of the near-surface (10 meter) wind field valid at 1600 UTC with the derived surface divergence field, for the 1989 pair of simulations. The time of day chosen for analysis (1600 UTC) corresponds closely to local solar noon. The pattern shown is typical for the near-surface wind field just before convection initiates (Michaels et al. 1987). Thus, at this time of day, the effects of the land surface are readily observable without complicating factors that arise after convective outflows begin to impact the near-surface mesoscale flow patterns. Note the divergence/convergence couplet that is associated with acceleration toward the more intensely heated land along the coastlines. Of particular interest here is the spatially coherent axis of surface divergence (positive values) located along the inundated flood plain of the Kissimmee River in the natural land-cover case (left panel).

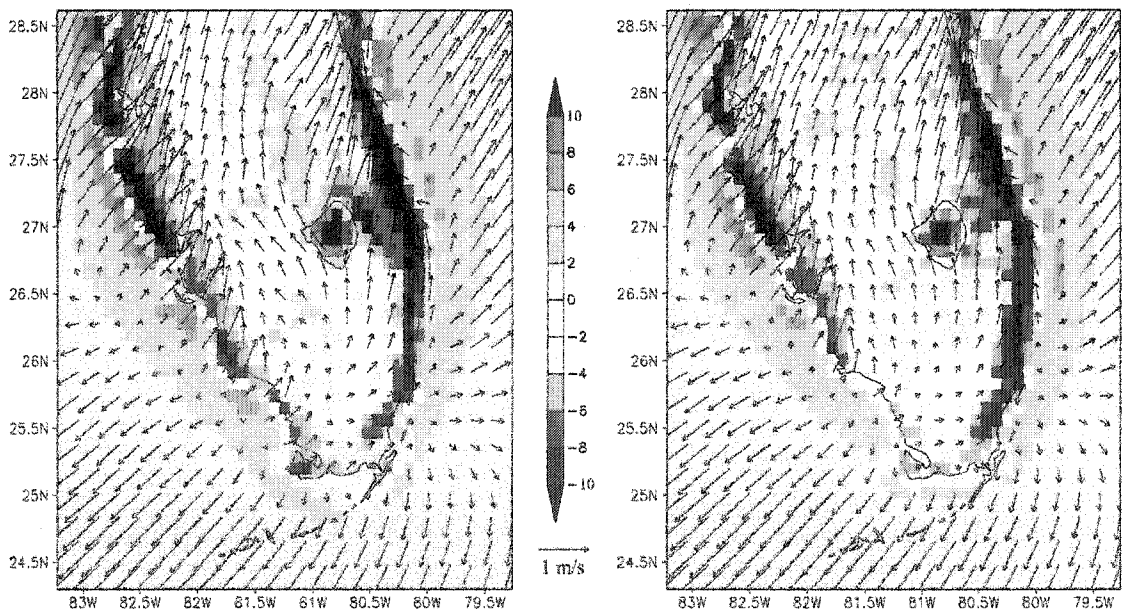

Figure 3.16. Two-month average of the 1600 UTC horizontal wind (vectors; m s^{-1}) and the derived surface divergence (color shaded; 10^5 s^{-1}) from the Jul-Aug 1989 simulation with the (left) natural land cover and (right) current land cover.

The difference field of the divergence from the two land-cover cases (Figure 3.17; shaded field) indicates decreased values over the Kissimmee River valley. This signature is also indicated by convergence of the vectors in the wind vectors, which are overlain on the shaded divergence field. Negative values in the divergence difference field shown in Fig. 3.17 (and convergence of the accompanying vectors) can result from three different possibilities. The first possibility is that a grid point with convergent flow in both land-cover cases became more convergent when the current land cover was implemented (i.e., negative values became more negative). Second, a grid point that was divergent (positive) in the natural case became convergent (negative) when the current land cover was implemented. The final possibility is that a divergent grid cell in the natural case became *less* divergent (though not convergent) in the current case. Thus, the coherent axis of negative values and converging vectors along the Kissimmee River valley in the difference field (Figure 3.17) represents the fact that when the natural land cover was replaced with the current data, the near-surface flow over this area became either less divergent or convergent. Close inspection of Figure 3.16 shows that over a number of grid cells in the vicinity of the Kissimmee River, divergent flow in the natural case became convergent in the current case. This feature appears to be spatially consistent with several other features discussed above; most notably, the distinct axis of increase in the model rainfall fields (bottom panels of Figures 3.2-3.4). In addition, the feature is spatially aligned with a distinct axis of increase in sensible heat flux seen in Figures 3.6, 3.8, and 3.10, and the axis of increased maximum temperature shown in Figure 3.12. These results suggest that the changes seen in these fields are related through a physical-

dynamical framework that is directly attributable to the difference in the land-cover class between the two simulations.

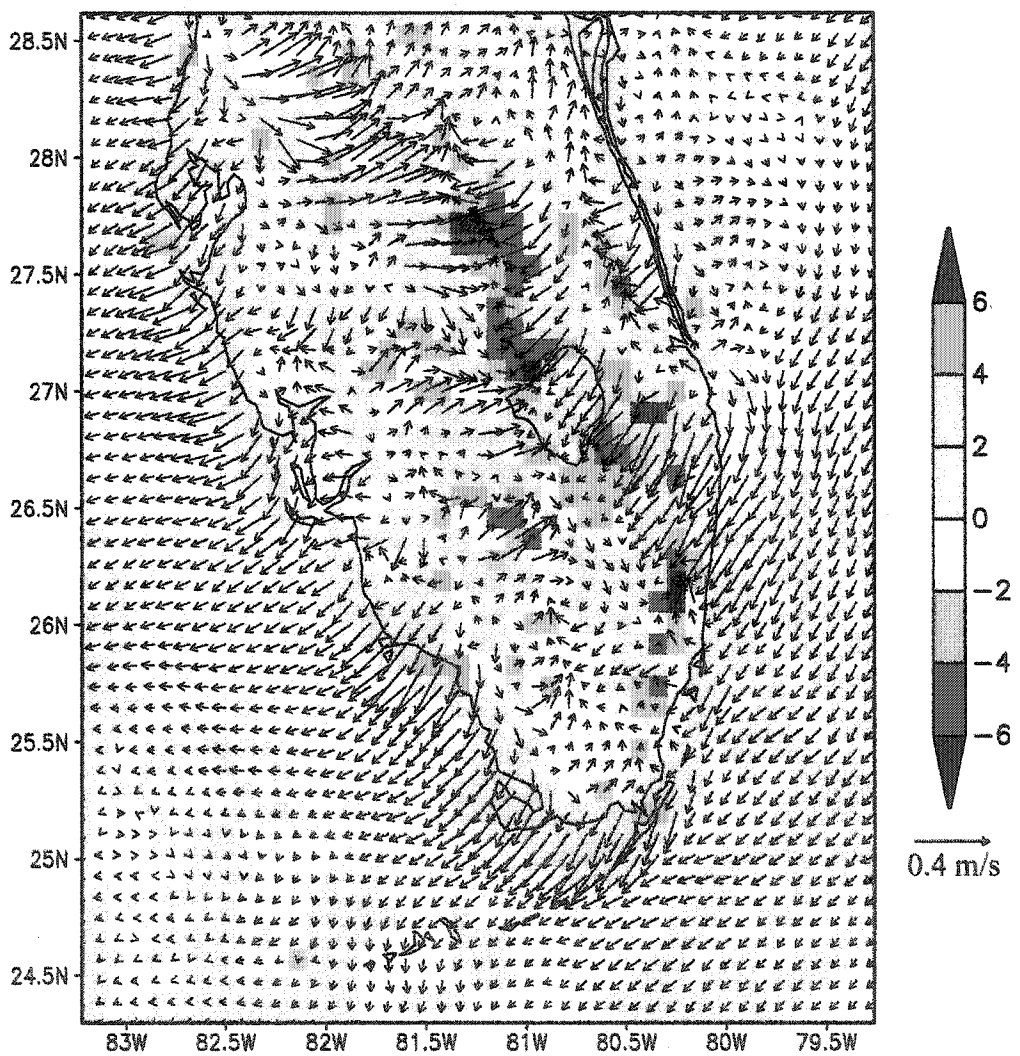

Figure 3.17. Difference (natural minus current) of the fields shown in Figure 3.16.

Vertical cross sections of the low-level wind flow in the x-z plane were constructed to complement Figures 3.16 and 3.17. The cross sections (Figure 3.18) represent the two-month average of the 1600 UTC u and w wind components over the lowest 3000 m of the model domain. The data shown in Figure 3.18 are the average of all such x-z planes over the latitude belt from 26.5°N to 28°N. The purpose of averaging in the north-south direction was to capture the general flow pattern associated with the distinct axis of increased precipitation along the Kissimmee River valley and the juxtaposed axes of decrease. The concentrated areas of upward vertical velocity associated with the sea breezes are shown along the flanks of the domain in both land-cover cases, along with a broad area of subsidence in the interior. Note the marked decrease in the upward vertical velocities along the upward branches of the sea-breeze circulations in the accompanying difference field (Figure 3.19). Because these were areas of upward motion in both land-cover scenarios and the magnitude of that motion was greater in the natural land-cover case, the decrease of upward motion is indicated as downward motion in the difference field (note the regions centered around 82.2°W and 80.4°W in Figure 3.18). Over the central part of the domain, the general subsidence was decreased in the current case. This decrease in downward motion is shown as relative upward motion in Figure 3.19 (between approximately 80.9°W and 81.7°W), because the absolute magnitude of the subsidence is greater for the natural case. It is suggested that the area of generalized subsidence in the natural case is associated with the outward-directed (divergent) horizontal flow over the Kissimmee River basin seen in the left panel of Figure 3.16. Recall that the coherent axis of horizontal divergence over this area is greatly reduced or even replaced with weak convergence in the current case. Mass

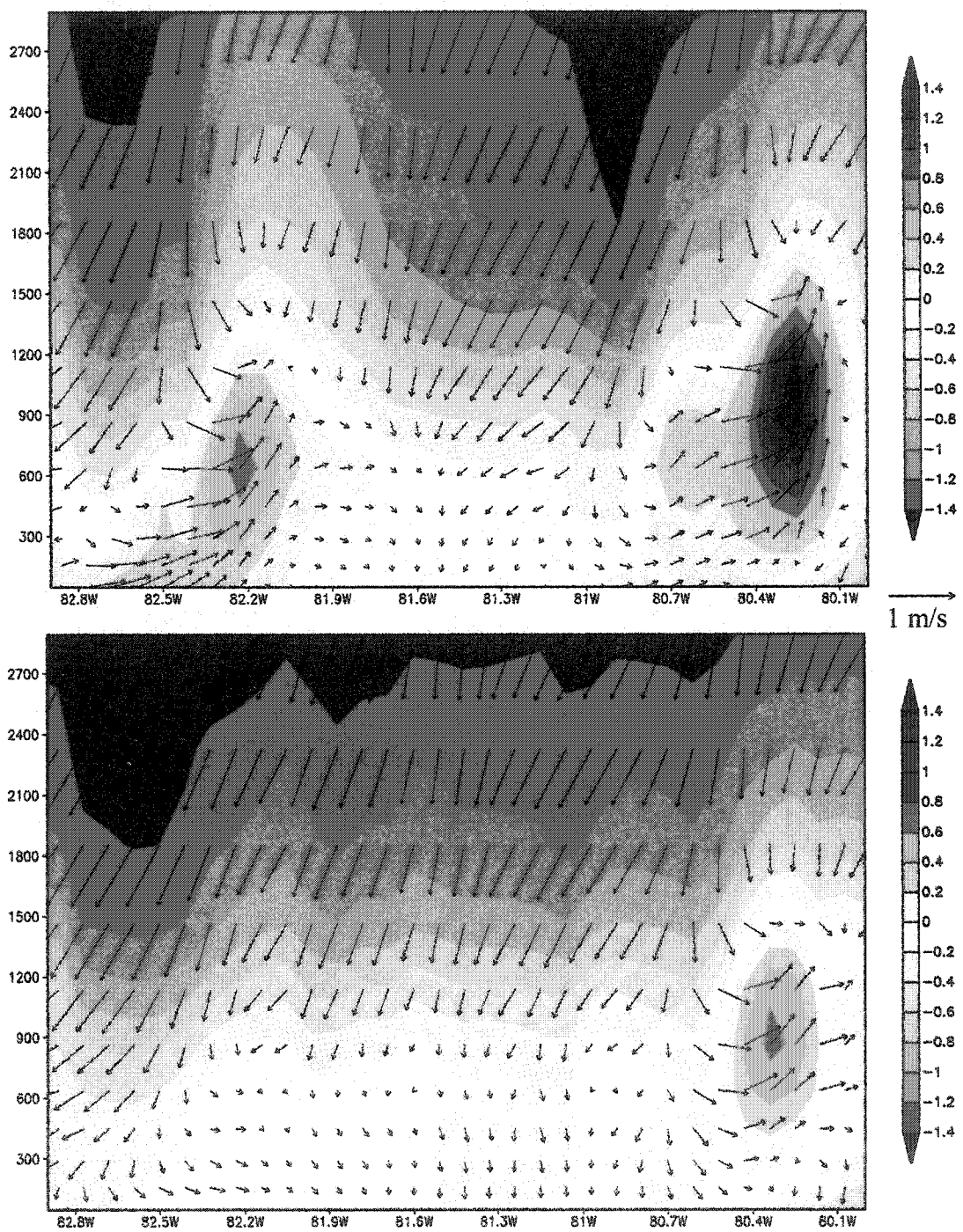

Figure 3.18. Two-month average of the 1600 UTC u-w wind component (vectors in units of m s^{-1} because w component is multiplied by 100 for visual emphasis) and vertical velocity (cm s^{-1}; color shaded) from simulations for Jul-Aug 1989 with (top) natural land cover and (bottom) current land cover. The vertical cross section is the average of all vertical cross sections in the model domain from 26.5°N to 28°N.

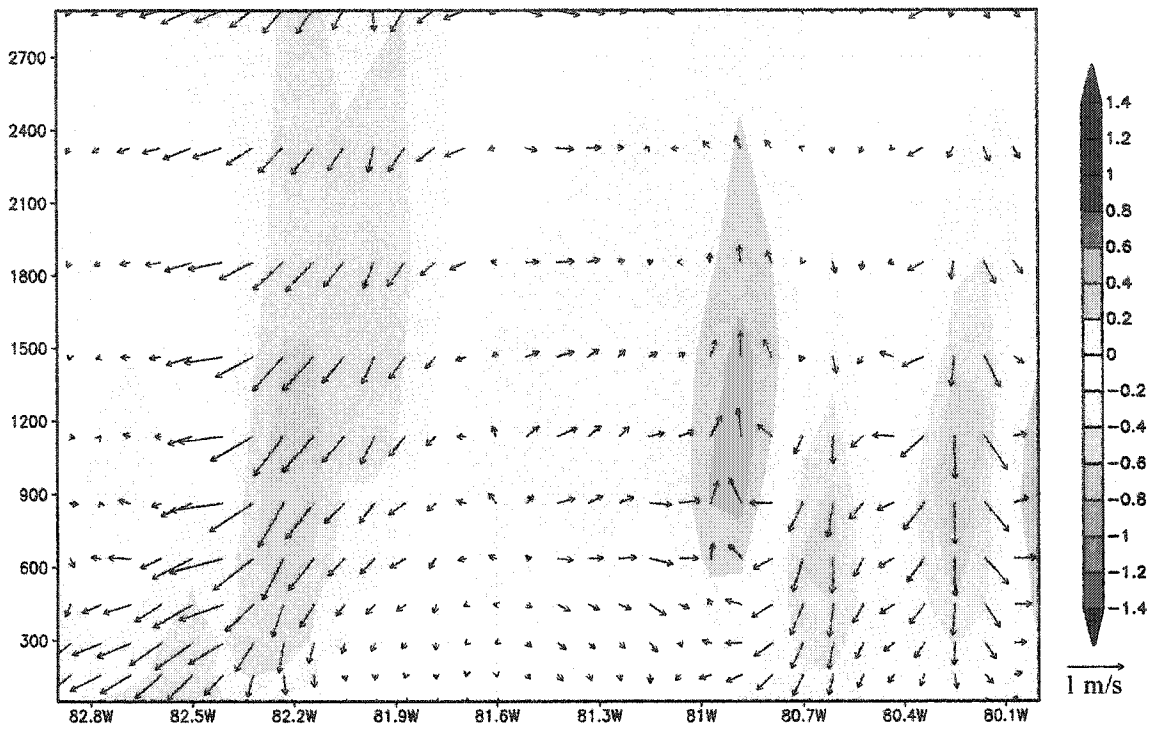

Figure 3.19. Difference (current minus natural) of the fields shown in Figure 3.18.

continuity arguments can be invoked to suggest that a decrease in compensating subsidence could occur over that part of the domain where surface divergence is weakened.

The characteristics of the changes in the low-level horizontal wind field patterns and associated vertical circulations appear to be associated with the changes in sensible heat flux patterns shown in Figures 3.6, 3.8, and 3.10. In the framework of the natural land-cover scenario, the expanse of the Kissimmee River basin may have resulted in a divergent, outward-directed mesoscale flow, because sensible heating increased outward from the center of the water covered basin. This proposed mechanism is physically the same as that which drives the sea-breeze circulations, as outlined mathematically in

Equations. (3.1)-(3.7). In this particular case, the sensible heating gradient is associated with spatial gradients in the thermal properties of the land surface. When the current land-cover data, wherein the inundated flood plain of the Kissimmee River basin has been drained, is implemented in the model configuration, the sensible heat flux over this area is increased, which in turn decreases the horizontal gradient of the flux along the periphery of the basin, relative to the natural case. Thus, the mechanism suggested to force this mesoscale flow in the natural land-cover case would be diminished or removed when the current data are implemented. This effect is visually apparent in both the difference field for the horizontal flow (Figure 3.17) and the difference field for the vertical cross sections (Figure 3.19).

If the outward-directed mesoscale breeze forced by this mechanism in the natural case is considered within the context of the sea breezes, it stands to reason that it could serve to enhance the horizontal convergence and upward motion along the upward flanks of the circulations, because the afternoon sea-breeze fronts are often positioned immediately either side of the Kissimmee River valley, and their associated near-surface flow is directed inward, towards the central part of the peninsula. This constructive reinforcement mechanism would be either decreased or eliminated when the current land-cover data are implemented.

Given that preferred areas of mesoscale vertical motions can be reflected as mesoscale spatial variations in convective rainfall, it is not surprising that those areas along the sea-breeze fronts that are marked by decreased upward motion are consistent with the axes of decreased precipitation shown in Figures 3.2-3.4, whereas the decreased subsidence over the interior is associated with increased precipitation. This spatial

pattern of the changes in the accumulated rainfall between land-cover scenarios, readily apparent in a visual inspection of the model fields, is consistent among all the simulated periods. The resulting grid average rainfall decrease is also consistent among the three periods. As discussed above, the spatial redistribution of convective precipitation results in an overall grid average decrease of 10% to 12% (or about 2.6 M acre-ft) for all simulated periods. Therefore, it is suggested that the physical-dynamical mechanism outlined above, directly attributable to changing in the land cover within the pair of simulations, is the key factor not only in determining the redistribution of convective rainfall, but also in the resulting regional decrease.

3.6 Sensitivity Tests

In this section, the sensitivity of the results to various aspects of the model setup is explored. Using the default configuration as the control, the July-August 1989 pair of simulations was repeated with three alternative model configurations. The first alternative used the Chen-Cotton radiative transfer scheme (Chen and Cotton 1983), and the second used the Kuo convective parameterization. The third alternative used the default physics options (Mahrer-Pielke radiation and Kuo convection), but at a 40 km horizontal grid spacing. Using both the default physics and default grid spacing, three additional experiments were conducted to examine the impact of initial soil moisture and the distribution of SST. The first of these experiment used alternative initial soil moisture, the second an alternative SST distribution, and the third included both of these alternatives.

The factors explored in this sensitivity analysis were deemed among those most important to the nature of the model fields examined in this study (e.g., the surface energy budget and convective precipitation). However, these factors are by practical necessity a limited subset of those that could impact the results. Numerous other aspects of the model setup could potentially influence the results. For example, these simulations did not employ explicit cloud microphysics, because the resulting precipitation totals with use of a convective parameterization alone appeared adequate to capture the magnitude of the observed rainfall.

Much of the convective activity over the Florida peninsula during July and August is initiated by the sea breezes, which are surface-forced circulations. Thus, it is reasonable to expect that the parameterized radiation, which provides the primary forcing for the surface sensible heat, could have an impact on the nature of those circulations, and hence the distribution of convective rainfall. The Mahrer-Pielke scheme (the default) accounts for the presence of water vapor, but it does not explicitly account for cloud liquid water or ice in determining the radiative transfer. However, during the typical diurnal scenario, circulations such as the sea breezes are often well developed before the onset of significant convective cloudiness and rainfall. Thus, it is suggested that the Mahrer-Pielke scheme, which is desirable because of its computational efficiency, is adequate for the simulations presented in this study. Nevertheless, it was deemed prudent to examine the impact of using an alternative, such as the Chen-Cotton scheme, which does incorporate the effects of cloud water and ice. As Figure 3.20a illustrates, the spatial distribution of the precipitation difference field is quite similar to the difference

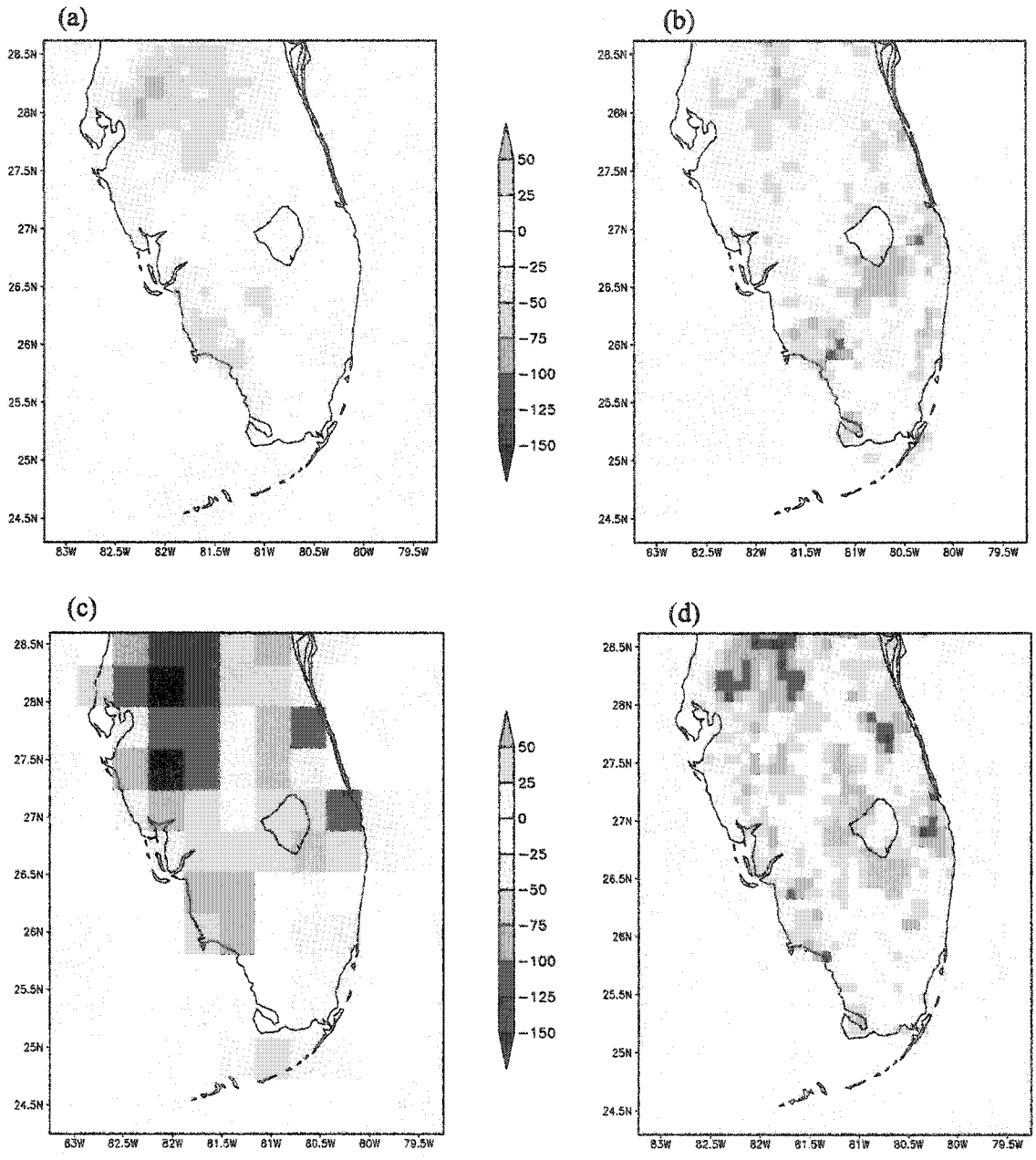

Figure 3.20. Difference field of accumulated precipitation (mm; current minus natural land cover case) from the sensitivity simulations for Jul-Aug 1989 with (a) the Chen-Cotton radiative transfer scheme, (b) the Kuo convective parameterization, (c) default physics, but at 40 km grid spacing, and (d) default physics and grid spacing, but with weekly-observed SST and VIC model soil moisture initialization.

field from the control simulations (bottom panel of Figure 3.3). The axis of increased rainfall along the Kissimmee River valley is not as distinct as in the control case, but the general pattern of increase over the interior peninsula and decreases on adjacent sides is realized with the use of the Chen-Cotton scheme. The grid-average decrease corresponding to Figure 3.20a is 18% of the grid average value of the natural case rainfall. The magnitude of this decrease is somewhat greater than the control decrease, which was 11%. This result indicates that using a radiative transfer scheme that accounts for cloud water and ice magnified the impact of land-cover change. A detailed investigation of the possible reasons for the difference with the control is not the primary focus of this study. The point emphasized here is that, even with an alternative radiation treatment, the difference realized because of changing the land cover is qualitatively similar and quantitatively not far removed.

The model configuration with the Kuo scheme produced significantly less precipitation when the current land cover was implemented (Figure 3.20b). The grid average decrease is 13% of the natural case grid-average total. This percentage decrease is very close to the percentage decrease in the control experiments, despite the fact that the overall Kuo scheme totals for both land-cover cases (not shown here) were significantly less than those produced by the Kain-Fritsch configuration. For the natural land-cover case, the Kuo configuration yielded a grid-average total of 198 mm, whereas for the current case this total was 173 mm. The Kain-Fritsch scheme yielded 342 mm for the natural case, and 305 mm for the current case. It is also noted that the large decrease when the Kuo scheme is implemented is in agreement with the difference between the 1973 totals shown here and those shown by Pielke et al. (1999).

The horizontal grid spacing should significantly impact the results, regardless of the choices for the various physical parameterizations. Furthermore, the contributions of the physical parameterizations to the grid-scale tendencies are themselves strongly influenced by the horizontal grid spacing. In other words, the horizontal grid spacing and the options selected for the physical parameterizations cannot be considered as mutually exclusive categories in this sensitivity analysis, because these factors are inherently interdependent. This interdependency is especially strong in the case of the convective parameterization. In fact, convective schemes are designed for a particular range of grid spacing. Figure 3.20c shows that the results at 40 km, produced with the same physics options used in the control (Kain-Fritsch convection and Mahrer-Pielke radiation), yielded a similar pattern of change in convective rainfall when the natural land cover was replaced with the current dataset. The percentage decrease, 9.5%, is close to the 11% noted for the control (10 km) case. The precipitation totals from both land-cover scenarios (not shown here) were considerably larger than for the 10 km control set, with local maxima exceeding 700 mm. The 10 km maxima were less than 450 mm (see Figure 3.3 top two panels). This indicates that the 10 km totals were in much closer agreement with the observed magnitudes (Figure 3.1). Regardless, the important point emphasized here again is that the difference in precipitation totals between land-cover cases *at either resolution* is qualitatively and quantitatively (as a percentage change of the natural case grid-average amount) similar. Here, this sensitivity was evaluated by comparing the results from a model configuration with larger grid spacing than that assigned to the control in order to provide results that span the range of grid spacing for which the Kain-Fritsch convective parameterization was designed. However, it is

acknowledged that the results could also differ if the model grid spacing were smaller than the 10 km control value. At grid increment sizes much below this value, where the model setup could be configured to resolve convection explicitly, the representation of circulations such as the sea breezes could change markedly, and the results could vary in a highly nonlinear manner with small changes in grid spacing (Weaver et al. 2002).

Other aspects of the model configuration, in addition to the physical parameterizations and grid spacing, could significantly influence the impacts of changing the land cover. The specification of SST and initial soil moisture are two factors that are believed to have particularly significant impacts on warm season convective rainfall in regional/seasonal climate modeling simulations (Walker and Rowntree 1977; Mintz 1984; Atlas et al. 1993; Paegle et al. 1996; Fennessey and Shukla 1999). Using the July-August 1989 simulations with default physics and grid spacing as the experimental control, a factorial set of experiments was designed to explore these sensitivities. Note that any effects of SST anomalies at remote locations, such as the equatorial Pacific, are realized through the lateral boundary conditions as specified directly by the NCEP/NCAR Reanalysis data. As such, the question of interest here concerns SSTs in the adjacent coastal waters of the RAMS domain, and what impact their specification may have on the resulting distribution of convective precipitation on the regional model grid.

In the control simulations, the SSTs were specified from the monthly climatological dataset referenced in Chapter 2. For the sensitivity studies, a weekly-observed dataset provided by NCEP (Reynolds and Smith 1994) was implemented. For the period July-August 1989, the two-month average of the weekly-observed fields is

quite different from the corresponding climatological data (Figure 3.21). Note that the Gulf Stream is locally several degrees warmer. In addition, the climatological dataset, which combines many years of multiple observations, is spatially smoother than the weekly data, which are based on a course-grid objective analysis of limited observational data, primarily from satellite overpasses.

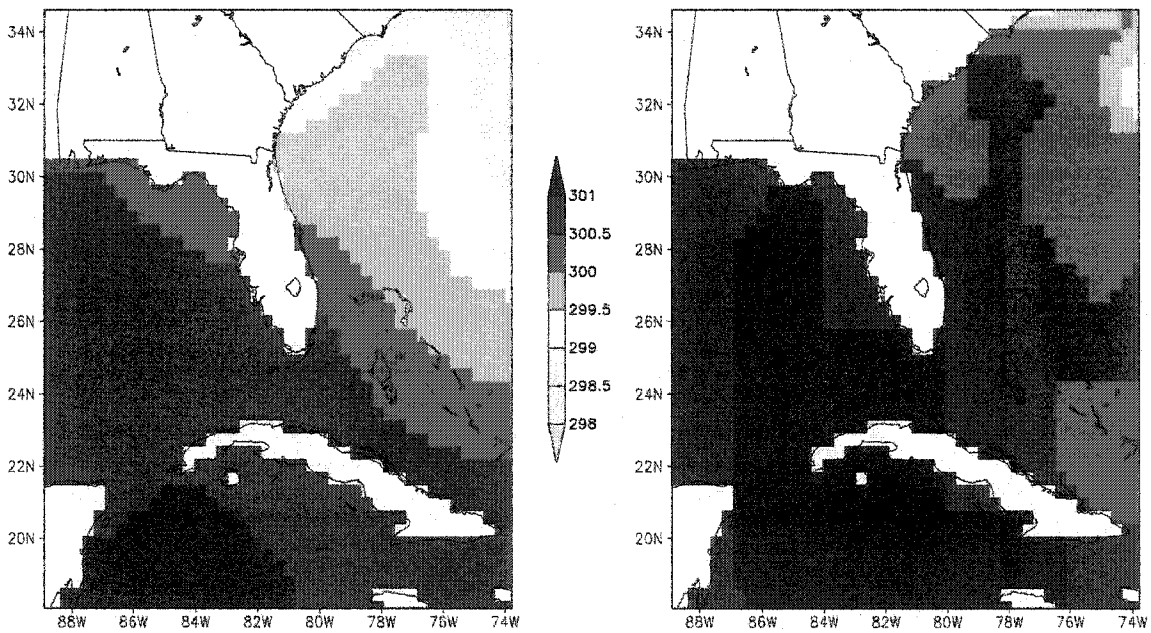

Figure 3.21. Jul-Aug average SST (K) from the (left) weekly observed NCEP data during 1989 and (right) the NCEP monthly climatological dataset.

For the sensitivity tests involving initial soil moisture, the alternative initialization was derived from the dataset produced by the University of Washington with the Variable Infiltration Capacity (VIC) model (recall that this archive is used to provide the

default soil moisture initialization for the freeze simulations that are presented in Chapter 4). Figure 3.22 shows the VIC-derived initial soil moisture for both the natural and current land-cover cases. Note that the initial field is different for the two different land-cover cases because of the imposed saturation condition for swamp and marsh classes. The spatial distribution of these classes is different between the two land-cover datasets. Also note the large area of the Everglades that has volumetric water contents greater than 0.8, because the soils at most wetlands locations were designated as organics, which have a very large porosity (i.e., soil moisture saturation value). As discussed by Baker et al. (2001), the unique distribution of properties on the Florida peninsula could have substantial impacts on the nature of local circulations and the interaction of those circulations with the sea breezes.

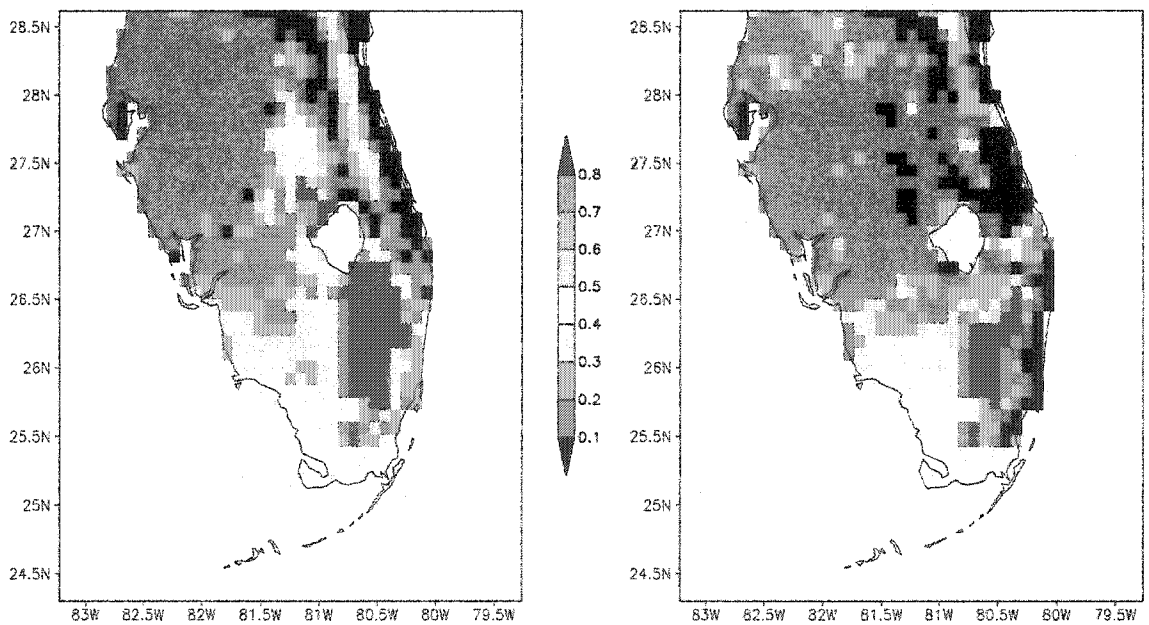

Figure 3.22. Initial soil moisture (m^3 m^{-3}) as derived from the VIC model for the (left) natural land cover and (right) current land cover.

Figure 3.20d, the experiment that incorporates both the SST and soil moisture alternatives, is consistent with the other results shown in Figure 3.20. Substantial increases in precipitation directly over the Kissimmee River basin and decreases along the adjacent sea-breeze fronts are realized when the natural land cover is replaced with the current dataset. Figure 3.23 illustrates the grid-average rainfall (both land-cover scenarios) for the complete factorial set of SST and soil moisture experiments. There are substantial differences in the absolute totals among the experiments. However, the difference between land-cover scenarios *within a given sensitivity experiment* is consistent, lending further credence to the robustness of the impact of land-cover change on the simulated convective precipitation. The decrease relative to the natural case total in all experiments is in the range of 10% to 12%, which is nearly identical to the difference yielded by the control configuration.

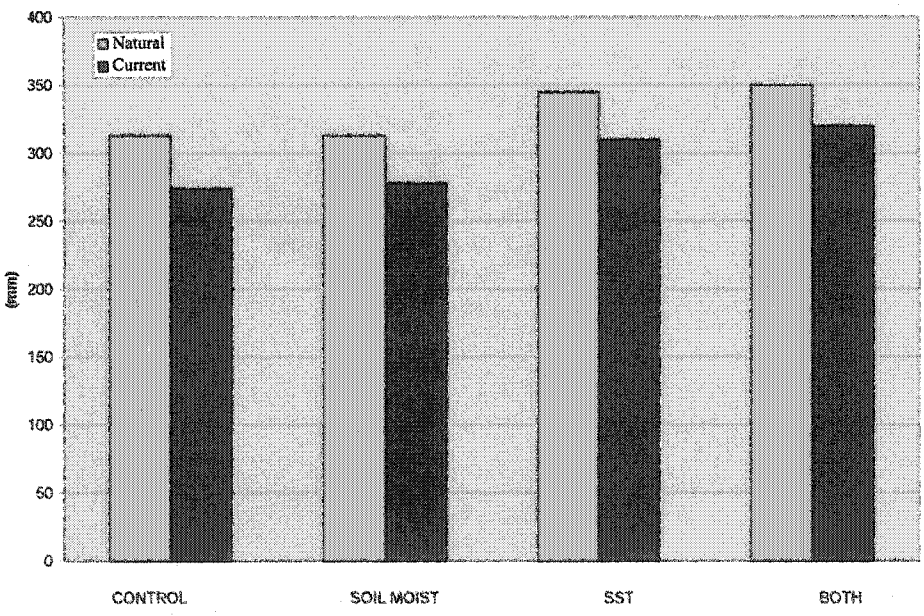

Figure 3.23. Grid average rainfall (mm) from the factorial set of SST and soil moisture experiments for both land-cover cases.

3.7 Comparison of the Model Results with Observations

In light of the expanded scope of the simulations shown in this present study, it is also of interest to revisit and expand upon the earlier observational data analysis provided by Pielke et al. (1999). In that work, time series of July-August accumulated rainfall and mean shelter-level temperature observations from Everglades City, Belle Glade, and Fort Lauderdale were presented. Here, data from these and several more stations (see Figure 3.24 for all station locations) were compiled to provide long-term, regional-average time series. Furthermore, the July-August regional-mean time series of daily maximum and minimum temperature are provided in lieu of the single mean observed value shown in the previous study.

Data for Arcadia, Belle Glade, Everglades City, and Fort Lauderdale through 2000 were obtained from the NOAA National Climatic Data Center (NCDC) United States Historical Climatology Network (USHCN) Serial 2000 Temperature and Precipitation Dataset. The analysis of rainfall data from these stations was based on the unadjusted area-edited (i.e., original or "raw") USHCN monthly total precipitation data. These totals were screened by NCDC to flag outliers, defined as three standard deviations beyond the mean for the period of record. Temperature data were subjected to NCDC USHCN 2000 quality assurance procedures. Specifically, these data are from the "area-edited, time of observation" data that have been adjusted for maximum and minimum system (instrumental) bias and station moves, with estimated values for missing and outlier data. However, these data were not subjected to the NCDC adjustment for urban heat island effects. The NCDC data for all July and August periods were nearly complete, with the few instances of missing data estimated from nearby station records.

The Florida Climate Center provided the data for the remaining stations shown in Figure 3.24, with the exception of rainfall data for HGS1, which was provided by the South Florida Water Management District.

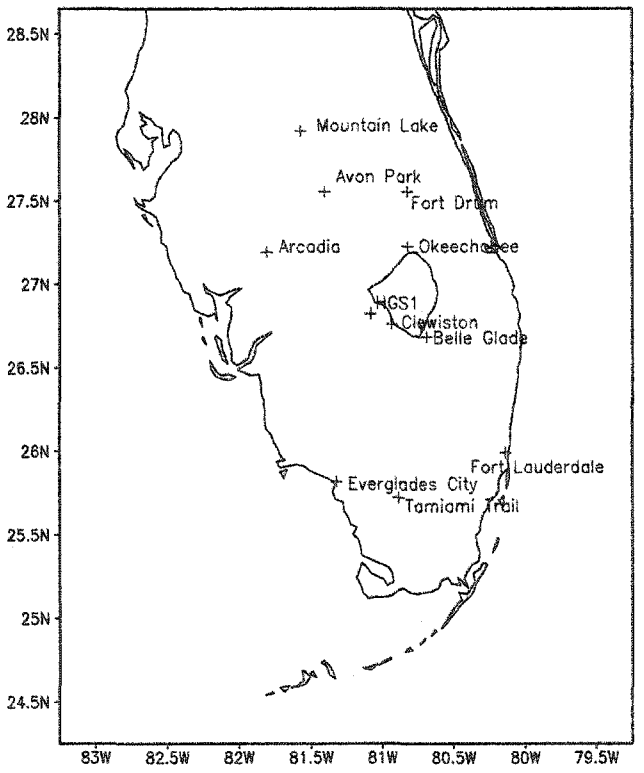

Figure 3.24. Locations of observation stations used to compile regional average long-term time series.

Several limitations should be considered when comparing this observational data with the model results. The observations are point-specific, whereas the model values represent an average over the finite area covered by the corresponding 10 km by 10 km grid cell. Thus, it is possible that an observation at a particular point, otherwise free of

error, will differ significantly from the corresponding model grid value, which itself could accurately portray the average over the grid cell area. To minimize this source of uncertainty, observational data were spatially averaged. The resulting composite time series were then used for comparison with model domain-average data. Additionally, instrument platforms for a given station designation were occasionally relocated (often by as much as several kilometers) during the long-term period of interest. It is plausible that such relocations could have a marked impact on the observed trend for a particular station. Finally, the number of stations with long-term records is rather limited, thereby constraining the sample size used to construct long-term time series of regional average data.

It must also be recognized that long-term time series of July-August observations and model simulations for *only three* July-August periods of interest that employ two different land-cover datasets that were constructed to capture the long-term change do not constitute two otherwise identical statistical samples. The valid times for the two different land-cover scenarios correspond roughly to the endpoints of the long-term observational time series provided, thus differing results within a pair of simulations may provide physical insight into the possible impact of long-term land-cover change on regional climate trends. However, a statistically consistent comparison with observations would require data from model simulations for every July-August period used to construct the observational time series. Furthermore, each of these simulations would have to employ a land-cover database valid for each of the individual July-August periods. Such datasets are not available, rendering this task beyond the scope of this work.

The time series of the regional-average July-August rainfall for the period 1924 to 2000 is shown in Figure 3.25 (insufficient data prevented a start date prior to 1924), along with a trend based on a linear regression that incorporates all years in the sample. The linear trend has a slope of -0.064, with a total decrease of 5 cm, or 12%, over the period of record. This is consistent with the percentage decrease of the domain-average convective precipitation from the model results. The standard error bars overlain on the raw time series indicate an appreciable spread among the individual station totals for a given July-August period, but this spread is typically less than 25% of the regional mean for its period. Eight out of the ten individual observation locations that were used to construct the regional-mean precipitation time series exhibited a decreasing trend in July-August precipitation during their respective observational period of record. Unfortunately, station spacing and location, along with the considerations discussed above, preclude a meaningful comparison of these individual trends with the data from the corresponding grid point locations within the model domain. The lack of long-term records for stations in the heart of the Kissimmee River valley in particular prohibits an analysis of whether this area has actually seen an *increase* in rainfall during the 20th Century. Prior to anthropogenic change, these areas were inaccessible wetlands that were devoid of meteorological observation sites.

Lack of available long-term records for temperature observations at all the sites shown in Figure 3.24 prohibited a start date prior to 1948 for the regional mean time series of maximum and minimum temperature (Figure 3.26). However, clear trends emerge in the available data. The time series for both the July-August daily maximum and minimum temperatures indicate warming. The trend from linear regression has a

slope of 0.011 (0.009) degrees per year, with a magnitude of 0.57°C (0.46°C) for the maximum (minimum) temperature increase over the period 1948-2000. The maximum temperature trend is in reasonable agreement with the 0.31°C increase in the grid-average model maximum temperature that resulted from the replacement of natural land cover with the current dataset (Figure 3.12). However, the grid-average model minimum (Figure 3.13) decreased slightly (-0.26°C) in response to changing the land cover.

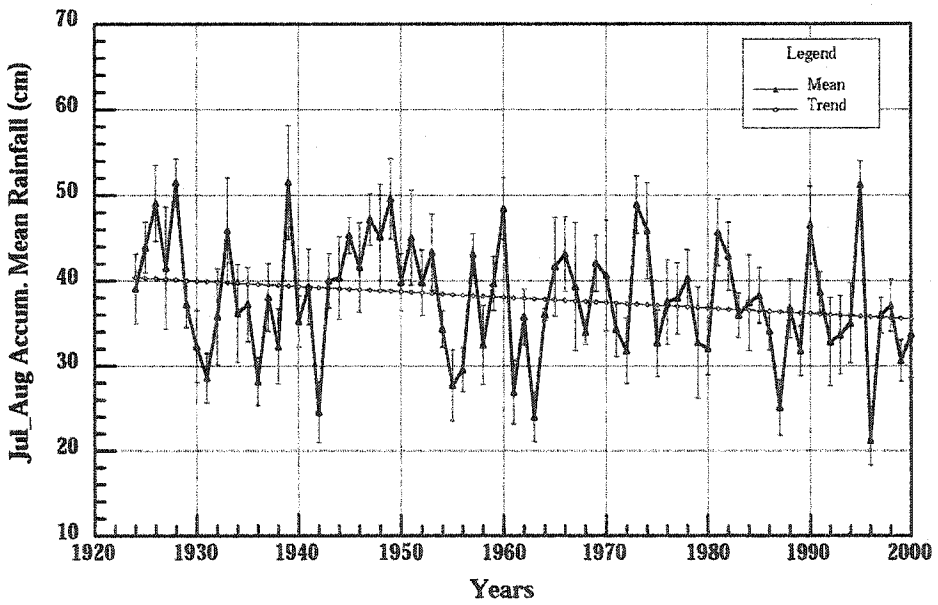

Figure 3.25. Regional-average time series of accumulated rainfall (cm) from 1924 to 2000, with corresponding trend based on linear regression of all Jul-Aug regional average totals. The vertical bars overlain on the time series indicate the standard error of the Jul-Aug regional mean.

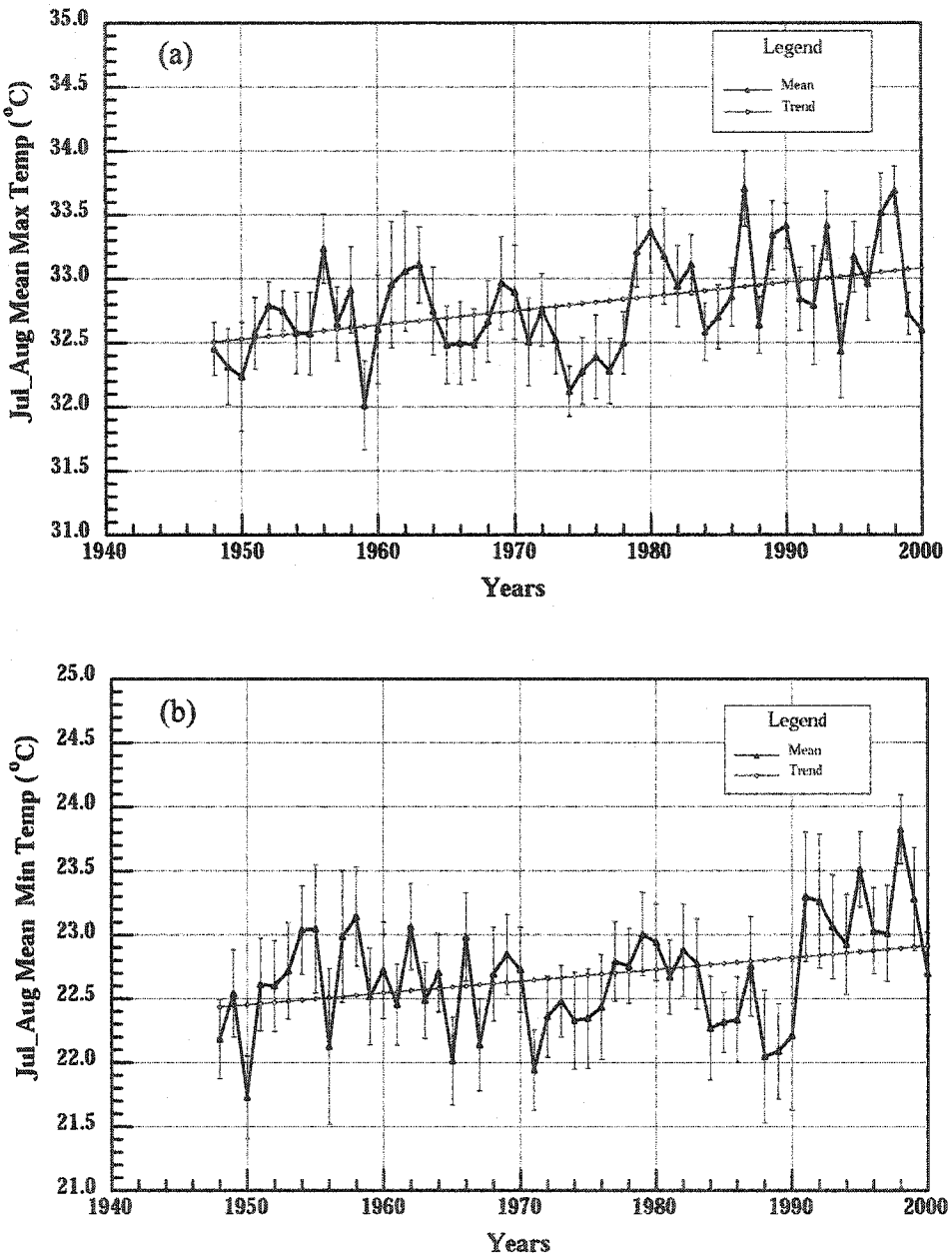

Figure 3.26. Same as in Figure 3.25, except for daily (a) maximum and (b) minimum shelter level temperature (°C).

This inconsistency of the model minimum temperature results and the corresponding observed trend could result from a number of factors, including model error, or inadequate observational sampling of those areas with the greatest cooling in the model that are in the heart of the poorly-sampled Kissimmee River valley. Possible sources of model error include the relatively coarse vertical spacing in the lower levels of the domain, and the parameterization of stable boundary layer processes. Both of these factors could result in inadequate representation of shallow nocturnal inversions. Furthermore, the sub-grid scale horizontal variability of minimum temperature is often greater than that for the daytime maximum. Maximum temperatures can be more homogenized in the horizontal by daytime boundary layer mixing processes. Moreover, the model does not explicitly predict shelter-level temperatures. They are diagnosed using similarity theory (Monin and Obukhov 1954). Numerous factors in the similarity theory framework could introduce error in the diagnosed values that may not be consistent (e.g., linear) for stable versus unstable (i.e., daytime maximum and nighttime minimum) conditions. Subtle differences between the elevation of the observing platform and the model grid cell effective elevation may also result in diagnosis of a temperature value that is not at the exact elevation of the observation. This error can be large when steep, surface-based thermal inversions are present, such as the time when the daily minimum temperature is observed. It must also be recognized that the observational time series could be indicative of a regional or larger scale trend in nocturnal warming that is indeed real, and that it could be the result of factors that are independent of those addressed by this study.

Chapter 4

COOL SEASON IMPACTS: AGRICULTURALLY DAMAGING FREEZES

4.1 Background: The Freeze Events

Simulations of the freezes that occurred on the mornings of December 26, 1983, December 25, 1989, and January 19, 1999 are presented in this chapter. The meteorological conditions associated with these events are typical of those that lead to agriculturally damaging freezes in south Florida. Figures 4.1-4.3 illustrate the sea-level pressure (SLP) and 850 hPa temperature patterns for each event. In all three events, significant surface high pressure, of Arctic origin, had migrated southward and eastward over the continental United States during the previous few days. On the morning that freezes occurred in south Florida (defined here as that portion of the Peninsula south of Lake Okeechobee), temperatures at 850 hPa had fallen to near or below 5°C, and the SLP gradient had become weak. These synoptic conditions combined to produce clear skies and calm winds. With a very dry air mass in place, the loss of infrared radiation from the land surface during the nighttime hours was optimized. The strong loss of infrared radiation allowed for the development of a steep, surface-based thermal inversion over south Florida, with a shallow layer of below freezing temperatures near ground level.

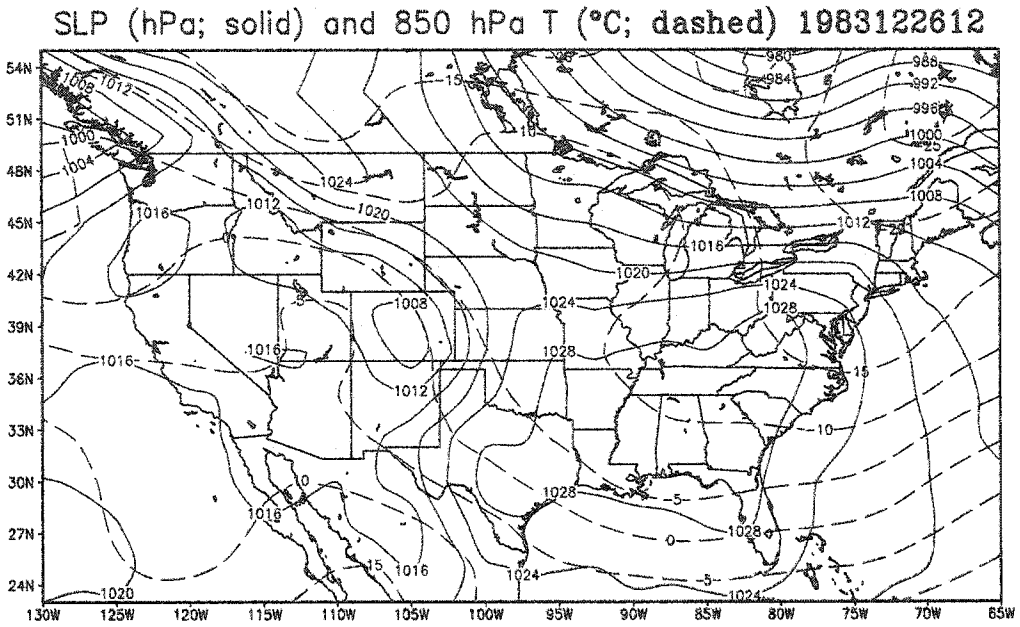

Figure 4.1. Sea-level pressure (hPa; solid contours) and 850 hPa temperature (°C; dashed contours) analyses over the conterminous U.S. valid 1200 UTC 26 December 1983. Data supplied by NCEP/NCAR Reanalysis.

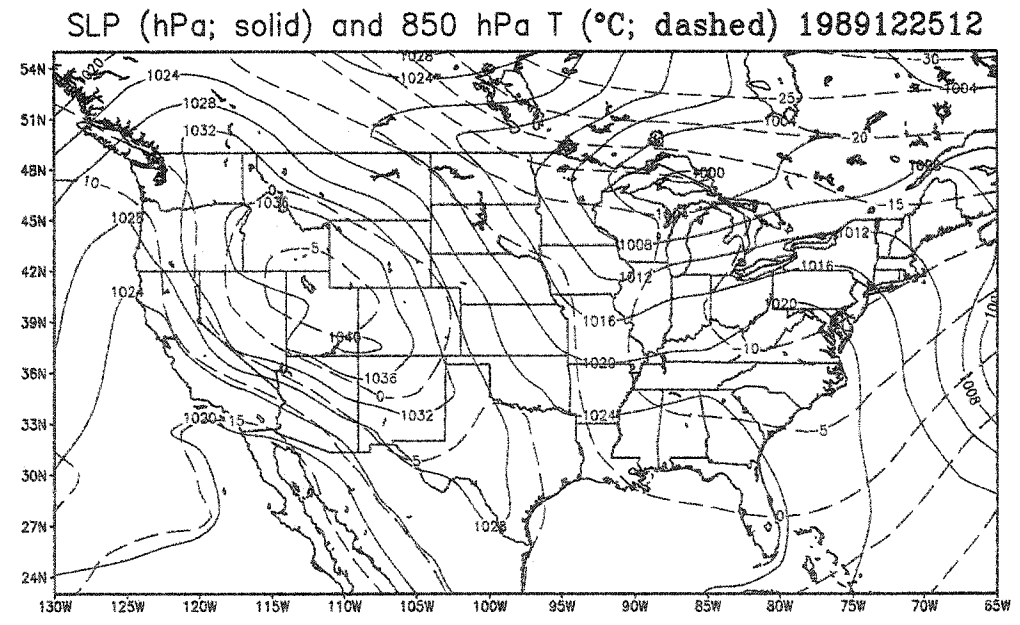

Figure 4.2. Same as in Figure 4.1, except 1200 UTC 25 December 1989.

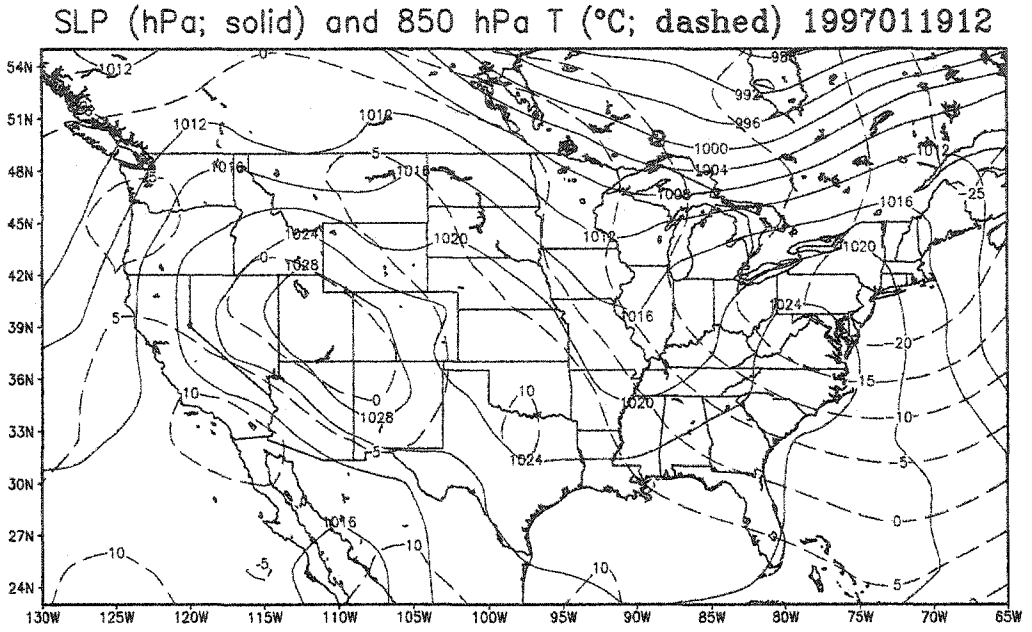

Figure 4.3. Same as in Figure 4.1, except for 1200 UTC 19 January 1997.

These types of freeze events are referred to by the Florida meteorological and agricultural communities as "radiation freezes", in contrast to "advective freezes", which are associated with the intrusion of a large-scale Arctic air mass and widespread freezing temperatures over a deep vertical layer of the lower troposphere (Rogers and Rohli 1991). This latter type of event is very rare as far south as the agricultural areas of south Florida. When freezing conditions do occur in those areas, they are usually of the "radiation" variety, and minimum temperatures rarely fall much below the freezing mark for any significant duration of time (Waylen 1988; Waylen and LeBoutillier 1989). Often, advective freezes occur over more northern areas of the peninsula on nights preceding a radiation freeze over the agricultural areas of south Florida. In many cases, these advective freezes occur on the first or second night following the passage of the cold

front associated with the leading edge of the associated Arctic air mass, when the gradient of SLP is still significant enough to sustain appreciable low-level winds throughout the night. Radiation freeze conditions may occur over areas farther south on subsequent nights, when the axis of the high pressure is near and the SLP gradient decreases.

During the 1983 and 1989 events, advective freezes did occur to the north of the agricultural areas of south Florida on the preceding night. However, this was not the case for the 1997 event. As a result, the development of freeze conditions over south Florida on the morning of January 19 was not well forecast by the local agricultural and meteorological communities. The poor forecast resulted in a lack of steps to implement freeze and frost protection measures, and thus the socioeconomic costs of the event were quite severe. Losses in the fresh vegetable and sugarcane sectors alone, with the near total loss of crops in the area of dense cultivation centered immediately south of Lake Okeechobee, were near U.S.$300M (ERS USDA 1997). In addition, nearly 100,000 migrant farm workers became displaced or unemployed (UCD 1997).

Because events similar to the cases presented here are driven by radiative cooling of the surface under atmospheric conditions that are otherwise only marginally supportive of below freezing temperatures near ground level, the nighttime minimum temperature at any particular location can be quite sensitive to local properties of the land-surface that modulate the exchange of energy with the overlying atmosphere. These properties include small topographic variations, the amount and type of vegetation, and soil water content. In the case of south Florida, these properties are strongly linked to the spatial distribution of wetlands. These events impacted areas of south Florida where these

properties had been changed markedly during the 20th Century by the conversion of wetlands to agricultural production. Therefore, these cases provide an opportunity to address the question of whether there is any possible feedback between the occurrence of recent agriculturally damaging freeze events in south Florida and the conversion of the natural landscape to agriculture itself. The natural and current land-cover datasets were implemented in RAMS to provide two simulations of the 48 h period ending at 1200 UTC on the morning of the event. The simulated minimum temperatures are presented in the next section, along with an analysis of the duration of freezing temperatures. The 1997 event was chosen for further analysis because of the surprise nature and severity of the damage it inflicted on agriculture. Time series of the surface energy budget from a location where dense agricultural production replaced wetlands are evaluated. In addition, sensitivity tests were performed using the 1997 event as the control case.

4.2 Minimum Temperatures

Figures 4.4-4.6 illustrate the observed minimum temperatures for available stations from the National Weather Service Cooperative Observer Network. The model-simulated minimum temperature at 2 m above ground level for the three events is shown in Figures 4.7-4.9. The current land-cover cases are consistent with the observational data, in that the model results indicates subfreezing temperatures in the locations where they were observed.

Comparison of the bottom panels of Figures 4.7-4.9 with Figure 1.1 reveals a strong spatial correlation between those areas that were converted from wetlands to agriculture during the 20th century, and those areas that experienced colder minimum

temperatures in the current land-cover case. These areas are located principally to the south and west of Lake Okeechobee and along the formerly inundated floodplain of the Kissimmee River valley. In the current land cover cases, minimum temperatures in those areas were colder by more than 2 °C at key locations of dense winter vegetable and sugarcane cultivation. While this may not seem like a large difference, it is worth noting that it constitutes the difference between a devastating agricultural freeze and light freeze conditions. In some cases where agriculture has replaced natural wetlands (e.g., just south of Lake Okeechobee), minimum temperatures remained above freezing altogether when the land cover was specified as natural wetlands.

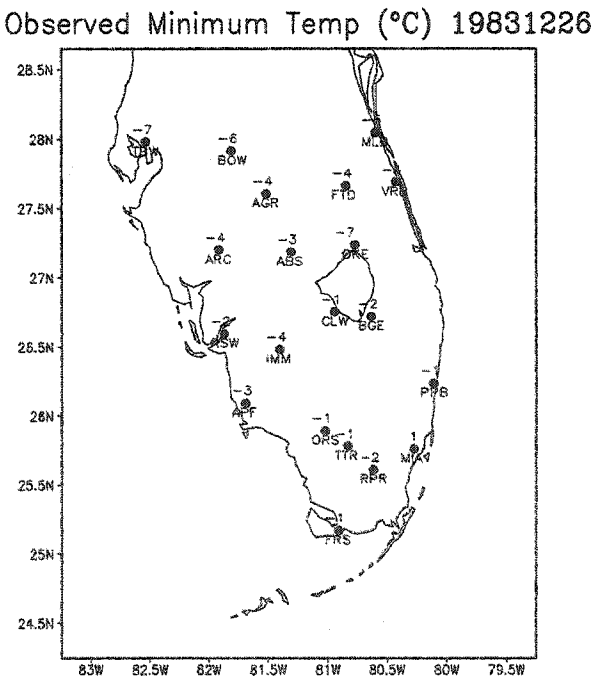

Figure 4.4. Observed minimum temperatures (rounded to the nearest whole °C) at Cooperative Observer Network sites on the morning of 26 December 1983.

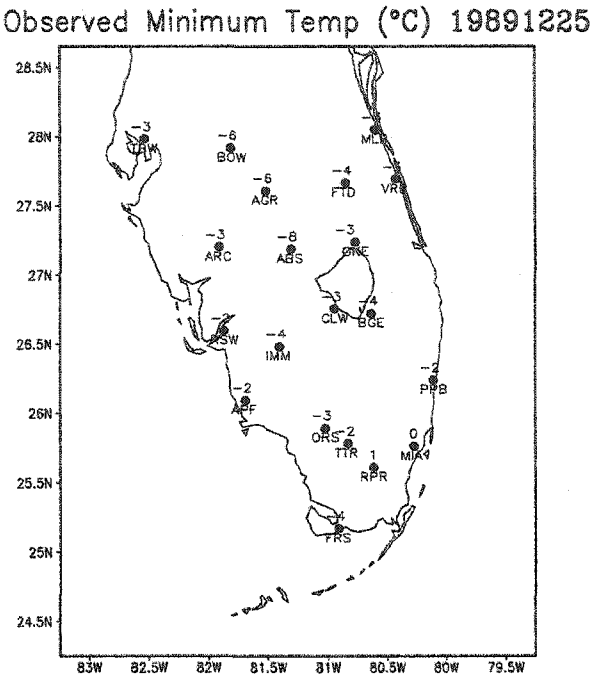

Figure 4.5. Same as in Figure 4.4, except for 25 December 1989.

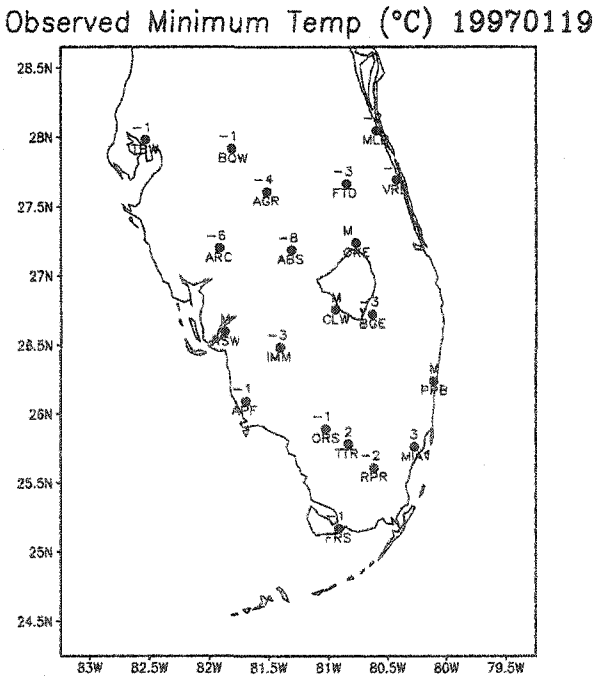

Figure 4.6. Same as in Figure 4.4, except for 19 January 1997.

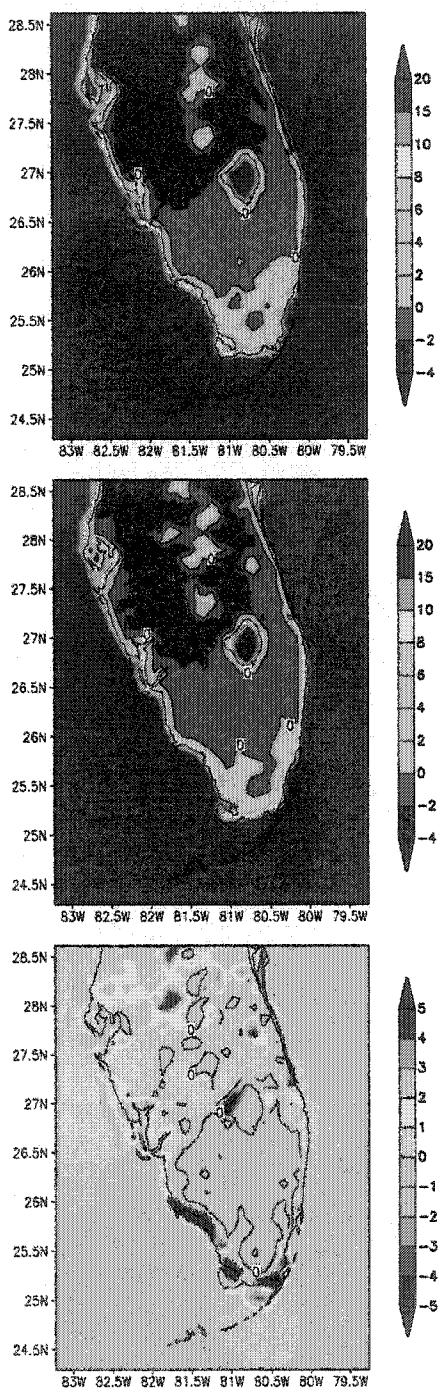

Figure 4.7. Minimum temperature (°C) at 2 m above ground level simulated by RAMS for 26 December 1983 with the natural land cover (top), the near-current land-use (middle), and the difference between the two (bottom; difference defined as the near-current minus natural scenario).

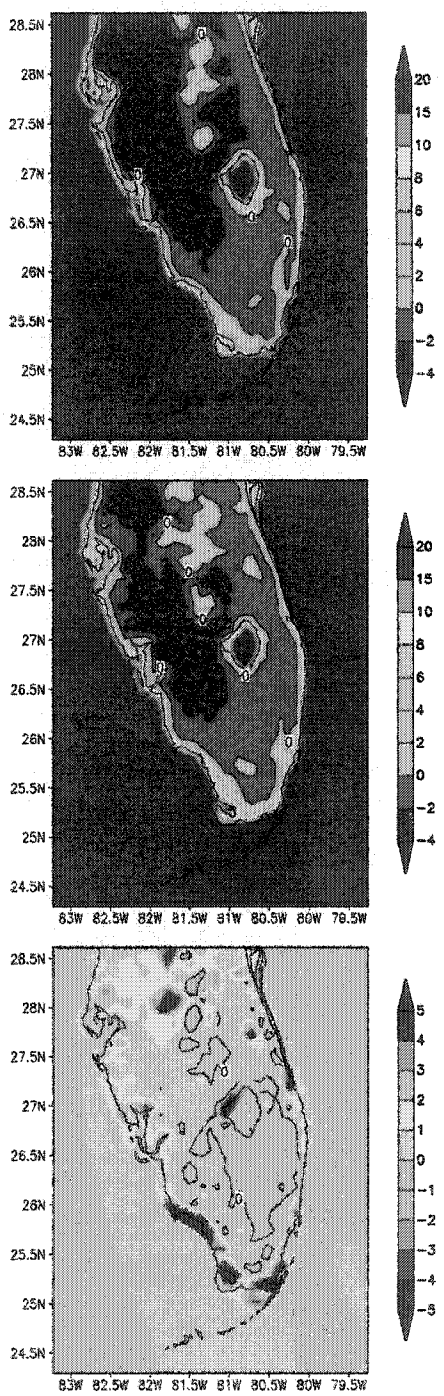

Figure 4.8. Same as in Figure 4.7, except for 25 December 1989.

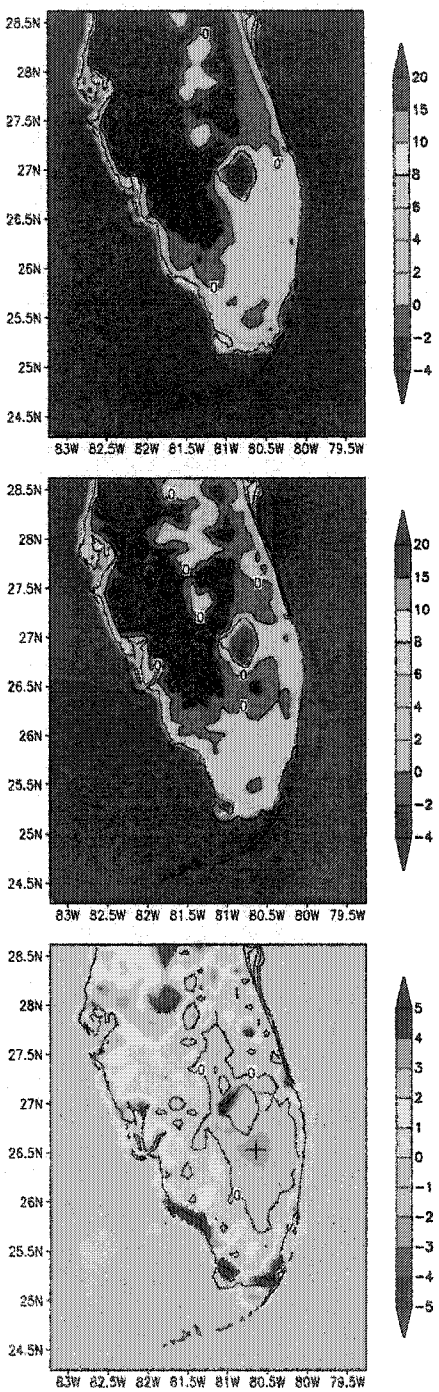

Figure 4.9. Same as in Figure 4.7, except for 19 January 1997.

At some locations between the Kissimmee River valley and the coasts, implementation of the current land use resulted in noticeably *warmer* minimum temperatures. Many of the warmer locations are associated with urbanization and the development of other significant infrastructure. Over immediate coastal locations, localized spots in the model domain were significantly warmer. These locations are associated with changes in the coastlines and the representation of these changes in the two land-cover datasets. The coastlines were changed by natural factors (e.g., hurricanes) and anthropogenic activities, including the removal of saltwater marshes. Because of these reasons, some locations that were classified as saltwater marshes in the natural land-cover dataset were reclassified as ocean in the current land cover. Thus, at the affected model grid points, the temperature of underlying water surface was initialized with the SST data, whereas the initial value was set equal to the initial air temperature at the first model level above ground in the natural land-cover case. This difference resulted in significantly warmer shelter-level temperatures in the current land-cover case. This issue is not a significant factor in this analysis, because this work is focused on those areas of wetlands in the interior that were converted to agricultural land during the 20th Century.

4.3 Freeze Duration

Depending upon the particular crop, and the stage of growth and development, the amount of time spent below a critical temperature threshold can be just as important as the magnitude of the minimum temperature itself in determining the amount of damage realized by exposure to sub-freezing temperatures. This is because the plants, buds,

fruits, and vegetables themselves have finite thermal inertias. Thus, an extended duration of exposure to subfreezing air is required for damage to occur. For example, mature, full-size oranges can escape damage even when temperatures fall to –4°C for one hour (Wolford 1955). These factors warrant a consideration of the impact of the specification of land cover on the duration of time spent below 0°C in the model simulations of these events. In all three events, the most densely cultivated areas south and southwest of Lake Okeechobee and in other key agricultural areas in the Kissimmee River valley were not only colder in the current land cover, but they also experienced subfreezing conditions for a longer duration (Figures 4.10-4.12).

The combination of duration and minimum temperature difference varied among the events. For example, in the 1983 simulations, the area south of Lake Okeechobee was not significantly colder when current land cover was implemented. However, the amount of time below 0°C was longer by 5 h. In the simulations of the 1997 event, this area remained above freezing throughout the night when classified as wetlands, whereas subfreezing temperatures were simulated for more than 5 hours when classified as agricultural land. As noted above, the 1997 freeze inflicted particularly severe damage on south Florida agriculture. The land cover specification determined both the severity, and the overall occurrence of a freeze event at the locations of severe damage. Given these reasons, this particular set of simulations was chosen for further analysis.

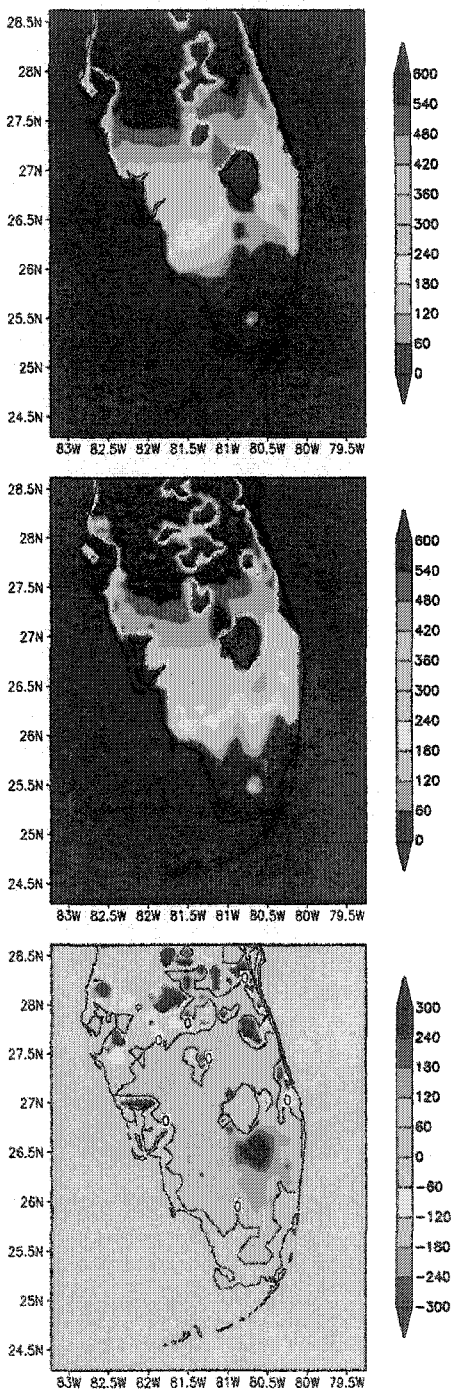

Figure 4.10. Time spent below 0°C (min) in the RAMS simulations on the morning of 26 December 1983. Panel convention same as above.

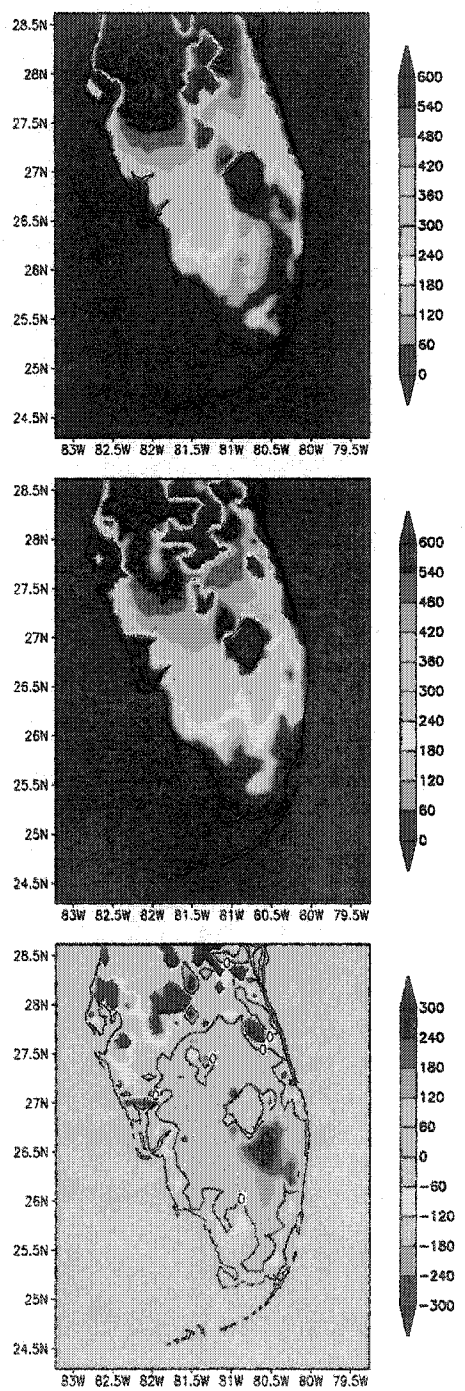

Figure 4.11. Same as in Figure 4.10, except for 25 December 1989.

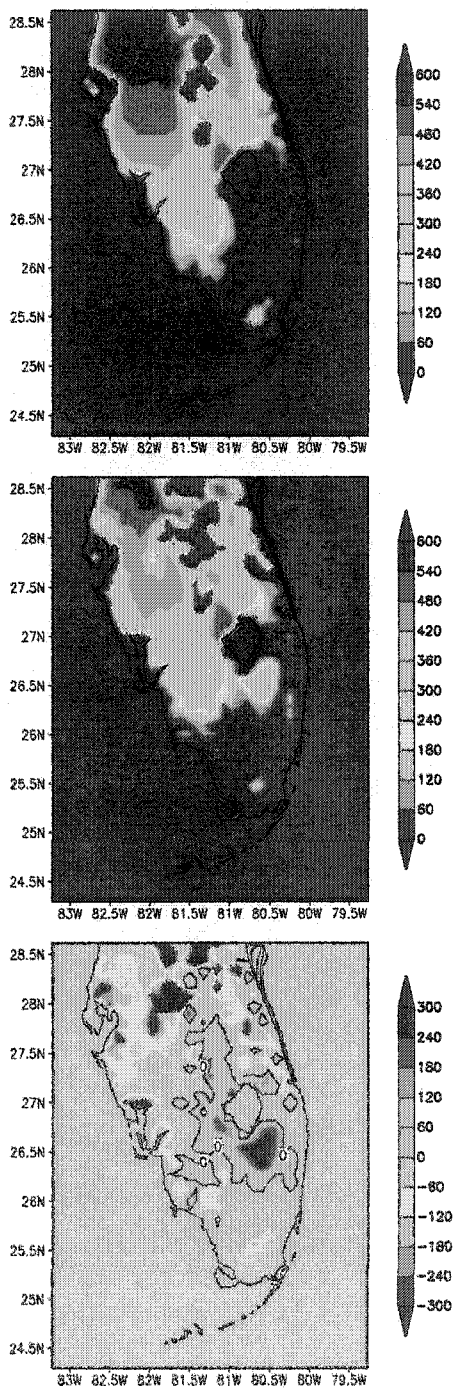

Figure 4.12. Same as in Figure 4.10, except for 19 January 1997.

4.4 The Surface Energy Budget

The impact of land-cover properties on the evolution of an event such as the south Florida freezes investigated for this work results from strong modulation by the land surface of the exchange of energy with the overlying atmosphere. Many of the areas that experienced colder temperatures for a longer duration in the simulations with current land cover were natural wetlands before they were converted to agricultural land during the 20th Century. In the model configuration, areas that were specified as wetlands were specified to have saturated soil with 10 cm of standing water beneath the vegetation canopy (see Chapter 2 for a more detailed description of this aspect of the model configuration). The presence of saturated soils and standing water on the land-surface could have a substantial impact on the exchange of energy with the overlying atmosphere.

Figure 4.13 provides model time series of the components of the surface energy budget from a grid point located just south of Lake Okeechobee. Before the completion of the Hoover Dike in the 1930s, which now prevents overland flow out of Lake Okeechobee and into the Everglades, this was an area of inundated sawgrass marsh. Today, it is one of the most densely cultivated locations of winter vegetable and sugarcane production in south Florida. At this location, the model sensible heat flux simulated with the natural cover is much less during the daytime hours than that simulated with current land cover. Conversely, the model latent heat flux in the natural case is much greater. These differences are a direct consequence of the removal of saturated soils and standing water at this location. In the natural case, more of the available energy is expended by the evaporation of water, and the sensible heat flux is

lower. The effect of the standing water is also reflected in the difference in the diurnal cycles of the effective skin temperature (the radiative temperature of the combined ground and vegetation surface; Figure 4.14). In the natural case, the standing water, beneath the sawgrass canopy, acts to dampen the diurnal cycle of the effective skin temperature, because it increases the effective heat capacity of the land surface.

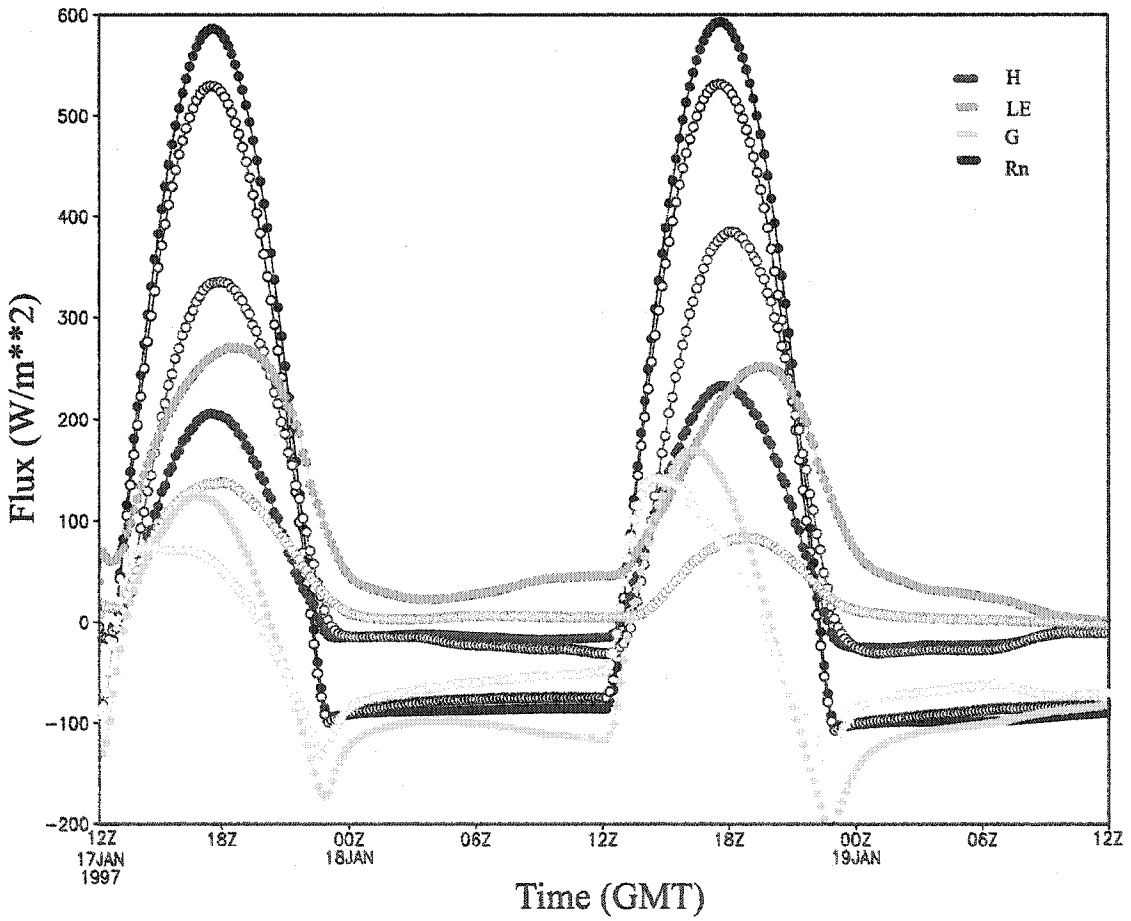

Figure 4.13. Time series of the four components of the surface energy budget (W m^{-2}; see color code provided in legend) for both RAMS simulations of the 19 January 1997 event, at a model grid point centered just south of Lake Okeechobee (location indicated by the "+" on the bottom panel of Figure 4.9). Filled (open) circles indicate data for the natural (current) land cover.

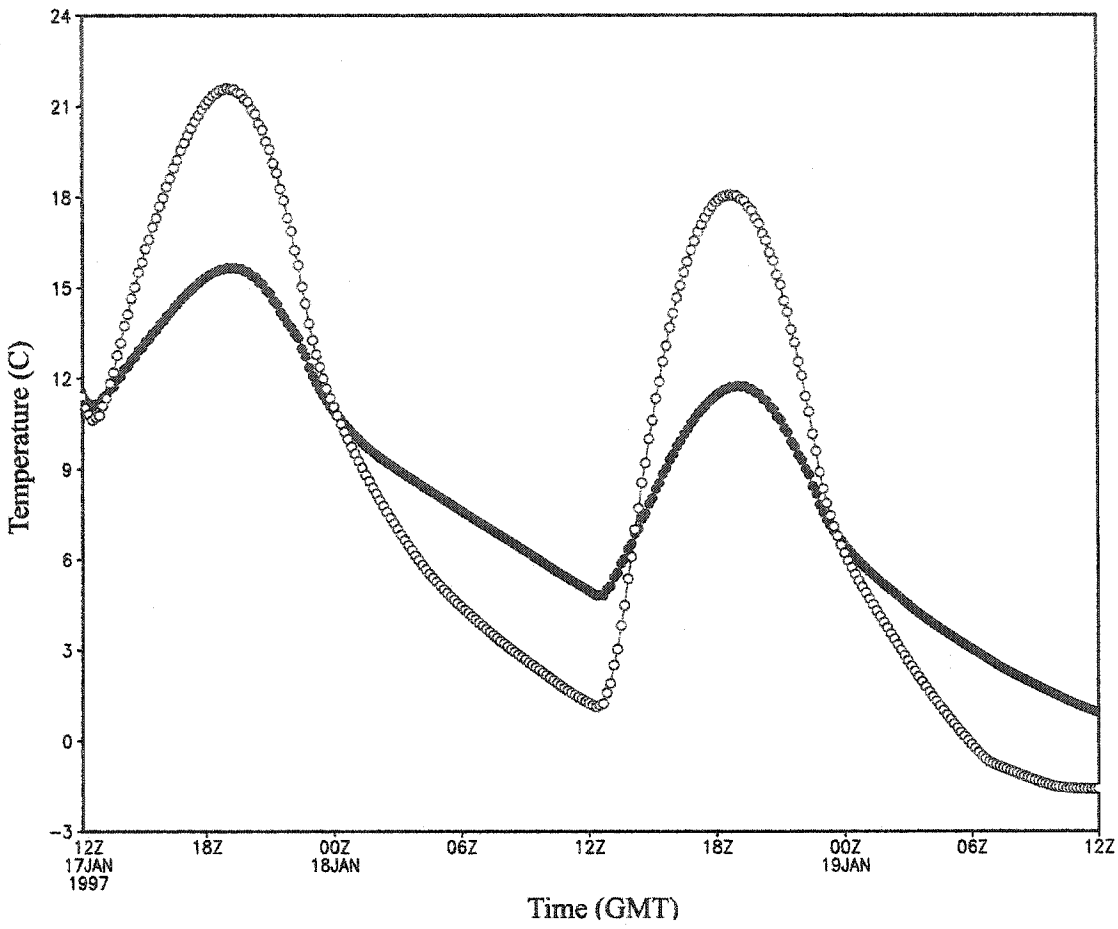

Figure 4.14. Time series of the effective skin temperature (°C). Filled (open) circles indicate data for the natural (current) land cover.

The sensible and latent heat fluxes during the night of January 19 are shown on Figure 4.15 for greater visual clarity. During the nighttime hours, the sensible heat flux in both cases is negative, indicating turbulent heat transfer from the lower atmosphere to the land surface as the land surface itself cools via radiative loss. When the current land cover is implemented, the nighttime latent heat flux drops to near zero. However, latent heat flux continues after sunset in the natural cover case, despite the fact that net radiation has become negative. Figure 4.16 illustrates that in the natural case, the ground heat flux

remains larger (in absolute magnitude) than the net radiation until approximately 0700 UTC. This supplies the energy to sustain the water vapor flux. In the current land-cover case, the available energy quickly becomes negative after sunset, as the ground heat flux becomes less (in absolute magnitude) than the net radiation. The negative available energy is reflected almost entirely in the magnitude of the (negative) sensible heat flux.

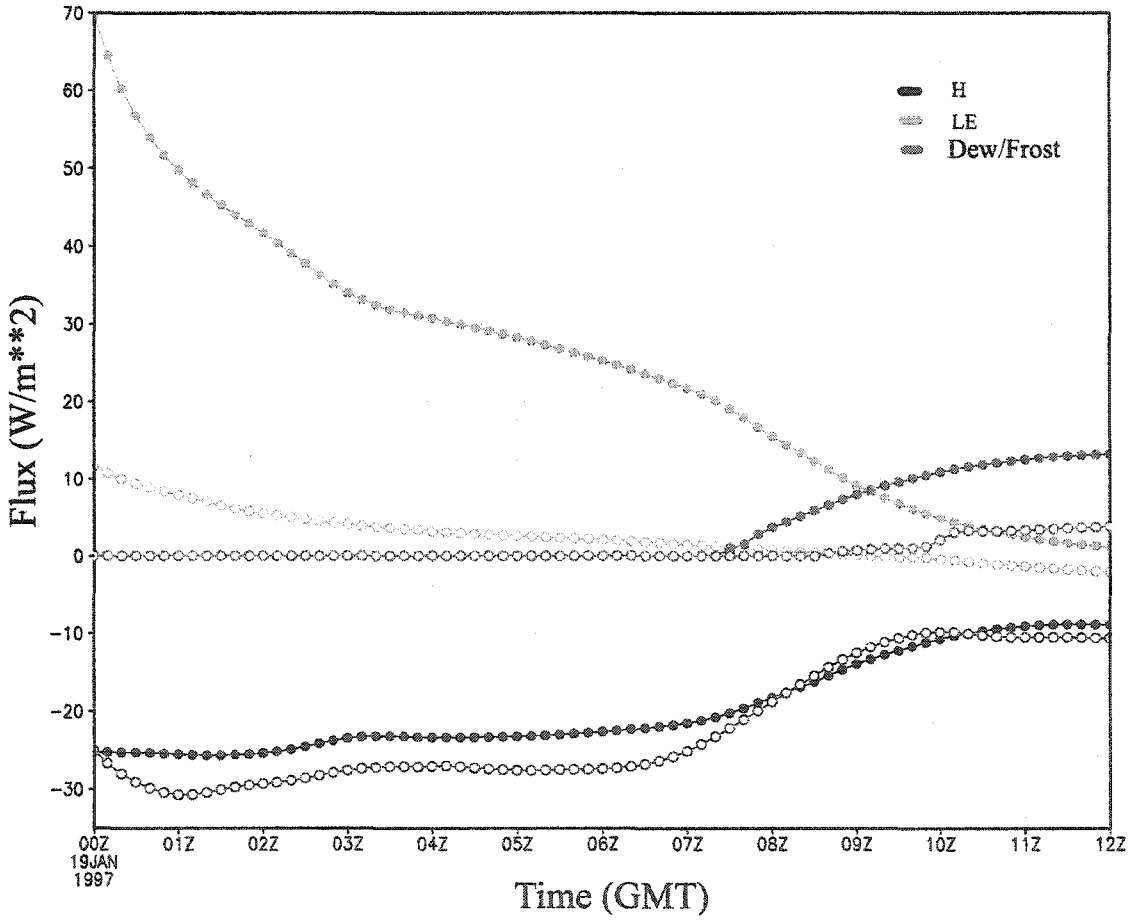

Figure 4.15. As in Figure 4.13, except for the night hours only, for H and LE, with the addition of the condensational/depositional heating due to dew or frost.

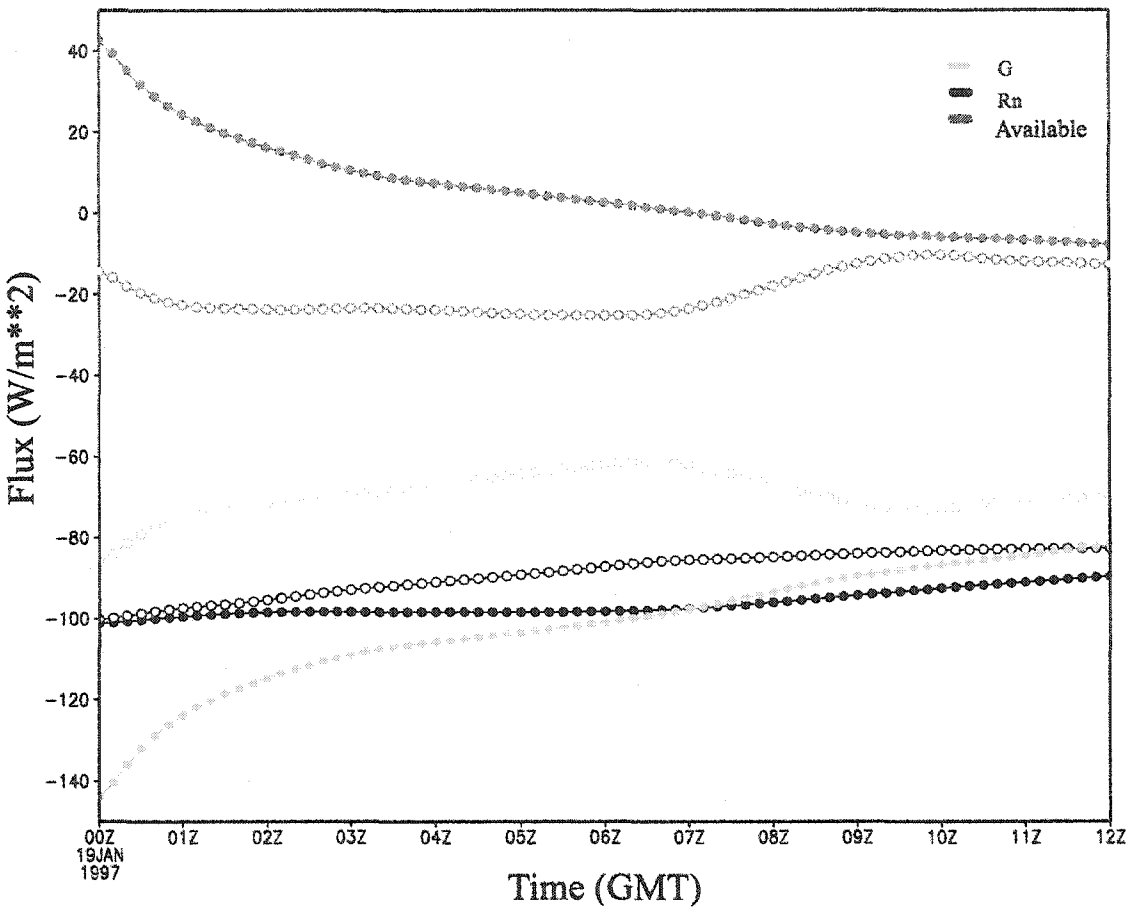

Figure 4.16. As in Figure 4.13, except for the night hours only, for G and Rn, with the addition of the available energy (Rn - G).

The larger ground heat flux in the natural case is sustained during the evening hours because a larger amount of heat is gained during the day, and this heat is released more slowly than in the current case. This results primarily because the effective heat capacity of the surface is much larger than that of the dry land in the current case. Furthermore, the thermal conductivity of liquid water is nearly six times that of dry soils with a high organic matter content (Oke 1987), which is the soil type specified at this location in the current case. Thus, during the preceding daylight hours, the wetlands

cover is much more efficient at conducting the available net radiation into the surface and storing this energy in the water layer. After sunset, the dry soil in the current case loses the smaller amount of heat that it has stored and cools relatively quickly, allowing the ground heat flux to become less in magnitude than the net radiation.

It is noted that the available energy that persists after sunset is allocated primarily towards latent heat flux, rather than more equally between additional sensible and latent fluxes. For example, at 0300 UTC, the available energy in the natural case is near 10 W m^{-2} (see Figure 4.16). Figure 4.15 shows that the natural case value of latent heat flux at this time is about 35 W m^{-2}, whereas the natural case value of sensible heat flux is close to -25 W m^{-2}. The disproportionate partitioning of the available energy in the natural case into evaporation results from the *relative* contributions of the water surface and the overlying vegetation canopy to the bulk sensible and latent heat fluxes from the combined water surface/vegetation canopy. As outlined by Strack et al. (2004) and Walko et al. (2000), the individual contributions of the ground (or water) surface and vegetation canopy to the bulk surface energy fluxes in LEAF-2 are proportional to the density of the vegetation canopy:

$$H_{eff} \sim f_{veg} * LAI * H_v + H_w \tag{4.1}$$

In Equation (4.1), H_{eff} is the total atmospheric surface-layer sensible heat flux. The contributions from the water surface and the overlying vegetation canopy are given by H_w, H_v, respectively, The fractional vegetation coverage and leaf area index are represented by f_{veg} and LAI. This formulation accounts for the fact that a dense vegetation canopy has a significantly larger surface area in contact with the adjacent air

than the underlying water surface. In this particular case, the specified vegetation fraction of the sawgrass canopy above the standing water is near 0.75, and the LAI is 4.0. Thus, the canopy component contributes significantly to the transfer of sensible heat from the combined water surface/vegetation canopy at the location of this grid cell. A relationship analogous to (4.1) can be written for the latent heat flux. In this particular case, with negative net radiation, the canopy is not transpiring, and thus the effective latent heat flux is entirely from the water surface.

The partitioning of the available energy in both the current and natural cases means that, while the latent heat flux in the natural case is much larger (the latent heat flux in the current case is almost negligible), the sensible heat flux does not differ significantly from that in the current case. Because the skin temperature, which provides the lower boundary condition for calculating the sensible heat flux, is significantly warmer in the natural case, this result may at first seem counterintuitive. However, it is important to remember that the magnitude of the bulk sensible heat flux is determined by the *vertical gradient* of the temperature between the skin and the air at a reference height in the surface layer as follows:

$$H_{eff} = \rho C_p \frac{T_{skin} - T_a}{r_a} \tag{4.2}$$

where r_a is the aerodynamic resistance (which, in this formulation includes the wind speed through its incorporation of the friction velocity), and T_a is the air temperature at a reference height above the surface. In LEAF-2, this temperature is the explicitly predicted temperature at the height of the first model vertical surface (about 20 m). All other variables are as defined in Section 3.5. Figure 4.17 illustrates the absolute value of

vertical temperature gradient as applied in Equation (4.2). The gradient in the current case is as much as 2-3 times the corresponding natural case value, yet the magnitude of the sensible heat flux in the current case is not 2-3 times that in the natural case. This is because the aerodynamic resistance (Figure 4.18) is also much larger in the current case than in the natural case. The aerodynamic resistance reflects the fact that, as the profile becomes more stable (i.e., the vertical temperature gradient becomes larger), the layer becomes more resistant to turbulent mixing. These results are entirely consistent with the formulation of the surface resistances (Louis 1979) employed in LEAF-2.

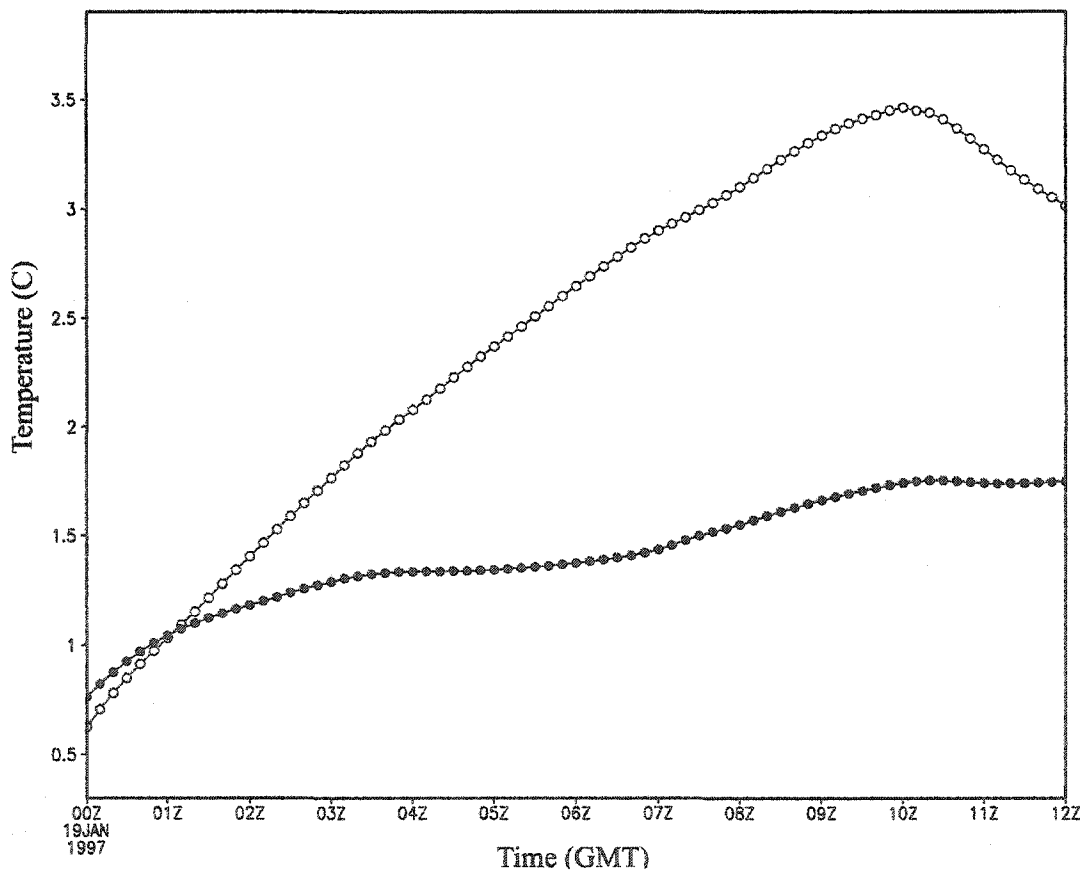

Figure 4.17. Vertical temperature gradient (Ta - Tskin; °C). Filled (open) circles indicate data for natural (current) land cover.

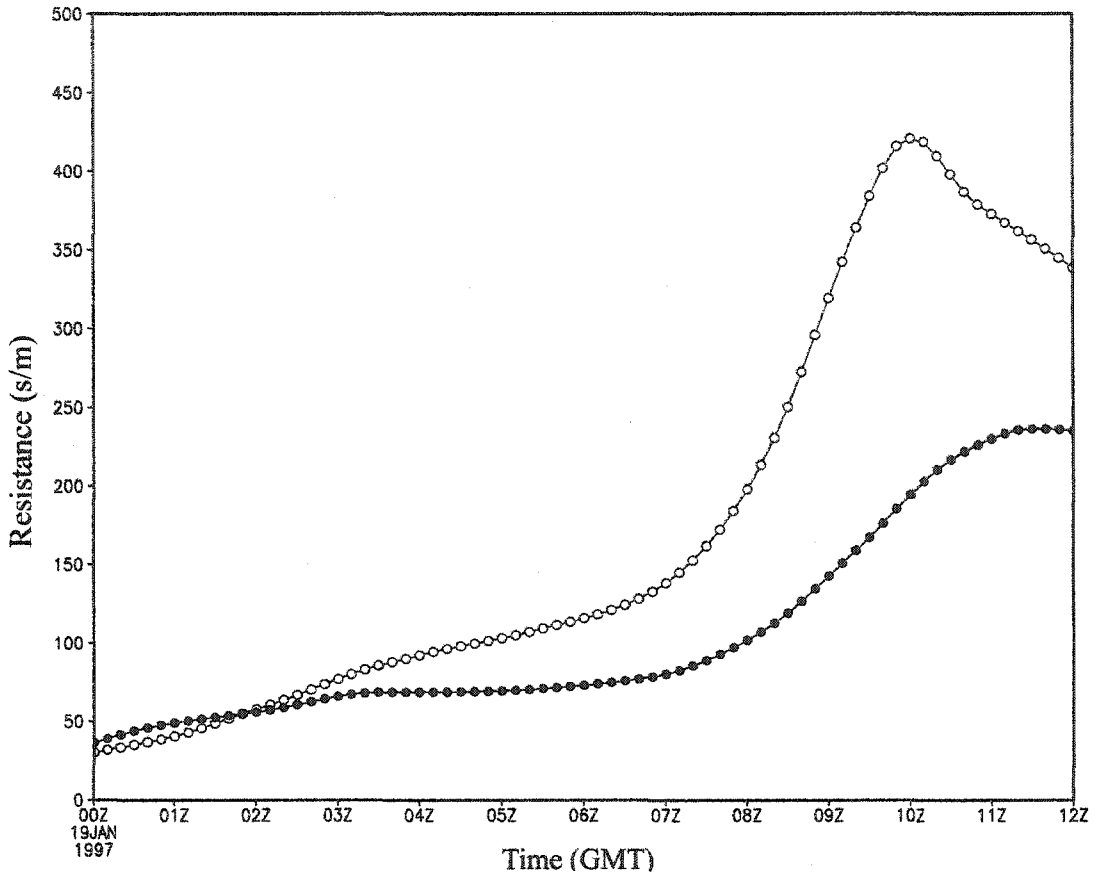

Figure 4.18. Aerodynamic resistance (s m^{-1}) for the turbulent heat fluxes. Filled (open) circles indicate data for natural (current) land cover.

The bulk transfer of water vapor can also be expressed as a relationship analogous to (4.2), except the vertical gradient in question is that between the water vapor content of the canopy air and the water vapor content at the reference height. It is assumed in LEAF-2 that the aerodynamic resistance to water vapor flux is equal to that for heat transfer. Figure 4.19 illustrates this gradient for both land-cover cases. During the early evening, the gradient in the natural case is as much as 6-8 times larger than that in the current case. Unlike the case of sensible heat flux, the difference in aerodynamic resistance cannot adequately compensate, and thus the water vapor flux in the natural case is much larger than that in the current case.

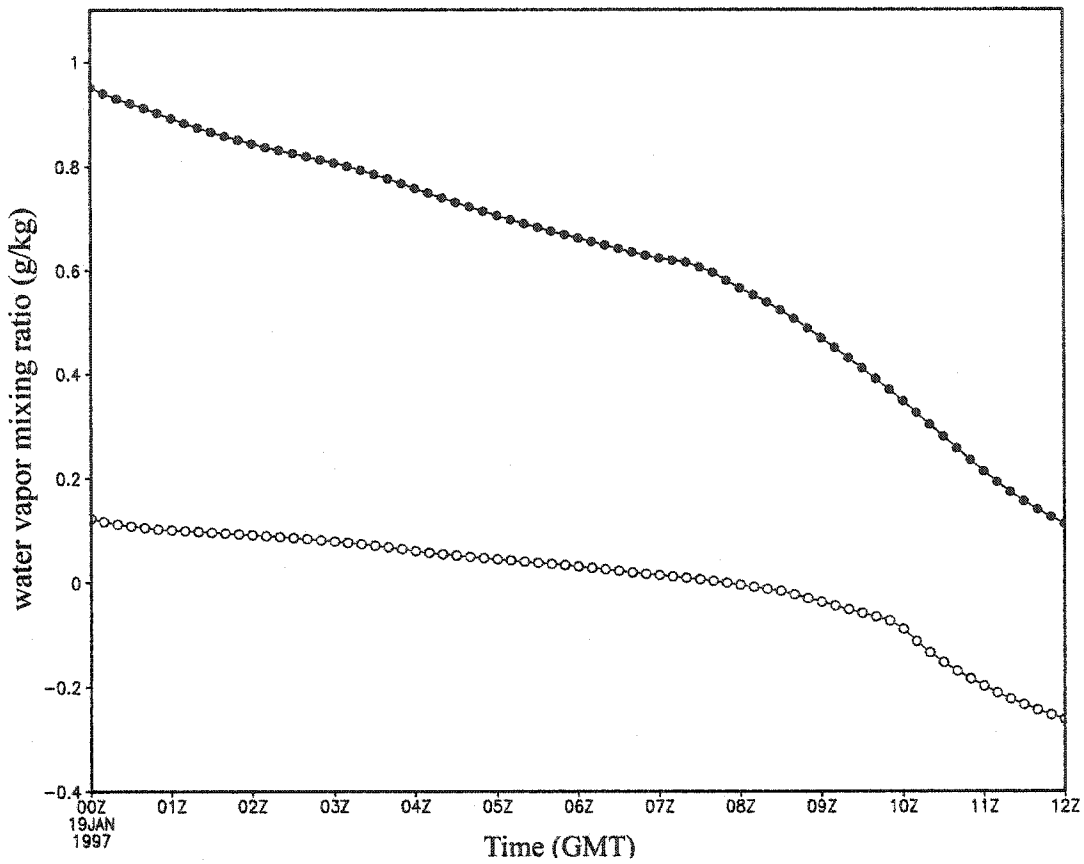

Figure 4.19. Vertical water vapor gradient (absolute value of canopy value minus value at height of Ta in Figure 4.17; g kg^{-1}). Filled (open) circles indicate data for natural (current) land cover.

It is also of interest to note that, in the natural case, the formation of dew does contribute an appreciable amount of condensational heating during the early morning hours. As Figure 4.15 illustrates, condensational heating from dewfall begins around 0700 UTC, and increases to near 11 W m^2. This condensational heating is reflected as an increase in the sensible heat flux, and a decrease in the latent heat flux. Note that dewfall begins while the bulk latent heat flux remains positive. This occurs because the vegetation canopy has cooled below the dewpoint temperature, but the water surface beneath continues to evaporate.

In the current land-cover case, the skin temperature (Fig. 4.14) falls below freezing well before 1000 UTC, thus the heating that begins around that time is due to the latent heat of deposition (frost formation). The overall contribution of the depositional heating is relatively insignificant to the nocturnal evolution of the surface energy budget. However, it appears that the freezing of the water content in the soil itself has an impact on the evolution of the surface energy budget. The skin temperature in this case reaches 0°C around 0600 UTC. The effect of this can be seen in the ground heat flux (Figure 4.16), which begins to increase (in absolute magnitude) around the same time, after it had been decreasing since sunset. The thermal conductivity of soil increases with moisture content. Because ice has a thermal conductivity about 4 times that of water (Oke 1987), the freezing of any moisture content will further increase the thermal conductivity. The reversal of the tendency of ground heat flux seen in Figure 4.16 and its coincidence with the point in time when the skin temperature reaches the freezing point of liquid water reflects this effect. This increase (in magnitude) of the ground heat flux is reflected in a change in the available energy. After having hovered near –20 W m^{-2} for several hours, the available energy begins to rise (see Figure 4.16). Figure 4.15 shows an accompanying rise in the sensible heat flux, the negative value of which in this case is nearly equal to the available energy for most of the night, because latent heat flux is negligible. In essence, the effect of the freezing of the water content of the near-surface soil layer does impact in a non-trivial manner the evolution of the nocturnal energy budget.

It is reasonable to expect that the differences in the diurnal cycles of the surface energy budget should be reflected in the diurnal cycles of the near-surface atmospheric

temperature and moisture content. As Figure 4.20a illustrates, the diurnal cycle of the 2 m temperature in the natural case is indeed dampened relative to the current case. The time series of 2 m water vapor mixing ratio (Figure 4.20b) indicates that, in both land-cover cases, the water vapor content of the near-surface airmass generally decreased throughout the simulation. This general decrease results because of synoptic-scale dry air advection, which followed the cold front that passed two days prior to the freeze event. However, the airmass remained persistently moister in the natural land-cover case because of the persistently larger water vapor flux from the underlying wetlands.

The results presented above indicate that, from a broader perspective, the impact of standing water on the surface is to change the effective heat capacity of the surface. It is this change in heat capacity that impacts the diurnal cycles of the surface energy budget and thus the diurnal cycles of the near-surface atmospheric temperature and moisture. The particular question of interest here, however, is the impact on the magnitude of the nocturnal cooling of the near-surface airmass, and the relative importance of the factors that allowed the nocturnal cooling in the current case to exceed that in the natural case by 2°C. One question of interest includes the role of the specified depth of the wetlands, and its impact on the nocturnal cooling. The specified depth of the water should directly impact the effective heat capacity of the land surface, and thus the rate of nocturnal cooling of the skin temperature and the 2 m temperature. Another important question involves the relative importance of the impact of atmospheric water vapor on the radiation budget, and its relationship to the water depth. These issues are explored in more detail in the next section.

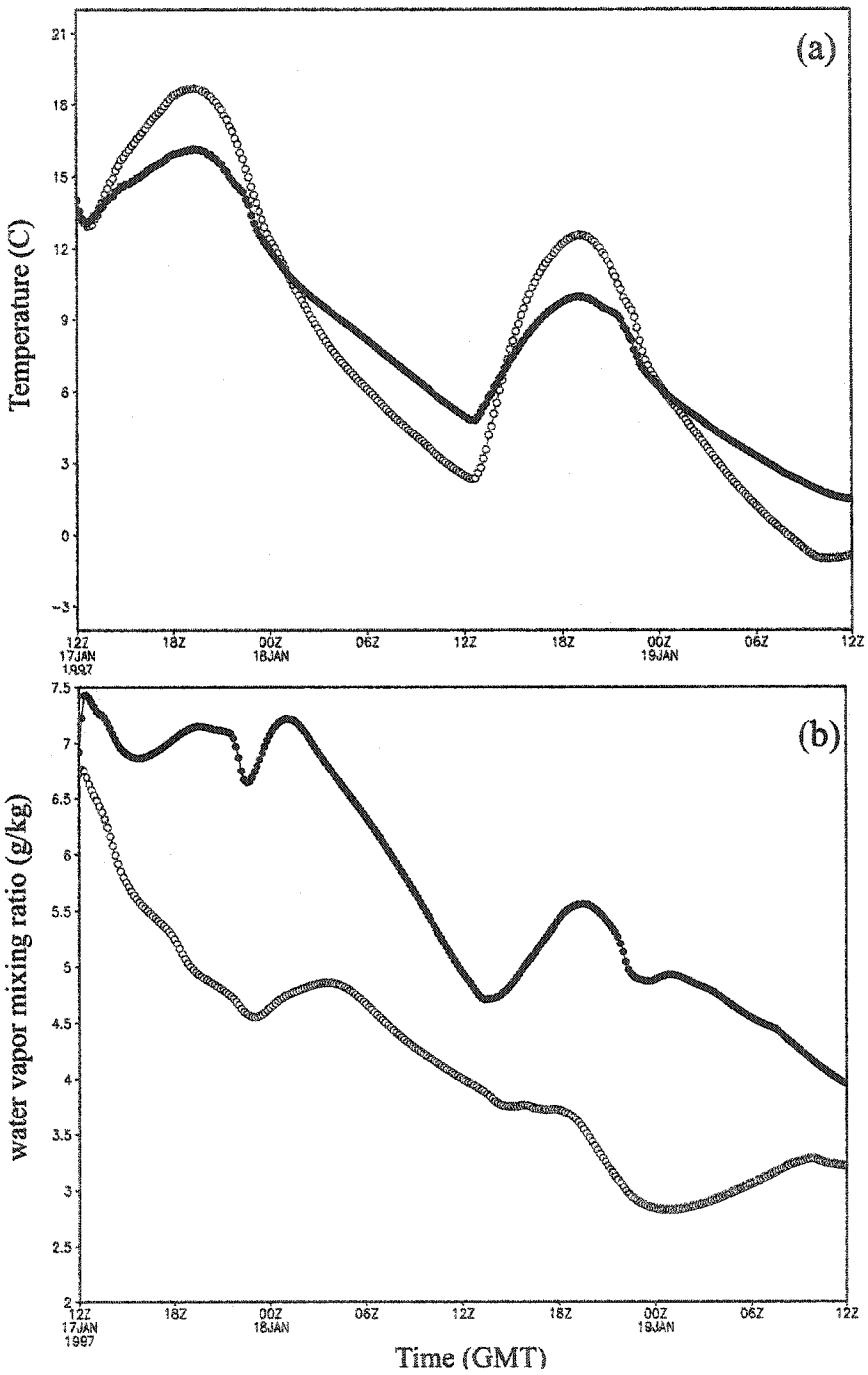

Figure 4.20. Time series of the (a) temperature at 2 m above ground level (°C) and (b) the 2 m water vapor mixing ratio (g kg^{-1}) for the same grid point as for the data shown in Figures 4.13-4.16. Filled (open) circles indicate data for natural (current) land cover.

4.5 Sensitivity to Water Depth

According to Kushlan (1990), most of the wetland areas just south of Lake Okeechobee and in the Kissimmee Valley are inundated through January. As discussed in Chapter 2, 10 cm was chosen to represent an effective depth over the area of a RAMS model grid cell. In nature, however, there is considerable variability in the water depth over a 10 km × 10 km area. The model-specified depth of the water could have a substantial impact on the effective heat capacity of the land surface, and thus the simulation of the surface fluxes and the minimum temperatures. To address this issue, sensitivity tests were performed. Specifically, the simulations of the 19 January 1997 event were repeated, with half (5 cm) the default depth and again with double (20 cm) the default depth.

Figure 4.21 illustrates the impact of halving the water depth. Despite the shallower specified depth in the natural land-cover case, the key locations of winter vegetable and sugarcane cultivation still experienced colder minimum temperatures for a longer duration when current land cover was specified. The differences in the control case were somewhat greater (see bottom panels of Figures 4.9 and 4.12). Figure 4.22 shows that when the water depth in the natural land-cover case is doubled, the effect of land-cover change is magnified, because the differences in minimum temperature and freeze duration are greater than the differences within the control simulations.

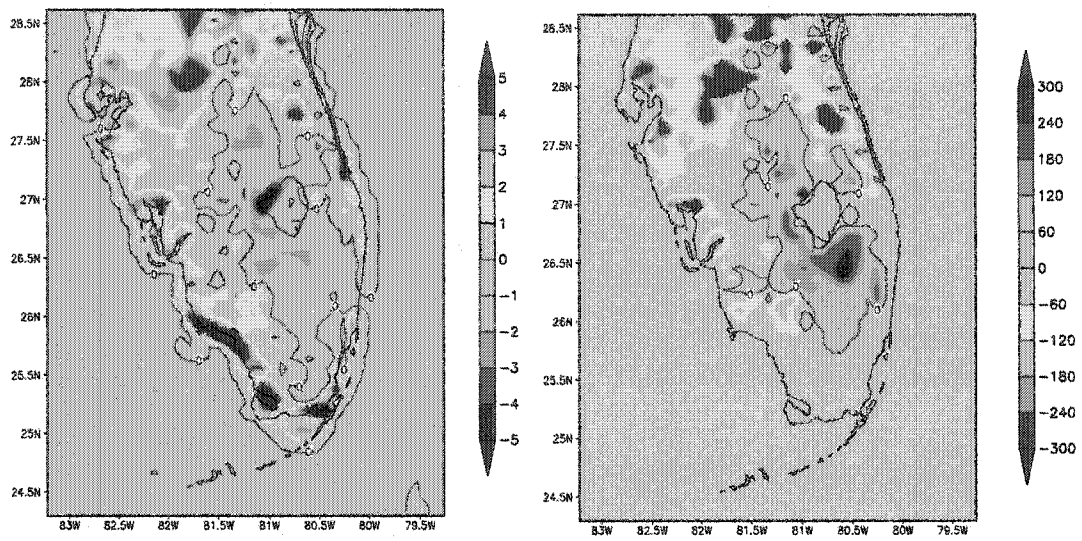

Figure 4.21. Difference fields (current minus natural land cover) for (a) temperature (°C) and (right) time below freezing (min.) when the depth of water at wetlands was specified at 5 cm (half the control case depth) in the simulations of the 19 January 1997 event.

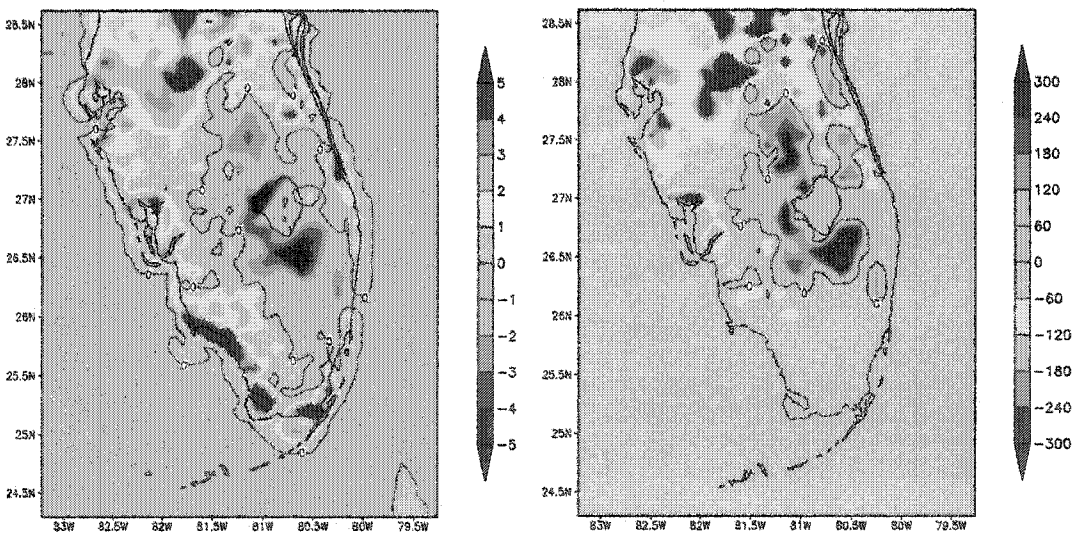

Figure 4.22. Same as in Figure 4.21, except the depth of wetlands was specified as 20 cm (double the control case depth).

In the preceding section, it was shown that the effective skin temperature of the land surface remained warmer throughout the night in the natural case. The net longwave radiation at the surface was larger than that in the current case. The ground heat flux in the natural case remained significantly larger in magnitude, resulting in the available energy remaining positive. In contrast, the available energy in the current case became negative shortly after sunset. In terms of the differences in the nocturnal sensible and latent heat fluxes, the major effect was to sustain a physical evaporation in the natural case that was not present in the current case. Although the magnitude of the sensible heat flux is greater in the current land-cover case, the difference in sensible heat flux was not as large as that for the latent heat flux. The reasons for this were shown to be related to the nature of the partitioning of the available energy by the land surface in each of the cases, and the relative differences in the near-surface gradients of temperature and moisture, as well as differences in the aerodynamic resistances.

It was also shown above that the standing water provided a source of lower atmospheric water vapor by sustaining a water vapor flux from the surface that was not present in the current land-cover case. Throughout the simulation period, the difference in the latent heat flux was significant. When nocturnal cooling commenced (near 0000 UTC on January 19), the near-surface moisture content was significantly higher in the natural case. During the night, the water vapor flux continued to support higher near-surface water vapor content in the natural case. It is possible that this water vapor content could impact the nocturnal cooling, by altering the radiative cooling of the air near ground level. This effect is a somewhat different mechanism than the control exerted by the standing water on the cooling of the land surface itself. Of course, these

effects cannot really be considered as mutually exclusive in nature. The higher near-surface water vapor content, the effective heat capacity of the land surface, and the surface energy budget are all fundamentally related to the impact of standing water on the surface, and hence the depth of that water. The question of interest here is how that depth impacts the relative importance of the factors involved.

Figure 4.23 illustrates the diurnal cycle of the effective skin temperature for the natural case, with the default (10 cm) specified depth, and with the 5 cm and 20 cm depths. The diurnal cycle with the current land cover is included for reference. During the daylight hours, the natural case temperatures are much closer to each other than any of them is to the current case temperature. At night, however, an appreciable spread develops among the values corresponding to the three depths. Some portion of these differences may reflect the assumption specified in LEAF-2 that the standing water has a uniform temperature throughout its depth. Given the overall shallow depths in question, and the high thermal conductivity of water, this assumption is probably a good one. At night, cooling at the top of the layer could generate negatively buoyant convection, which should readily overturn the shallow confined fluid and prevent the development of steep vertical temperature gradients. Of course, the timescale of convective overturning increases with the depth of the fluid, so the assumption would be most susceptible with the 20 cm depth. Nevertheless, the results shown in Figure 4.23 confirm that as the specified depth of the water increases, the differences in skin temperature among the three depths are larger at night than during the day.

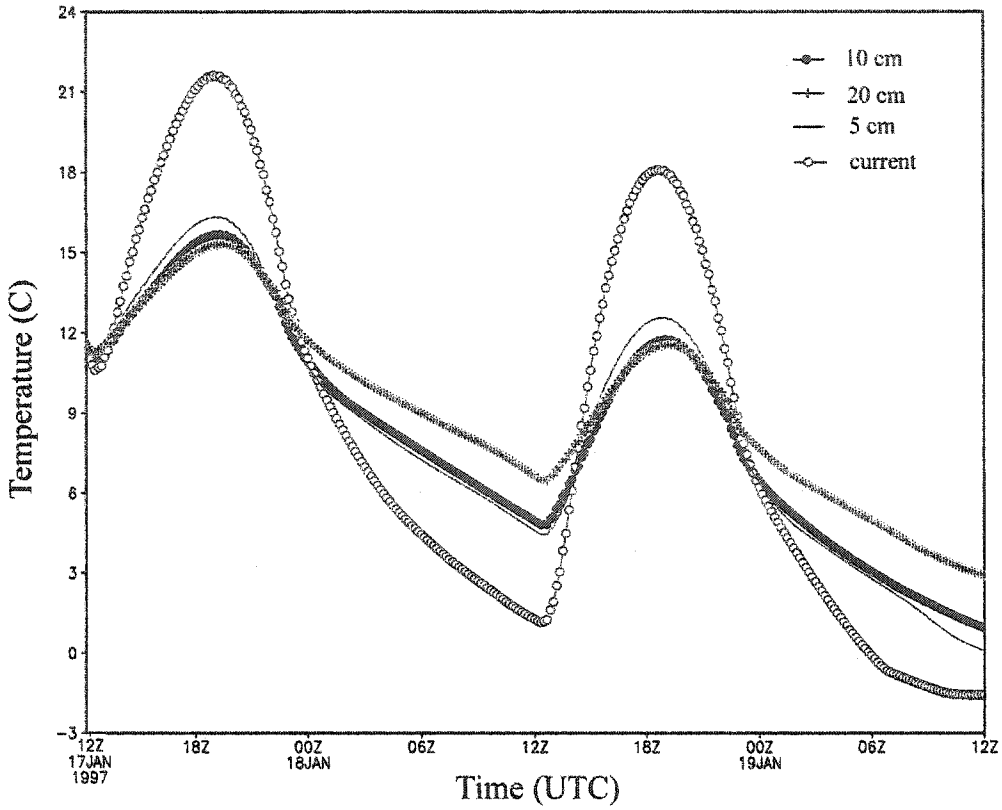

Figure 4.23. Diurnal cycle of the effective skin temperature (°C) for the natural case with default depth (filled circles), the natural case with double (20 cm) depth ("+"), the natural case with half (5 cm) depth (no marker), and the current land-cover case (open circle).

Figure 4.24. illustrates the diurnal cycle of 2 m air temperature and mixing ratio, for the three depths in question and the current land-cover case. In all three natural case depths, the airmass remains moister throughout the simulation period. The daytime natural case values of mixing ratio are relatively close, in comparison to the current land-cover case. During the night, a relatively even spread develops among the four values. Similar behavior is noted in the 2 m temperature time series. Thus, the times series indicate that the magnitude of the nocturnal cooling decreases as water depth increases.

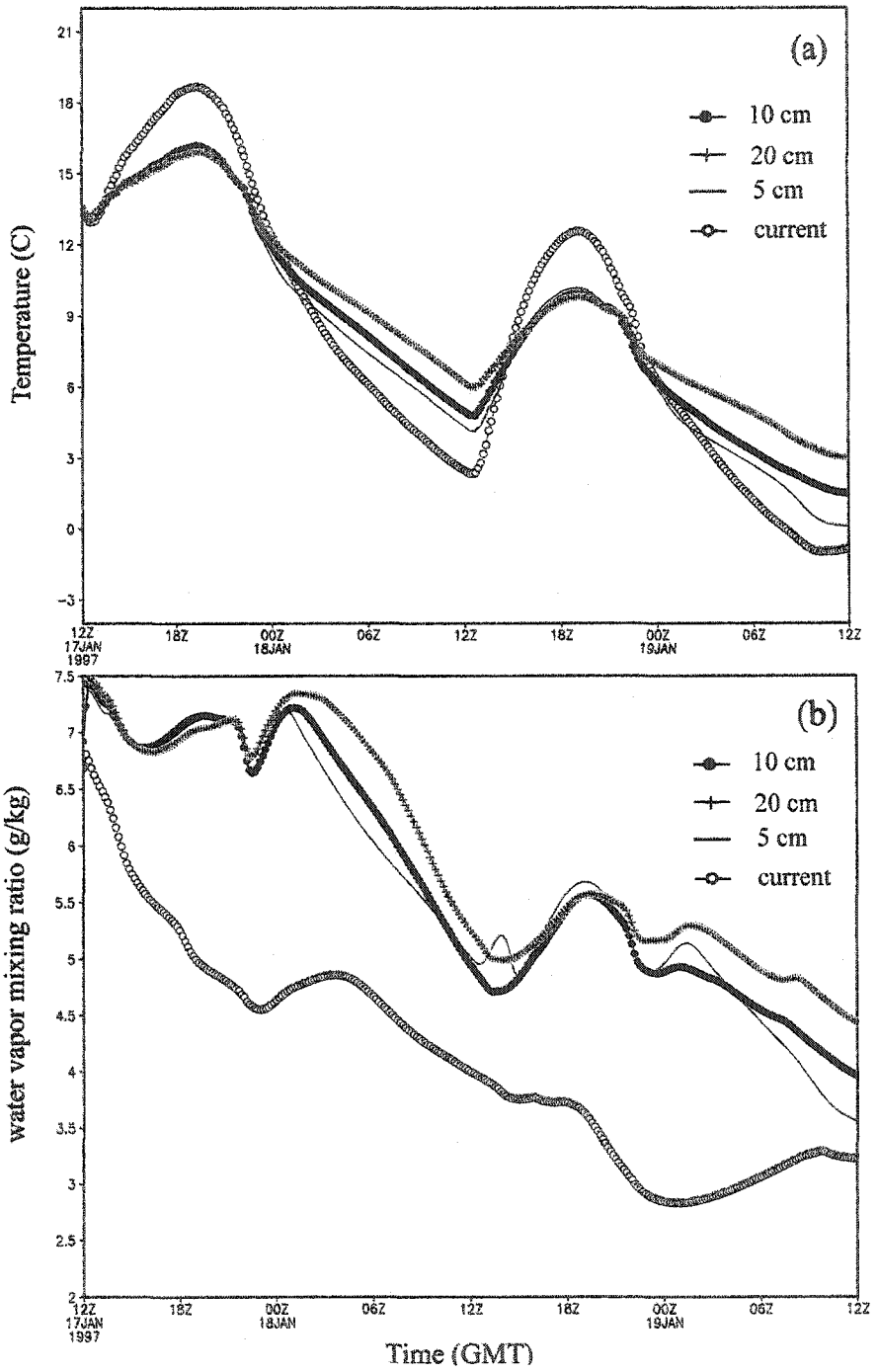

Figure 4.24. As in Figure 4.20, except with the addition of the time series corresponding to the 5 and 20 cm depths. Symbol convention same as in Figure 4.23.

The full diurnal cycles of the components of the surface energy budget for the alternative depths (not shown) exhibit similar behavior to the 2 m quantities and the skin temperature. For all energy budget components, the daytime values corresponding to the alternative depths are quite close to the daytime magnitudes illustrated in Figure 4.13 for the default 10 cm depth. At night, the values become spaced fairly evenly between the upper (20 cm depth) and lower (current land cover) bounds. Thus, during the daytime hours, when net radiation is high, the availability of any standing water on the surface, regardless of its depth, impacts the diurnal cycles more than the depth of the water itself.

Figure 4.25 provides a concise way to illustrate the nocturnal spread over the four cases, for each component of the surface energy budget, along with the available energy. In lieu of providing five figures, each with four overlapping time series, this figure can be used to illustrate the difference between the time series corresponding to standing water of 20 cm depth and the time series for the current land-cover case (former minus latter), for each of the five energy budget quantities. These difference time series can be compared with Figures 4.15 and 4.16 to deduce the impact of increased standing water on the surface energy budget. This comparison shows that, as water depth increases, the (absolute magnitude) of the ground heat flux remains greater for a longer period during the night, and the net radiation at the surface remains larger (in absolute magnitude) throughout the night. The net effect of this is to provide more available energy for much of the night when the depth is increased. For example, at 0300 UTC, the available energy with 20 cm of standing water is nearly 50 W m^{-2} greater than it is in the current land-cover case. As Figure 4.16 shows, the available energy is near 10 W m^{-2} with 10 cm of standing water, and near –20 W m^{-2} with the current land cover. Thus, the available

energy is increased by approximately 15 W m^{-2} when the water depth is doubled. In other words, the available energy itself is more than doubled by doubling the water depth.

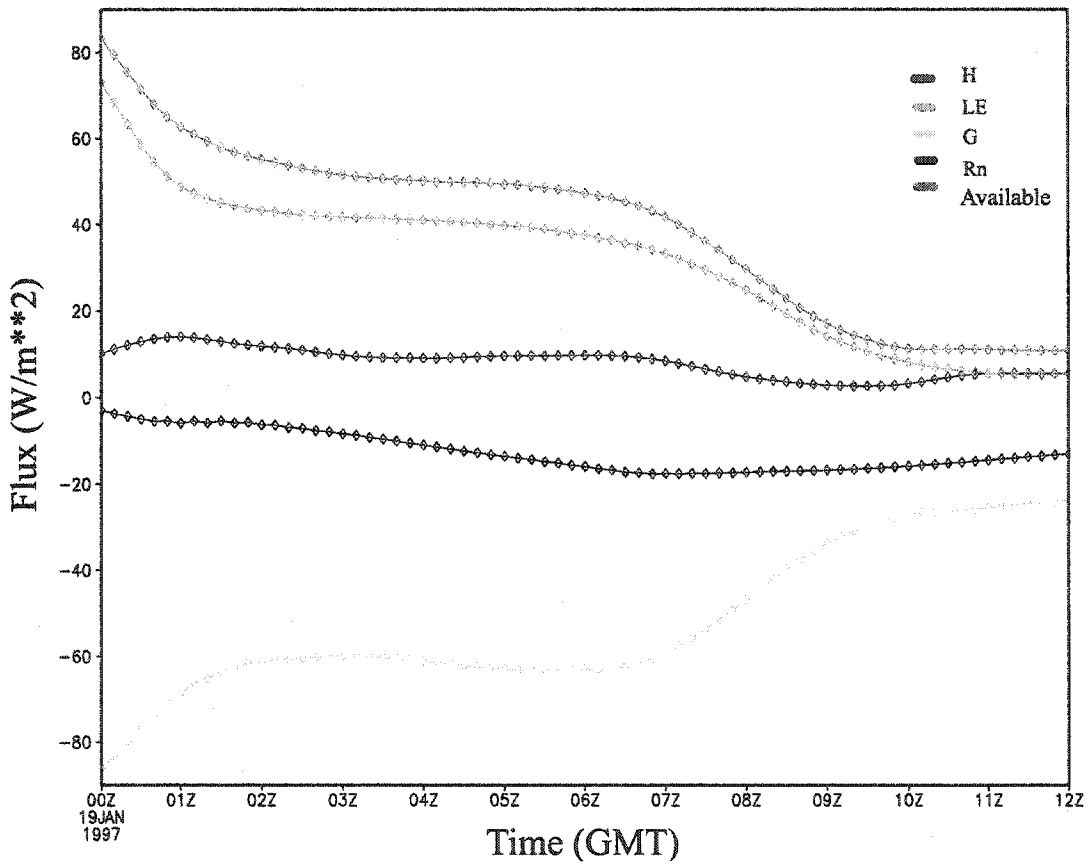

Figure 4.25. The difference of the time series corresponding to each of the components of the surface energy budget (all units in W m^{-2}) between the natural land-cover case with a specified water depth of 20 cm, and the current land-cover case. Difference defined as the former minus the latter.

As discussed above, the difference in the available energy between the default (10 cm depth) natural case and the current case was realized mostly as a sustained physical evaporation during the evening hours. Comparison of Figure 4.25 and 4.15 reveals that

the latent heat flux is nearly 10 W m^{-2} greater in the 20 cm case than it is the 10 cm case, whereas the (negative) sensible heat flux is 5 W m^{-2} greater. Thus, when the depth was doubled to 20 cm, the resulting 15 W m^{-2} of additional available energy was partitioned largely towards latent heat flux. Nevertheless, the difference in sensible heat flux is, relative to the current land-cover case, nearly doubled by doubling the water depth.

These results are indicative of the relationships among water depth, increase in available energy, the partitioning of that energy during the night, and the importance of radiative role of water vapor on the nocturnal cooling. In this context, some background information on the relationship of the land-surface energy fluxes to the tendencies of the water vapor and temperature in the atmospheric surface layer is useful. In particular, it is important to emphasize that while the magnitudes of the surface energy fluxes determine the evolution of the land surface state variables (i.e., temperature and moisture), that strictly speaking, the evolution of these variables in the air layer above the land-surface is related to the flux *divergence* in the air layer.

During the nocturnal cooling period, the negative net radiation at the land surface indicates loss of energy from the land-surface as the land-surface cools. As the land-surface cools, the air near ground level cools via sensible heat loss. The layer of air immediately above the surface cools from the "bottom up," and a surface-based thermal inversion forms. Consequently, the warmer air at the top of the inversion emits a larger flux of infrared radiation. This means that the layer experiences a net radiative flux *divergence*. Thus, the cooling of the air layer itself is related to upon the magnitude of this divergence, not just the magnitude of the surface flux itself. Similarly, the temperature of the layer is impacted by the sensible heat flux divergence in the layer. If

advection is neglected (a safe assumption in this case), the temperature tendency of the air near ground level (e.g., at 2 m) is a function of the sum of the two divergence quantities. If the layer of air contains gaseous or aerosol constituents that are radiatively active in the infrared spectrum (e.g., water vapor), the effect could be to dampen the net radiative flux divergence through the layer and thus reduce the contribution of the radiative flux divergence to the overall cooling rate of the layer. If the overall cooling is greater in magnitude than that indicated by the radiative flux divergence, then the sensible heat flux divergence must contribute to cooling of the layer.

Figure 4.26 provides time series of the radiative flux divergences and associated cooling rates in the first atmospheric layer above ground (which extends from the surface to near 20 m) for the current land-cover case and for each of the three natural case depths. The cooling of the layer indicates a net radiative flux divergence in the layer throughout the night. In the current case, the cumulative nocturnal cooling (defined here as the integral of the instantaneous cooling rate during the 0000-1200 UTC period) associated with the radiative flux divergence in the first model layer is near 7°C. For the natural case, with depths of 5 cm, 10 cm, and 20 cm, the cumulative radiative cooling is 5.3°C, 4.2°C, and 2.3°C, respectively. The corresponding actual magnitudes of the cooling of this layer during the same period, as indicated in the time series of the 2 m temperature (see Figure 4.24a), are 7.1°C, 5.5°C, 4.7°C, and 4.0°C. Thus, in the current land-cover case, the radiative cooling and the actual cooling are nearly equal. As the depth of water is increased in the natural case, the cooling associated solely with the radiative flux divergence decreases from about 96% to 58% of the total cooling.

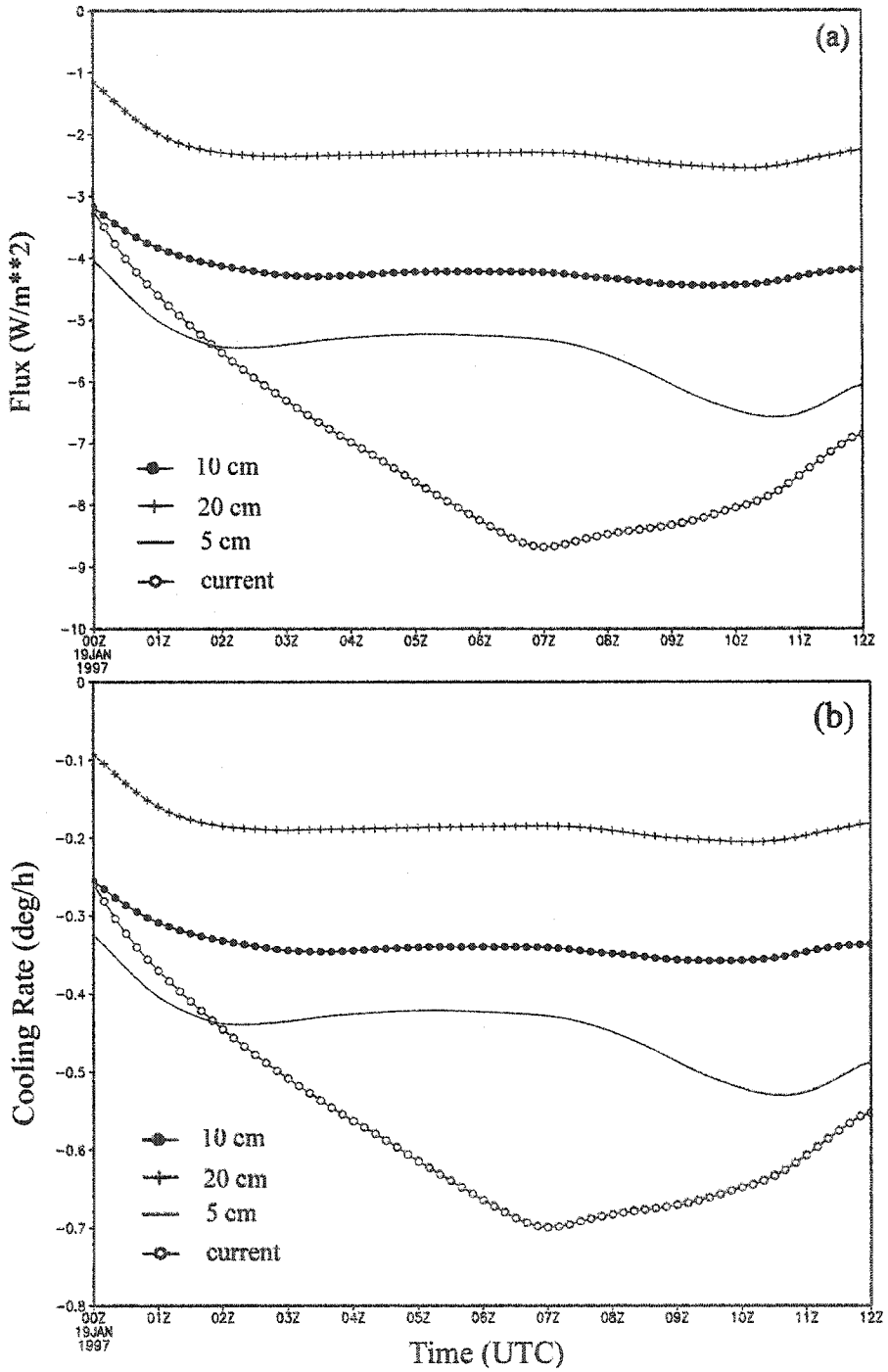

Figure 4.26. Time series of the (a) net radiative flux difference (W m^{-2}) in the first model layer (defined as Rn at the land surface minus Rn at model level 1, near 20 above ground level) and (b) the cooling rate (deg h^{-1}) due solely to the flux divergence in the same layer. Symbol convention same in Figure 4.23.

Figure 4.27 illustrates the time series of the sensible heat flux divergence and its associated cooling rate. The cumulative cooling magnitudes associated with the sensible heat flux divergence for the current land-cover case, and the natural cases with the three depths (from 5 cm to 20 cm) are near 0°C, 0.1°C, 0.5°C, and 1.6°C, respectively. Thus, the cooling due to sensible heat flux in each case virtually equals the difference between the total cooling of the layer and that due to radiative flux divergence.

Note that in all cases except the one corresponding to 20 cm depth, the sensible heat flux divergence actually changes sign at some point during the evening. These results are in agreement with recent observational findings by Sun et al. (2003). They showed that in strong nocturnal cooling situations during the earlier portion of the evening, as the land surface cools strongly and the atmosphere cools from the "bottom up," the sensible heat flux loss from a low level near ground to the ground itself often exceeds the sensible heat flux loss from some height above to the level in question. This indicates strong cooling due to sensible heat flux divergence at the lower levels. As the cooling progresses, the inversion deepens and stability increases over a greater depth, and the magnitude of the sensible heat flux divergence approaches zero. Various processes can act to modulate the stability of the profile both above and below a particular level as the night progresses (e.g., dew formation, time evolution of the vertical variation of water vapor absorption), and the sensible heat flux can actually become convergent at a particular level at some point during the night. The primary point here, however, is that, notwithstanding its nocturnal evolution, the effect of the *cumulative* nocturnal cooling from sensible heat flux divergence increases with increased water depth.

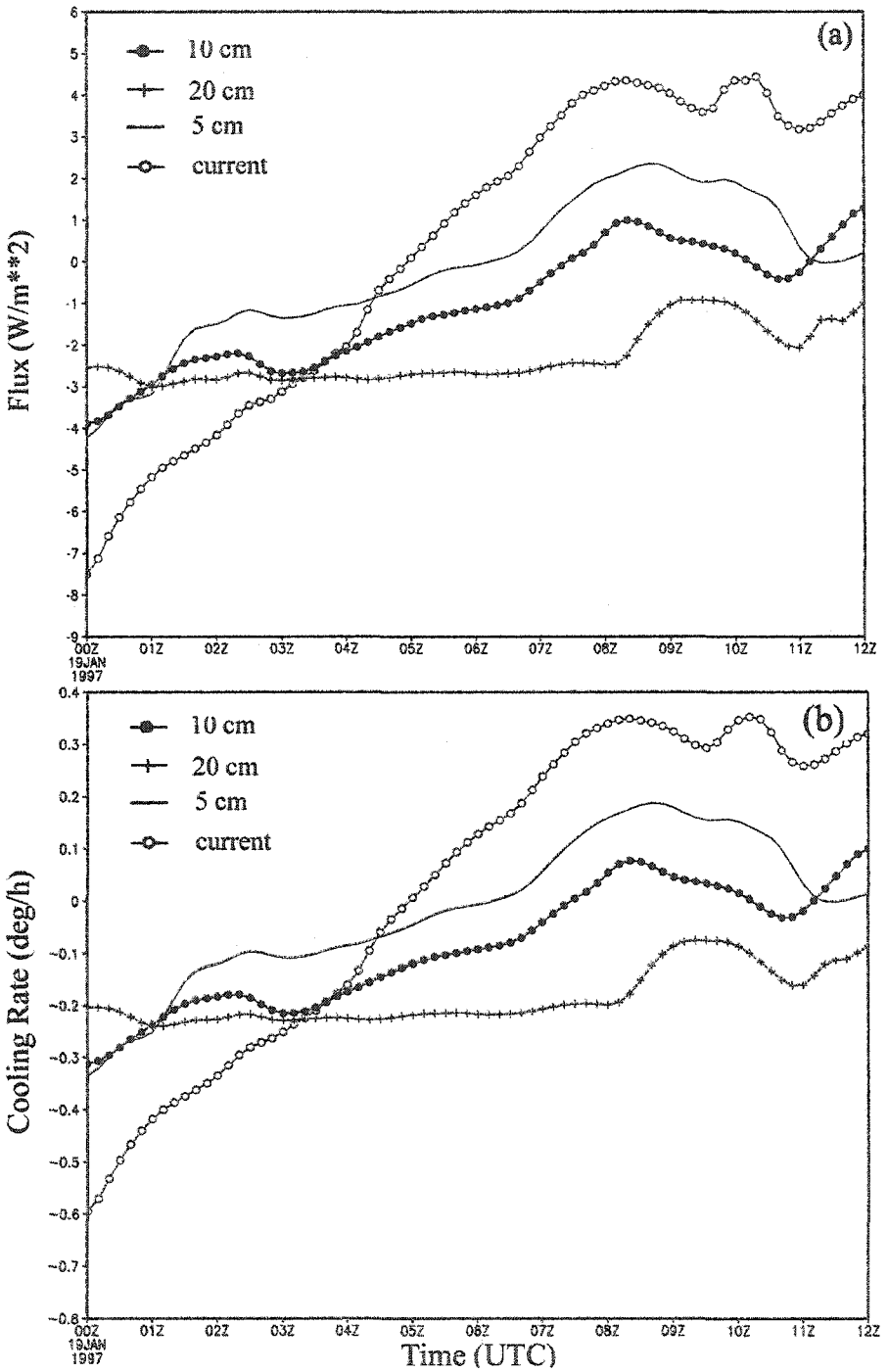

Figure 4.27. Same as in Figure 4.26, except the quantities pertain to sensible heat flux in the first model layer.

As discussed earlier, the spread of the atmospheric water vapor content in the three depth cases increased as the night progressed. As depth is increased, the surface water vapor flux during the night is increased, contributing to the differing tendencies of the atmospheric water vapor. Given that the contribution of the radiative flux divergence to the total cooling decreases as the depth of the standing water increases, these results suggest that the effect of absorption of outgoing longwave radiation by the atmospheric water vapor becomes increasingly important, meaning that the layer is absorbing more of the outgoing longwave radiation from the land surface as the water vapor increases. Of course, the overall magnitude of that outgoing radiation is controlled by the skin temperature, which is fundamentally related to the heat capacity of the surface and hence the depth of the water.

In this sense, it is re-emphasized that the effect of water depth on the heat capacity is the primary factor in determining the total cooling. As depth increases, both water vapor content of the air and the outgoing longwave radiation from underlying surface become larger, and the increased water vapor content acts to "trap" a greater proportion of the radiation. However, the cumulative cooling due to sensible heat flux divergence is increased in this situation. The fundamentally important point is that, at the end of the nocturnal cooling period, the presence of standing water has prevented the development of what was otherwise a devastating agricultural freeze.

Chapter 5

SUMMARY, CONCLUSIONS, AND SUGGESTIONS FOR FUTURE WORK

5.1 Summary and Conclusions

The land cover on the Florida peninsula was dramatically altered by human activities during the 20th Century. This work provides the results of a study that was designed to evaluate the impacts of these changes on the mesoscale climate of the region. Specifically, the Regional Atmospheric Modeling System was configured with datasets that represent pre-1900 (near natural) and 1993 (near-current) land cover. Pairs of simulations were produced for three separate July-August periods using the two configurations. The results within a given pair were compared to evaluate the impacts of land-cover change on warm season weather. The two configurations were also used to produce pairs of simulations for three recent freeze events, in order to assess impacts of land-cover change on an important aspect of the region's cool season weather.

The average shelter-level temperature in the July-August simulations was generally increased by implementing the current land-cover dataset. These results confirm the earlier conclusions of the brief study presented by Pielke et al. (1999). The results of the present study further demonstrate that at many locations, particularly interior areas of the peninsula where wetlands were drained and converted to agricultural land during the 20th Century, daytime maximum were increased locally by several

degrees, whereas the nighttime minimum at those locations actually *decreased*. This result is reflected in the grid average of the complete diurnal cycle, which was amplified by implementing the current land-cover dataset.

The results also agree with previous evidence and popular perceptions that convective rainfall across the peninsula decreased during the 20th Century. Moreover, this study has provided new evidence of a physical-dynamical mechanism that directly links the spatial patterns of land-cover change with changes in the sea-breeze circulations and the spatial distribution of sea-breeze generated convective rainfall. In particular, the spatial patterns of land-cover change directly affect the strength of the modeled sea-breeze circulations. In the natural land-cover simulations, a relative minimum in sensible heat flux along the water inundated floodplain of the Kissimmee River basin results in an outward-directed mesoscale flow that serves to reinforce the convergence and upward motion along the adjacent sea-breeze fronts. Implementing the current land cover in the simulations effectively removes the feature, resulting in general weakening of the sea breezes.

The weakening of the sea breezes results in decreased convective rainfall totals in areas of the model domain between the coasts and the Kissimmee River watershed. The outward directed mesoscale flow along the Kissimmee River valley in the natural land-cover case is accompanied by weak compensating subsidence. Thus, in the current land-cover case, the removal of the horizontal mesoscale flow results in weakening of this subsidence. The weakening of the subsidence is in turn associated with an axis of increased rainfall directly over the Kissimmee River valley, between the adjacent decreases along the sea-breezes fronts. When expressed as a spatial average over the

model domain, the precipitation in all three simulated periods with current land cover is decreased by 10% to 12% from the corresponding natural cover case. In hydrologic terms, this amounts to an average decrease of 2.6 M acre-ft of water during the July-August period. This result indicates that the mesoscale changes in the sea breezes and sea-breeze rainfall have a regional-scale effect, because the sea breezes provide the dominant mode of warm season rainfall in the region.

The overall magnitudes of convective rainfall differed when the simulations were repeated to test the sensitivity of the results to several factors, including grid spacing, convective parameterization, radiative transfer scheme, initial soil moisture, and regional SST. However, the difference in the simulated convective rainfall between the two land-cover cases *within a given sensitivity experiment* was consistent with the control case. Rainfall increased along an interior axis and decreased along the sea-breeze fronts, with grid average decreases generally in the range of 10-14% when current land cover was implemented. The consistency among the sensitivity experiments lends greater credence to the suggestion that these model results provide evidence that anthropogenic land-cover change could be responsible for hydrologically significant changes in the warm season precipitation climatology of the Florida peninsula.

Limited observational data were compiled to provide estimates of regional trends in July-August temperature and precipitation. The estimated trends indicate that daytime maximum temperature increased and rainfall decreased during much of the 20th Century. These trends are consistent with the model results. However, the observational trend of nighttime minimum indicates regional-scale warming, which is inconsistent with the model results. It is difficult to know whether this discrepancy results from model error

and uncertainty, observational error and uncertainty, a combination of these factors, or if the trend is real and associated with factors not addressed in this work.

The two model configurations were also used to determine the impact of land-cover change on the evolution of three recent freeze events that resulted in significant crop damage in south Florida. In all three pairs of freeze simulations, model minimum temperatures were generally colder and below 0°C for a longer duration at locations where wetlands were replaced by agricultural land. Further examination of the 19 January 1997 event reveals that when natural wetlands are specified at these locations, the impact of the standing water on the effective heat capacity of the land-surface dampens the nocturnal cooling. Furthermore, a persistent water vapor flux from the wetlands increased the water vapor content of the near-surface airmass relative to the content in the current land-cover case, despite large-scale advection of a drier low-level airmass into the region during the course of the simulation. The increased water vapor content acted to decrease the radiative cooling of the near-surface airmass during the night. The impact of the standing water on the heat capacity of the land-surface was found to be the primary factor in dampening the nocturnal cooling, but both of these factors served to limit the nocturnal cooling of the near-surface airmass in the natural land-cover case enough to altogether prevent the development of the freezing conditions that were simulated with current land cover.

A sensitivity analysis revealed that the overall magnitude of the nocturnal cooling decreased as the specified depth of water in the wetlands was increased. However, regardless of the specified depth, the presence of wetlands acted to prevent the development of freezing conditions. For the two other events, freezing temperatures

were simulated despite the specification of land cover. However, in both cases, minimum temperatures were colder and below 0°C for a longer duration at locations in the model domain where natural wetlands were replaced with agricultural land.

During the 20th Century, a series of devastating freeze events in northern and central Florida precipitated sharp southward migrations in the key production centers of the state's agricultural industries. These migrations, coupled with increasing winter vegetable and sugarcane cultivation, resulted in the draining of significant areas of natural wetlands in south Florida to provide new cropland. The results presented in this work suggest the ironic possibility that, in the attempt to avoid devastating freezes by relocating agricultural production centers to the wetlands of south Florida, draining the surface water may have resulted in an increase in the frequency and severity of freezes at those locations.

It is concluded that the results presented in this work are evidence that anthropogenic land-cover change has impacted several aspects of the mesoscale climate of the Florida peninsula, including warm season temperature, the strength of the sea breezes, convective rainfall, and the frequency and severity of damaging freeze events. This conclusion has important implications for land-use planning and water resources interests in Florida, including the ongoing efforts to restore the Everglades while providing the natural resources that are necessary to facilitate increasing agricultural production and rapid population growth. Given these implications, the results of this study also support previous studies in concluding that perturbations introduced to the climate system through anthropogenic land-cover change are physically and socioeconomically significant.

5.2 Suggestions for Future Work

The experimental design for this study is premised on the assumption that simulations of recently observed meteorology with two separate land-cover datasets designed to represent current and historical conditions can provide insight into the impact of land-cover change on weather over the historical period bracketed by those two datasets. In an ideal experimental design, historical land-cover datasets would be available for all individual periods within the long-term period of interest. For example, if land-cover datasets representing the conditions that existed on the peninsula during every July-August period were implemented to provide simulations for all of those periods, actual long-term trends could be derived from the model results for comparison with observational data. This experimental design could also be applied to simulate all cool season periods during the long-term period of record in order to evaluate the impacts of land-cover change on trends in the frequency and severity of freezes.

The construction of historical land-cover datasets that contain a degree of detail matching the datasets developed and implemented for this work presents a considerable challenge. Thus, the experimental design described above may not be feasible. However, the availability of increasingly sophisticated remote sensing techniques will provide a comprehensive record of future land-cover change. It is suggested that future land-cover datasets could be combined with observational and modeling tools to determine the impacts of anthropogenic land-cover change on future changes in the mesoscale climate of the Florida peninsula. Of course, future land-cover changes on the peninsula may not be as significant as 20th Century changes. However, this suggestion is not limited to the case of the Florida peninsula. Valuable knowledge could be gained by

using new and improved land-cover datasets to study the impacts of anthropogenic land-cover change on climate trends on scales ranging from the local to the global.

REFERENCES

Anthes, R. A., 1984: Enhancement of convective precipitation by mesoscale variations in vegetative covering in semiarid regions. *J. Climate Appl. Meteor.*, **23,** 541-554.

Atlas, R., N. Wolfson, and J. Terry, 1993: The effect of SST and soil moisture anomalies on GLA model simulations of the 1988 U.S. summer drought. *J. Climate*, **6,** 2034-2048.

Attaway, J. A., 1997: *A History of Florida Citrus Freezes.* Florida Science Source, Inc., Lake Alfred, FL, 368 pp.

Baker, R. D., B. H. Lynn, A. Boone, W.-K. Toa, and J. Simpson, 2001: The influence of soil moisture, coastline curvature, and land-breeze circulations on sea-breeze initiated precipitation, *J. Hydrometeorology,* **2,** 193-211.

Blanchard, D. O. and R. E. Lopez, 1985: Spatial patterns of convection in south Florida. *Mon. Wea. Rev.*, **113**, 1282-1299.

Boyle, R .H., and R. M. Mechem, 1982: Anatomy of a man-made drought. *Sports Illus.*, **56,** 46-54.

Byers, H. R., and H. R. Rodebush, 1948: Causes of thunderstorms in the Florida peninsula. *J. Meteor.*, **5**, 275-285.

Castro, C.L., W.Y.Y. Cheng, A.B. Beltrán, C.H. Marshall, Jr., R.A. Pielke, Sr., and W.R. Cotton, 2002: The Incorporation of the Kain-Fritsch Cumulus Parameterization Scheme in RAMS with a Terrain-Adjusted Trigger Function. *Fifth RAMS Users and Related Applications Workshop*. Santorini, Greece, 2002.

Chen, C. and W. R. Cotton, 1983: A one-dimensional simulation of the stratocumulus-capped mixed layer. *Bound.-Layer Meteor.*, **25**, 289-321.

Costanza, R., 1975: The spatial distribution of land use subsystems, incoming energy and energy use in south Florida from 1900 to 1973. M.S. thesis, Dept. of Architecture, University of Florida. [Available from Department of Architecture, University of Florida, P.O. Box 115702, Gainesville, FL 32611.]

_____, 1979: Embodied energy basis for economic-ecologic systems. Ph.D. dissertation, University of Florida, 253 pp. [Available from Department of Architecture, University of Florida, P.O. Box 115702, Gainesville, FL 32611.]

Cotton, W. R., R. A. Pielke Sr., R. L. Walko, G. E. Liston, C. Tremback, H. Jiang, R. L. McAnelly, J. Y. Harrington, M. E. Nicholls, G. G. Carrio, and J. P. McFadden, 2003: RAMS 2001: Current status and future directions. *Meteor. Atmos. Phys.*, **82**, 5-29.

Cressman, G., 1959: An operational analysis system. *Mon. Wea. Rev.*, **87**, 367-374.

Dalu, G. A., and R. A. Pielke, 1993: Vertical heat fluxes generated by mesoscale atmospheric flow induced by thermal inhomogeneities in the PBL. *J. Atmos. Sci.*, **50**, 919-926.

Davis, J. H., Jr. 1943: The Natural Features of Southern Florida. *Geological Bulletin No. 25.* Florida Dept. of Conservation, Tallahassee, FL, 130-215 pp.

Davies, H. C., 1976: A lateral boundary formulation for multi-level prediction models. *Quart. J. Roy. Meteor. Soc.*, **102**, 405-418.

Deardorff, J. W., 1974: Tree dimensional numerical study of turbulence in an entraining mixed layer. *Bound.-Layer Meteor.*, 7, 199-226.

Douglas, M. S. 1947. *Everglades: River of Grass*. Pineapple Press, 478 pp.

Downton, M. W., and K. A. Miller, 1993: The freeze risk to Florida citrus, part II: temperature variability and circulation patterns. *J. Climate,* **6,** 364-372.

ERS USDA, 1997: Florida freeze reducing supplies of fresh vegetables. *Agricultural Outlook,* Vol. 2, Economic Research Service, U.S. Department of Agriculture, No. 238, 9–11.

FAO, 1997: *Digital Soil Map of the World and Derived Soil Properties.* CD-ROM (Version 3.5).

FDACS, 2002: *Florida Agriculture Facts Directory 2002.* Florida Department of Agriculture and Consumer Services, 168 pp.

Fennessy, M. J., and J. Shukla, 1999: Impact of initial soil wetness of seasonal atmospheric prediction. *J. Climate,* **12,** 3167-3180.

Gannon, P. T., and T. E. Warner, 1990: Drought over south Florida: Mesoscale or synoptic scale? Preprints, *Eighth Conf. on Hydrometeorology,* Kananaskis Park, AB, Canada, Amer. Meteor. Soc., 3-6.

Hansen, J. W., J. W. Jones, C. K. Kiker, and A. W. Hodges, 1999: El Niño-Southern Oscillation impacts on winter vegetable production in Florida. *J. Climate,* **12,** 92-102.

Horel, J. D. and J. M. Wallace, 1981: Planetary-scale atmospheric phenomena associated with the Southern Oscillation. *Mon. Wea. Rev.*, **109**, 813-829.

Kain, J. S., and J. M. Fritsch, 1993: Convective parameterization for mesoscale models: The Kain-Fritsch Scheme. *The Representation of Cumulus Convection in Numerical Models,* Meteor. Monogr. K.A. Emmanuel and D.J. Raymond, Eds. No. 46, American Meteorological Society, Boston, 165-170.

Kalnay, E., and Coauthors, 1996: The NCEP/NCAR 40-Year Reanalysis Project. *Bull. Amer. Meteor. Soc.*, **77**, 437-471.

Küchler, A. W., 1964: Potential natural vegetation of the conterminous United States. Special Publ. No. 36. American Geophysical Society.

Kuo, H. L., 1974: Further studies of the parameterization of the influence of cumulus convection on large-scale flow. *J. Atmos. Sci.*, **31**, 1232-1240.

Kushlan, J. A., 1990: Freshwater marshes. *The Ecosystems of Florida,* R.L. Meyers and J. J. Ewel, Eds., University of Central Florida Press, Orlando, FL, 324-363.

Landers, J. L., and W. D. Boyle, 1999: An old-growth definition for upland longleaf and south Florida slash pine forests, woodlands, and savannas. General Technical Report SRS-29, Southern Research Station, Forest Service, United States Department of Agriculture, Asheville, NC, 15 pp.

Light, S. S., and J. W. Dineen, 1994: Water control in the Everglades: a historical perspective. *The Everglades: the ecosystem and its restoration,* S.M. Davis and J.C. Ogden, Eds., St. Lucie Press, Delray Beach, FL, 47-84.

Louis, J. F., 1979: Parametric model of vertical eddy fluxes in the atmosphere. *Bound.-Layer Meteor.,* **17,** 187-202.

Mahrer, Y. and R. A. Pielke, 1977: A numerical study of the airflow over irregular terrain. *Beitrage zur Physik der Atmosphere,* **50,** 98-113.

Maurer, E. P., A. W. Wood, J. C. Adam, D. P. Lettenmaier, and B. Nijssen, 2002: A long-term hydrologically-based data set of land surface fluxes and states for the conterminous United States. *J. Climate,* **15,** 3237-3251.

McVoy, C., 1996: Comparison of the South Florida Natural System Model with pre-canal Everglades hydrology estimated from historical sources. U.S. Geological Survey Fact Sheet FS-187-96, 2 pp. [Available online at http://sflwww.er.usgs.gov/publications/fs/187–96/.]

McVoy, C.W., Park, W.A., and Obeysekera, J., 2002: Landscapes and hydrology of the Everglades, circa 1850. U.S. Geological Survey, Open File Report.

Mellor, G. L., and T. Yamada, 1974: A hierarchy of turbulence closure models for planetary boundary layers. *J. Atmos. Sci.*, **31**, 1791-1806.

Michaels, P. J., R. A. Pielke, J. S. McQueen, and D.E. Sappington, 1987: Composite climatology of Florida summer thunderstorms. *Mon. Wea. Rev.*, **115**, 2781-2791.

Miller, K. A., 1991: Response of Florida citrus growers to the freezes of the 1980s. *Climate Res.*, **1**, 133-144.

Mintz, Y., 1984: The sensitivity of numerically simulated climates to land-surface conditions. *The Global Climate*, J. Houghton, Ed., Cambridge University Press, 79-105.

Monin, A. S., and A. M. Obukhov, 1954: Basic laws of turbulent mixing in the atmosphere near the ground. *Tr. Akad. Nauk SSSR Geoph. Inst.*, No. 24(151), 1963-1987.

Oke, T. R., 1987: *Boundary Layer Climates, 2nd Edition.* Halsted, 435 pp.

Paegle, J., K. C. Mo, and J. Nogués-Paegle, 1996: Dependence of simulated precipitation on surface evaporation during the 1993 United States summer floods. *Mon. Wea. Rev.*, **124,** 345-361.

Pearlstine, L.G., S.E. Smith, L. Brandt, C. Allen, W. Kitchens, and J. Stenberg, 2002: Assessing statewide biodiversity in the Florida GAP Analysis Project. *J. Environ. Manage.*, **66,** 127.144.

Pielke, R. A., 1974: A three-dimensional numerical model of the sea breezes over south Florida. *Mon. Wea. Rev.*, **102,** 115-139.

Pielke, R. A., 2001: Influence of the spatial distribution of vegetation and soils on the prediction of cumulus convective rainfall. *Rev. Geophys.*, **39,** 151-177.

Pielke, R. A., and W. R. Cotton, 1977: A mesoscale analysis over south Florida for a high rainfall event. *Mon. Wea. Rev.*, **105,** 343-362.

Pielke, R. A., W. R. Cotton, R. L. Walko, C. J. Tremback, W. A. Lyons, L. D. Grasso, M. E. Nicholls, M. D. Moran, D. A. Wesley, T. J. Lee, and J. H. Copeland, 1992: A comprehensive meteorological modeling system – RAMS. *Meteor. Atmos. Phys.*, **49,** 69-91.

Pielke, R. A., R. L. Walko, L. T. Steyaert, P. L. Vidale, G. E. Liston, W. A. Lyons, and T. N. Chase, 1999: The influence of anthropogenic landscape changes on weather in south Florida. *Mon. Wea. Rev.*, **127,** 1663- 1673.

Reynolds, R. W., and T. M. Smith, 1994: Improved global sea surface temperature analyses using optimum interpolation. *J. Climate,* **7,** 929-948.

Rogers, J. C., 1984: The association between the North Atlantic Oscillation and the Southern Oscillation in the Northern Hemisphere. *Mon. Wea. Rev.*, **112,** 1999-2015.

Rogers, J. C., and R. V. Rohli, 1991: Florida citrus freezes and polar anticyclones in the Great Plains. *J. Climate,* **4,** 1103-1113.

Ropelewski, C. F., and M. S. Halpert, 1986: North American precipitation and temperature patterns associated with the El Niño/Southern Oscillation (ENSO). *Mon. Wea. Rev.*, **114,** 2352-2362.

Schmidt, N., E. K. Lipp, J. B. Rose, and M. E. Luther, 2001: ENSO influences on seasonal rainfall and river discharge in Florida. *J. Climate,* **14,** 615-628.

Segal, M., and R. W. Arritt, 1992: Non-classical mesoscale circulations caused by surface sensible heat flux gradients. *Bull. Amer. Meteor. Soc.*, **73,** 1593-1604.

Simpson, J. E., 1994: *Sea Breeze and Local Winds.* Cambridge University Press, 234 pp.

Strack, J.E., G.E. Liston, and R.A. Pielke Sr., 2004: Modeling snow depth for improved simulation of snow-vegetation-atmosphere interactions. *J. Hydrometeor.,* **5**, 723-734.

Sun, J., S. P. Burns, A. C. Delany, S. P. Oncley, T. W. Horst, and D. H. Lenschow, 2003: Heat balance in the nocturnal boundary layer during CASES-99. *J. Appl. Meteor.*, **42**, 1649-1666.

Tremback. C. J., J. Powell, W. R. Cotton, and R. A. Pielke, 1987: The forward-in-time upstream advection scheme: extension to higher orders. *Mon. Wea. Rev.,* **115**, 540-555.

UCD, 1997: Florida freezes; west floods. *Rural Migration News,* Vol. 3, No. 2, Dept. of Agricultural Economics, University of California, Davis.

Vogelmann, J. E., T .L. Sohl, P. V. Campbell, and D .M. Shaw. 1998: Regional land cover characterization using Landsat Thematic Mapper data and ancillary data sources. *Environ. Monit. and Assess.,* **51**, 415-428.

Vogelmann, J.E., S. M. Howard, L. M. Yang, C. R. Larson, B. K. Wylie, and N. Van Driel, 2001: Completion of the 1990s National Land Cover Dataset for the conterminous United States from Landsat Thematic Mapper Data and ancillary data sources, *Photogrammetric Engineering and Remote Sensing,* **67,** No.6, 650-662.

Walker, J., and P. R. Rowntree. 1977: The effect of soil moisture on circulation and rainfall in a tropical model. *Quart. J. Roy. Meteor. Soc.,* **103,** 29-46.

Walko, R. L., L. E. Band, J. Baron, T. G. F. Kittel, R. Lammers, T. J. Lee, D. S. Ojima, R. A. Pielke Sr., C. Taylor, C. Tague, C. J. Tremback, and P. L. Vidale, 2000: Coupled atmosphere-biophysics-hydrology models for environmental modeling. *J. Appl. Meteor.,* **39,** 931-944.

Waylen, P. R., 1988: A statistical analysis of freezing temperatures in central and southern Florida. *J. Climatol.,* **8,** 607-628.

Waylen, P. R., and D. W. LeBoutillier, 1989: The statistical properties of freeze date variables and the length of the growing season. *J. Climate,* **2,** 1314-1328.

Weaver, C. P., and R. Avissar, 2001: Atmospheric disturbances caused by human modification of the landscape. *Bull. Amer. Meteor. Soc.,* **82,** 269-282.

_____, S. Baidya, and R. Avissar, 2002 Sensitivity of simulated mesoscale atmospheric circulations resulting from landscape heterogeneity to aspects of model configuration. *J. Geophys. Res.*, **107,** 1-21.

Weischet, W., and C. N. Caviedes, 1987: Citrus in Florida: ecological management and nature's latest intervention through freeze. *Erkunde,* **41,** 210-226.

Wetzel, P. I., 1990: A simple parcel method for prediction of cumulus onset and area-averaged cloud amount over heterogeneous land surfaces. *J. Appl. Meteor.,* **29,** 516-523.

Whittaker, H. M., 1985: Citrus tree losses from 1983 and 1985 freezes in fourteen northern counties. *Proc. FL State Hort. Soc.,* **98,** 46-48.

Willard, D. A., Weimer, L. M., and Riegel, W. L., 2001: Pollen assemblages as paleoenvironmental proxies in the Florida Everglades. *Rev. of Palaeobotany and Palynology,* **113,** 213-235.

Wolford, L. V., 1955: Citrus. *Weekly Wea. Crop Bull.*, **42,** 7-8.